GEMS & GEMOLOGY

WINTER 2017
VOLUME LIII

THE QUARTERLY JOURNAL OF THE GEMOLOGICAL INSTITUTE OF AMERICA

Large Cullinan-Like Diamonds with a Superdeep Origin

The Dreher Family of Gem Carvers

Akoya Cultured Pearls from Australia

A Chart of Ruby Inclusions

GEMS & GEMOLOGY
Winter 2017
VOLUME 53, No. 4


pg. 389


pg. 417


pg. 426


pg. 457

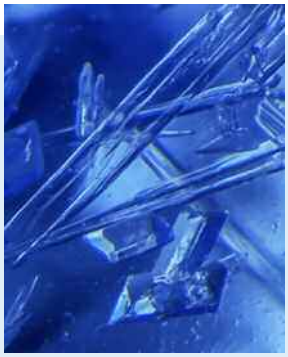
pg. 470

GEMS & GEMOLOGY

gia.edu/gems-gemology

Subscriptions
Copies of the current issue may be purchased for $29.95 plus shipping. Subscriptions are $79.99 for one year (4 issues) in the U.S. and $99.99 elsewhere. Canadian subscribers should add GST. Discounts are available for group subscriptions, GIA alumni, and current GIA students. To purchase print subscriptions, visit store.gia.edu or contact Customer Service. For institutional rates, contact Customer Service.

Database Coverage
G&G is abstracted in Thomson Reuters products (Current Contents: Physical, Chemical & Earth Sciences and Science Citation Index—Expanded, including the Web of Knowledge) and other databases. For a complete list of sources abstracting *G&G*, go to gia.edu/gems-gemology, and click on "Publication Information."

Manuscript Submissions
Gems & Gemology, a peer-reviewed journal, welcomes the submission of articles on all aspects of the field. Please see the Author Guidelines at gia.edu/gems-gemology or contact the Managing Editor. Letters on articles published in *G&G* are also welcome. Please note that Field Reports, Lab Notes, Gem News International, Micro-World, and Charts are not peer-reviewed sections but do undergo technical and editorial review.

Gems & Gemology is published quarterly by the Gemological Institute of America, a nonprofit educational organization for the gem and jewelry industry.

Postmaster: Return undeliverable copies of *Gems & Gemology* to GIA, The Robert Mouawad Campus, 5345 Armada Drive, Carlsbad, CA 92008.

Our Canadian goods and service registration number is 126142892RT.

About the Cover

The rough diamond shown on the cover, the 812 ct Constellation, was recovered from the Karowe mine in Botswana in November 2015. It is currently the sixth-largest gem-quality rough diamond ever recorded. It was sold in May 2016 for $63.1 million, the highest price paid for a rough diamond to date. The size, near absence of inclusions, low nitrogen content, shape, and surface texture place it in a special variety known as CLIPPIR diamonds, which are reviewed in the lead article in this issue. Diamonds such as the Constellation, which grow in a geologically distinct way, convey valuable information about the earth's deep mantle. Photo by Jian Xin (Jae) Liao.

Printing is by L+L Printers, Carlsbad, CA.
GIA World Headquarters The Robert Mouawad Campus 5345 Armada Drive Carlsbad, CA 92008 USA

ISSN 0016-626X

The World's Biggest Diamonds: Windows into the Earth's Deep Mantle

For geoscientists and gemologists alike, the origins of large, high-clarity, and relatively pure diamonds, like the Cullinan and the 812.77 ct Constellation on the cover of this issue, have long been an enigma. In a December 2016 *Science* article, a team of researchers led by GIA's Dr. Evan Smith provided important insights into how these rare and extraordinary gems form deep in the earth's mantle. That article presented evidence that such Cullinan-like, nitrogen-poor "CLIPPIR" diamonds contain high-pressure mineral inclusions that are only stable at depths of 360–750 km (approximately 225–465 miles). By contrast, the bulk of gem-quality diamonds form in the base of continental tectonic plates at depths of 150–200 km (95 to 125 miles). Inclusion-bearing CLIPPIR diamonds constitute only 1 in 10,000 of those submitted to GIA's laboratories. The inclusions these big diamonds carry—iron-nickel metal with minor sulfur and carbon—truly are a window into the earth's deeper mantle. In our lead paper, Evan Smith and Wuyi Wang partner with Steven B. Shirey of the Carnegie Institution for Science to build on the landmark *Science* article. They provide more detail on the key features of these remarkable diamonds as well as data on additional samples.

Natural diamonds are science's best tools for understanding the depths of the earth.

Our second paper, by Robert Weldon, Cathleen Jonathan, and Rose Tozer of GIA's Richard T. Liddicoat Library, explores the astonishing work of a multigenerational family of gem carvers: the Drehers of Idar-Oberstein, Germany. The authors focus on the contemporary craft of Gerd Dreher and his son, Patrick, artisans with an unerring ability to channel the spirit of the animals they model from high-quality rough gem minerals and richly patterned agates.

In our third paper, Laura Otter, Oluwatoosin Agbaje, Le Thi-Thu Huong, Tobias Häger, and Dorrit Jacob present the first gemological characterization of Australian akoya cultured pearls using Raman, photoluminescence, FTIR, and UV-Vis spectroscopy. Unlike many other akoyas, these Australian examples are marketed without any post-harvest treatments involving dyes or bleaches.

Next, Jennifer Stone-Sundberg, Timothy Thomas, Ziyin Sun, Yunbin Guan, Zachary Cole, Randy Equall, and John Emmett introduce a set of new reference standards designed to improve the quality of trace element analysis in ruby and sapphire. These standards use corundum substrates rather than the typical silicate glasses produced by the National Institutes of Standards and Technology (NIST). This important paper documents the development of corundum sets with precisely known levels of beryllium, magnesium, titanium, silicon, vanadium, chromium, iron, and gallium using secondary ion mass spectrometry (SIMS).

Stefanos Karampelas, Abeer Tawfeeq Al-Alawi, and Ali Al-Attawi provide a comparison of real-time X-ray micro-radiography (RTX) units fitted with different detectors. Their analysis demonstrates the superior resolving power of a flat panel detector (FPD) over an image intensifier (II) for interpreting fine detail in a pearl's internal growth structure.

And to complement our emerald and sapphire charts from Winter 2016 and Summer 2017, we present a new one featuring some characteristic internal features of natural, treated, and synthetic ruby. This chart is from GIA's team of inclusion specialists, led by Nathan Renfro and John Koivula.

As always, there's something for every gemological taste in our Lab Notes, Gem News International, and Micro-World sections.

Finally, I encourage you to join us for the 2018 GIA Symposium, October 7–9 in Carlsbad, California. This promises to be an unforgettable learning and networking event. You can register to attend or submit an abstract for an oral or poster presentation at symposium.gia.edu.

The Constellation diamond, with a maximum width of 64 mm, is shown beside a 1 ct round brilliant. Photo by Jian Xin (Jae) Liao.

Duncan Pay | Editor-in-Chief | dpay@gia.edu

The Very Deep Origin of the World's Biggest Diamonds

Evan M. Smith, Steven B. Shirey, and Wuyi Wang

Large and relatively pure diamonds like the historic 3,106 ct Cullinan, found in South Africa in 1905, have long been regarded as unusual based on their physical characteristics. For example, they often exhibit exceptional color and clarity, while routinely qualifying as type IIa, a rare designation of chemical purity. A new research discovery about these Cullinan-like diamonds is that they contain heretofore unknown, deeply derived inclusions that originate below the continental mantle keel and are thus known as "superdeep" diamonds (Smith et al., 2016). Originating from a depth between 360 and 750 km, they reveal information about the conditions within the convecting mantle, beneath the earth's rigid tectonic plates. Here we review the previously published findings, compare the Cullinan-like diamonds to the more abundant lithospheric diamond population, and offer evidence from some additional diamond samples that further verifies their superdeep origin. Cullinan-like diamonds contain minute and rare silicate and iron-rich metallic inclusions surrounded by a fluid jacket composed of methane and hydrogen. The inclusion compositions suggest that this deep mantle environment contains small pockets of oxygen-deficient metallic liquid out of which the diamonds crystallized. This new and unexpected observation made on the world's most expensive diamonds is important for understanding the chemical reactions between mineral assemblages in the deep earth. It shows that deep regions of the mantle contain metallic iron, as opposed to the shallower, more oxidized mantle rocks actively participating in plate tectonics and its associated volcanism.

Diamonds, besides being the most valuable gemstones for jewelry, are some of the most scientifically valuable samples of the deep earth. Interpretation of their included minerals and crystallization history provides a snapshot of otherwise inaccessible geological processes from more than 100 kilometers underground and often from billions of years in the past (e.g., Shirey and Shigley, 2013). No other mineral sample can provide information for research from such depths and from so long ago. Until recently, exceptional gem diamonds such as the famous Cullinan or Lesotho Promise, with a set of physical characteristics that distinguish them from other kinds of diamonds, were enigmatic and had an unknown origin (Bowen et al., 2009; Gurney and Helmstaedt, 2012; Moore, 2014). How did they form? Certainly not like 99% of other gem diamonds. New research carried out in the last two years at GIA, the Carnegie Institution for Science, and the University of Padua reveals that these Cullinan-like diamonds form in a geologically special way, involving metallic liquid and originating from extreme depths in Earth's mantle well below that of other gem diamonds (Smith et al., 2016).

RECOGNITION OF A NEW DIAMOND VARIETY

As a family, these diamonds tend to be large, inclusion-poor, and relatively pure (usually type IIa), and in their rough state they are irregularly shaped and significantly resorbed (figure 1) (Bowen et al., 2009; Gurney and Helmstaedt, 2012; Moore, 2014; Smith et al., 2016). These characteristics are combined in the acronym "CLIPPIR" (Cullinan-like, Large, Inclusion-Poor, Pure, Irregular, and Resorbed). Figure 2 shows a broad dataset of assorted diamonds, where the CLIPPIR population displays these characteristics. Among larger diamonds, there is a striking increase in the prevalence of D color grades and the proportion of type IIa diamonds, chiefly due to their

See end of article for About the Authors and Acknowledgments.
Gems & Gemology, Vol. 53, No. 4, pp. 388–403,
http://dx.doi.org/10.5741/GEMS.53.4.388

Figure 1. Rough CLIPPIR diamonds have physical features akin to the historic Cullinan diamond, which forms the "C" of the CLIPPIR acronym. The size distribution for this variety of diamond is skewed toward large sizes, with the examples shown here ranging from 14 to 91 carats. In rough form, CLIPPIR diamonds are irregularly shaped rather than well-formed crystals and sometimes appear to be broken fragments of once larger diamonds. Photo by Robert Weldon/GIA; courtesy of Gem Diamonds Ltd.

lack of nitrogen. As expected, these larger type IIa diamonds have very few inclusions and consequently high clarity grades.

Historically, it has been difficult to study these diamonds because of their rarity and high value as gemstones; they simply cannot be purchased for in-depth analysis on a research budget. It is only through the research program of GIA, where thousands of high-quality gem diamonds were available to be examined by non-destructive methods such as Raman spectroscopy and X-ray diffraction, that their common inclusion paragenesis and hence their origin was revealed. Here we review in more detail the key features of diamonds reported by Smith et al. (2016) as well as some additional CLIPPIR samples examined since.

An important key to the origin of these diamonds lies in the special inclusions they contain, composed of iron-nickel metal with minor sulfur and carbon. At the ambient pressure and temperature under which the CLIPPIR diamonds formed, these inclusions were metallic liquids. But now, under surface conditions, they have cooled and crystallized to a distinctive, rarely seen mineral assemblage. This assemblage includes the rare mineral cohenite, an iron-rich carbide with the formula $(Fe,Ni)_3C$, and the relatively common iron sulfide mineral pyrrhotite.

Metallic iron-nickel alloy is thought to be created and stabilized in parts of the deep mantle (Frost et al., 2004; Rohrbach et al., 2007). Although the normal amount of metal in these regions of the mantle is likely about 1% or less, it is expected to regulate and limit the local activity of oxygen (Frost et al., 2004). Oxygen availability is a key planetary parameter resulting from the earth's large-scale geologic evolution (Rohrbach and Schmidt, 2011). It controls, along with temperature and pressure, the basic mineral composition of the planet's interior, how this varies with depth, and the composition of melts generated. At the pressure and temperature conditions near and at Earth's surface, rocks almost never contain metallic iron. Also, these shallower rocks are affected by magmatism associated with plate tectonics and by interaction with Earth's atmosphere and hydrosphere,

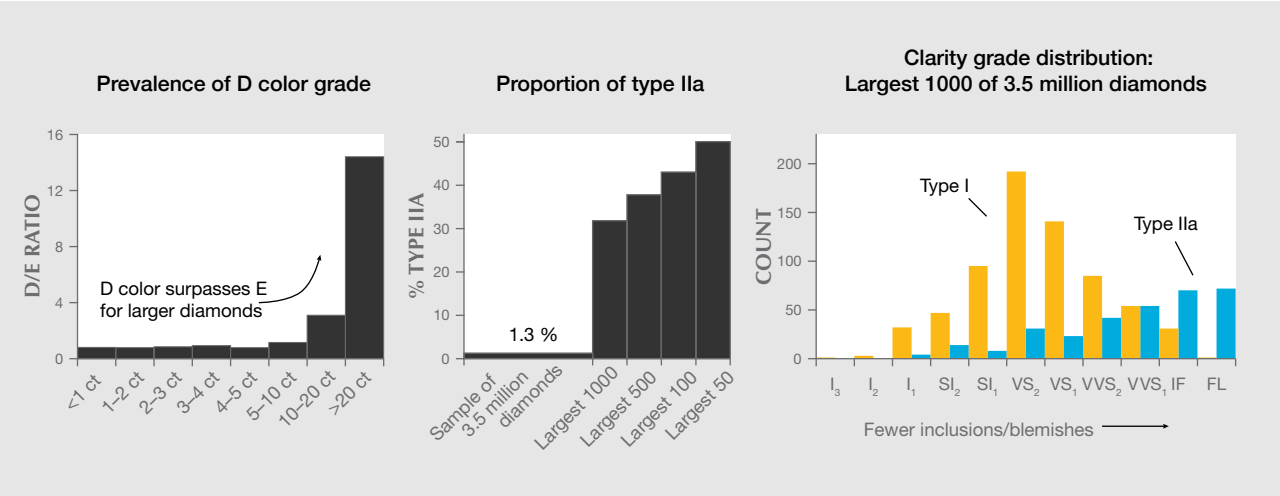

Figure 2. Systematic deviations of properties suggest that CLIPPIR diamonds become more prevalent among larger-sized diamonds. Left: Diamonds over 5 carats show an increasing incidence of D color grades in a random sample of 4.2 million diamonds graded by GIA; shown is the ratio of D color (colorless) to E color (not quite perfectly colorless) grades awarded. Center: In a similar dataset of 3.5 million samples, the proportion of type IIa diamonds (nitrogen-deficient, high-purity) also increases dramatically when considering only the larger diamonds. Right: Among a set of large diamonds, all over 15 carats, those qualifying as type IIa have markedly higher clarity and dominate the flawless grade category. (GIA clarity abbreviations: FL = flawless, IF = internally flawless, $VVS_{1/2}$ = very very slightly included 1/2, $VS_{1/2}$ = very slightly included 1/2, $SI_{1/2}$ = slightly included 1/2, and $I_{1/2/3}$ = included 1/2/3)

which occur at relatively oxidizing conditions. These conditions completely mask the ambient conditions in the earth's deep interior, which can be revealed in the mineralogy of CLIPPIR inclusions. It is coincidental but agreeably fitting that the world's most valuable diamonds as gemstones have now taken on exceptional scientific value.

NITROGEN AND THE DISTINCTION BETWEEN TYPE IIA AND CLIPPIR DIAMONDS

Nitrogen is all around us every day, making up 78% of the air we breathe and forming an essential element for life on Earth. Nitrogen behavior inside the earth, especially in minerals and fluids deep in the mantle, is less understood, but nitrogen is thought to be recycled into the mantle by plate tectonic activity. In the mantle, it is an ingredient in the diamond-forming fluids for the most common diamonds, known as type I. As such it is the most abundant trace element in diamond, where it substitutes for carbon atoms in the crystal structure. Since the advent of studies to understand the geological conditions for diamond growth and formation, diamonds have become one of the important tools that can help geologists trace the deep cycling and behavior of nitrogen.

The nitrogen content of diamond can vary greatly for several reasons, including variable supply of nitrogen in diamond-forming fluids, variable partitioning into the diamond, and variable partitioning into a competing nitrogen-bearing phase. Diamonds with no appreciable nitrogen-related absorption in the 800–1400 cm^{-1} range in infrared spectroscopy are classically defined as type IIa (Wilks and Wilks, 1994). Note that the abundance of nitrogen in diamond is a continuous range without a sharp division. The continuous range means that the 5–20 ppm nitrogen concentration threshold that marks the boundary in classification between type IIa (nitrogen-deficient) and type I (nitrogen-bearing) has no basis in mineralogy but rather is based on analytical sensitivity. Analytical sensitivity has shifted to lower thresholds over time, as instrumentation has improved.

The type IIa designation of chemical purity is usually regarded as a desirable gemological trait that is associated with high clarity and color, and it has proven convenient for scientific classification of diamond (see review by Breeding and Shigley, 2009). With one exception, the CLIPPIR diamonds of this study are type IIa. The relationship between CLIPPIR and type IIa diamonds likely applies to larger unstudied populations, as shown by the disproportionate

number of large, high-quality diamonds that are type IIa (figure 2). It is important to bear in mind, however, that not all type IIa diamonds are classified as CLIPPIR, and vice versa. Some lithospheric diamonds from peridotitic and eclogitic host rocks, for example, can also have very low nitrogen concentrations and be considered type IIa (e.g., Stachel and Harris, 2009; Gurney et al., 2010; Moore, 2014).

SOLIDIFIED IRON-NICKEL METAL: A NEWLY RECOGNIZED INCLUSION TYPE

Although inclusions are scarce in CLIPPIR diamonds, with the right approach they can be sought and studied. By leveraging a high-volume diamond grading service like that of GIA to find prospective samples for examination, it was possible to cull out enough of the rare inclusion-bearing CLIPPIR diamonds to look at their features as a group. In the past, the only reported inclusions in CLIPPIR diamonds were flat black inclusions with round boundaries, previously assumed to be flecks of graphite (Bowen et al., 2009; Moore, 2014). Rarely, some inclusions have been suspected to be sulfides, as they can resemble common pyrrhotite and pentlandite inclusions in lithospheric diamonds (Bowen, pers. comm., 2013, in Moore, 2014). However, a search of the literature reveals that the only consistently reported inclusion is visually identified graphite. In fact, the Cullinan diamond itself was described as having a small round, black inclusion in the center, which was intentionally bisected with the first cleave of the rough diamond by Joseph Asscher in 1908 (Crookes, 1909). Of course, the finished Cullinan gemstones are essentially flawless and free of inclusions (Scarratt and Shor, 2006). What few inclusions are to be found in rough CLIPPIR diamonds are usually eliminated during cutting and polishing, making the search for inclusions all the more difficult among polished goods.

In Brief

- Unusually large and pure diamonds like the 3,106 ct Cullinan have a special geological origin, much deeper in the earth's mantle than most other gem diamonds.
- Many of the world's biggest high-clarity, D-color diamonds belong to this special variety known as CLIPPIR diamonds.
- Newly recognized iron-rich metallic inclusions in these diamonds provide insight into the makeup of the deep earth.
- There is still much to be learned from the study of diamonds, which are an invaluable "window" into the unseen world deep beneath our feet.

Our recent study (Smith et al., 2016), comprising a targeted subset from hundreds of thousands of faceted diamonds as well as a small number of offcuts trimmed from rough diamonds during cutting and faceting, documented 53 inclusion-bearing CLIPPIR diamonds that establish a specific inclusion assemblage that deviates from known lithospheric or sublithospheric suites. Thirty additional faceted stones have since been studied and now yield observations on a total of 83 diamonds, summarized in table 1 (see also data supplement at www.gia.edu/gems-gemology/winter-2017-worlds-biggest-diamonds; for methods, see Smith et al., 2016). Past visual descriptions of inclusions in these types of diamonds mention flat, black features, interpreted as graphite. Our work has shown that these are graphitic rosette fractures that surround and sometimes conceal a much smaller non-graphitic inclusion (figure 3) somewhat reminiscent of sulfide inclusions.

In the center of the black fractures, the inclusion nucleus itself is different from that of a typical sulfide inclusion. In contrast to lithospheric diamonds, where black fracture rosettes are typically associated with sulfide inclusions, CLIPPIR diamonds have black fractures surrounding many inclusions, such that even silicates can have a superficial resemblance to "common" sulfide inclusions (figure 4A; see also figures S2 and S3 in Smith et al., 2016). The fractures are likely due to the higher stresses that build up around most superdeep inclusions when they are exhumed from the mantle.

The most common inclusion identified in CLIPPIR diamonds is a metallic iron-nickel-carbon-sulfur mixture. While most of these inclusions can only be studied remotely through the diamond by Raman spectroscopy, all inclusions that can be examined directly by other microanalytical techniques such as scanning electron microscopy (SEM), electron microprobe analysis, and/or X-ray diffraction (XRD) are similar metallic Fe-Ni-C-S mixtures. In our experience, these metallic inclusions differ from sulfide inclusions, which also have metallic luster but are smoother, more equant cuboctahedral shapes, isolated rather than grouped, and far less magnetic. The sulfide inclusions sometimes have brassy colors and identifiable sulfide mineral Raman features, and they have not yet been found to have coexisting fluid. In contrast, the Fe-Ni-

C-S metallic inclusions often have step-faced surfaces, strong magnetism, and elongate and irregular shapes, grouping into chains, and routinely possess a coexisting fluid phase (again, see figure 3).

Specifically, these inclusions are accompanied by a thin, invisible fluid layer of methane (CH_4) and lesser hydrogen (H_2) trapped at the interface between the solid inclusion and surrounding diamond (figure 5). Detailed analysis of the inclusions reveals that they are made up of cohenite ($(Fe, Ni)_3C$), interstitial Fe-Ni alloy, segregations of Fe-sulfide, and minor occasional Fe-Cr oxide, Fe-oxide (likely wüstite), and Fe-phosphate (Smith et al., 2016). We interpret the minor oxides as evidence of small amounts of oxygen even in these relatively oxygen-poor conditions, because all the inclusions examined were carefully selected from unaltered diamonds that had no surface-reaching fractures. This assemblage of minerals is interpreted to have crystallized during transport to the surface from the molten metallic liquid that was trapped during diamond growth at depth. The metal contains very limited amounts of oxygen, which indicates that CLIPPIR diamonds form under reducing conditions in the mantle. Metallic Fe-Ni-C-S melt inclusions such as these have not been described previously, although rare, isolated occurrences of native iron, iron-nickel alloy, and iron carbide inclusions have been found in other diamonds (Sharp, 1966; Jacob et al., 2004; Kaminsky and Wirth, 2011; Mikhail et al., 2014). Coincidentally, the German mineralogist Emil Cohen, for whom cohenite is named, might have encountered one of these Fe-Ni-C-S melt inclusions in an 80 ct rough diamond in South Africa 140 years ago, though he described the inclusion as "specular iron" or hematite based on color, luster, and form ("Iron in diamonds," 1877).

Figure 3. Examples of the typical appearance of metallic Fe-Ni-C-S inclusions in CLIPPIR diamonds. A: Two parallel <111> oriented chains (field of view 2.34 mm). B: Backlit inclusion chain (field of view 1.42 mm). C: Elongate metallic inclusion with a round black fracture of {111} orientation that obliquely cuts the <111> elongation direction of the inclusion (field of view 1.42 mm). D: A less elongate metallic inclusion with a small irregular tail on the lower left (field of view 1.42 mm). Photos by Evan M. Smith.

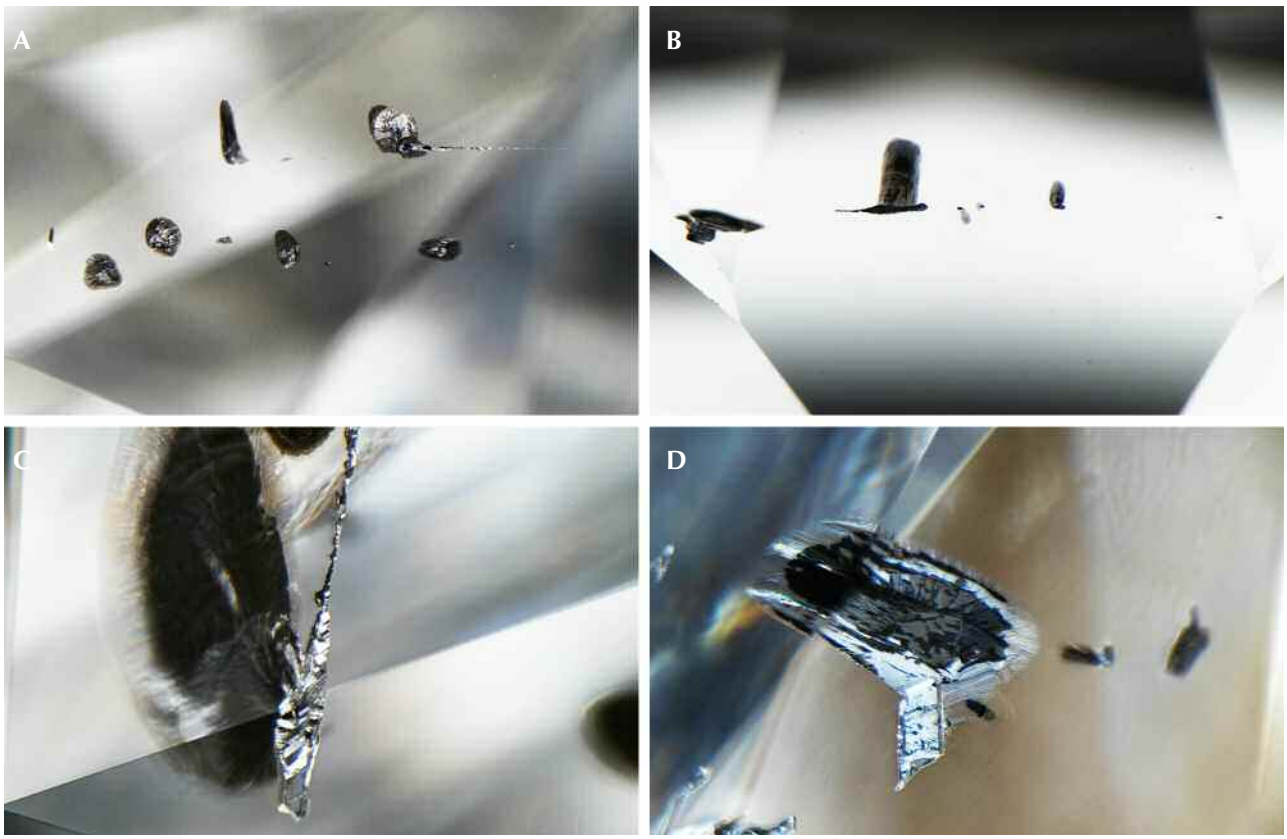

TABLE 1. Summary of inclusions observed in 83 CLIPPIR diamonds.

No. of diamonds	Largest in group	Inclusion assemblage	Inclusion properties	Mineralogy
60	30.13 ct	Metallic Fe-Ni-C-S (inferred to be primary melt inclusions)	Magnetic, silver/black color, opaque, grouped in <111> chains, CH_4 fluid jacket (22 also had detectable H_2 in Raman); associated with healed cracks; alters to red-brown (hematite).	Cohenite $(Fe,Ni)_3C$ + Fe-Ni alloy + pyrrhotite + minor phases
15	32.88 ct	Calcium silicate phases with original perovskite structure inferred (CaPv)	Colorless, transparent, often with droplet-like satellite inclusions defining lobes of localized healed cracks; one diamond had inclusions with CH_4 + H_2 fluid jackets but no indication of metal.	$CaSiO_3$-walstromite ± larnite (β-Ca_2SiO_4) ± $CaSi_2O_5$-titanite ± wollastonite ± perovskite ($CaTiO_3$)
4	10.21 ct	CaPv + metal	Colorless, transparent, with opaque, magnetic, metallic-luster droplet-like satellite inclusions with detectable CH_4; note that the silicate and metal co-occur rather than appearing as discrete separate inclusions.	$CaSiO_3$-walstromite ± larnite (β-Ca_2SiO_4) ± $CaSi_2O_5$-titanite + Fe-Ni-C-S phases
2	10.21 ct	Majoritic garnet + metal	Pale orange, transparent, with opaque, magnetic metallic phase partly occupying inclusion space, with detectable CH_4; note that the garnet and metal co-occur rather than appearing as discrete separate inclusions.	Low-Cr majoritic garnet ± Fe-Ni-C-S phases ± retrograde clinopyroxene, plagioclase, olivine
1	4.41 ct	CaPv + majoritic garnet + metal	Pale orange, transparent garnet inclusions with distinct metallic opaque regions exhibiting strong magnetism, with detectable CH_4; one colorless, transparent calcium silicate.	Majoritic garnet with metallic component + $CaSiO_3$-walstromite
1	10.17 ct	CaPv + majoritic garnet	Two colorless transparent calcium silicate inclusions; one pale orange, transparent garnet inclusion.	$CaSiO_3$-walstromite + majoritic garnet

Combines results from 53 diamonds in Smith et al. (2016) and 30 additional diamonds (see supplement at www.gia.edu/gems-gemology/winter-2017-worlds-biggest-diamonds). Average diamond mass is 6.1 ct, with 13 of them >10 ct. Note that most recorded masses are for the cut diamond and original mass of rough is unknown (also see data S1 in Smith et al., 2016).

The metallic inclusions (figures 3 and 5) have a silvery metallic luster with variable coating of patchy black graphite (as identified with Raman spectroscopy—a technique that can help identify minerals using a focused laser). They are bound by sharp-edged, flat cuboctahedral faces as well as complex stepped faces, and are often elongate in one dimension corresponding to a <111> vector with respect to the host diamond crystal. Inclusions near the surface of the diamond are noticeably magnetic when brought near a small rare-earth magnet suspended from a thread. Magnetism can be helpful for recognizing these inclusions but is not definitive since some other kinds of inclusions can be magnetic, such as sulfides or the metallic flux trapped in HPHT (high-pressure, high-temperature) synthetic diamonds. Raman spectroscopy, while of limited usefulness in identifying these inclusions since they are dominated by metals and carbides (both of which are inactive or weakly active in Raman), is good at revealing sulfides, which yield distinctive Raman peaks. We therefore take the general lack of Raman response from the inclusions with metallic luster as additional evidence that they are multi-phase metallic assemblages in which iron sulfide is a partial component rather than wholly sulfide mineral inclusions, which would have a distinctive Raman response.

Taken together, the metallic inclusions' consistent shape, texture, grouping, magnetism, lack of clear Raman response, and other features justify extending the microprobe and XRD results (Smith et al., 2016) to the majority of inclusions in the faceted samples that have been studied. It is unlikely that some of the metallic inclusions were misidentified sulfide inclusions. Furthermore, it is important to

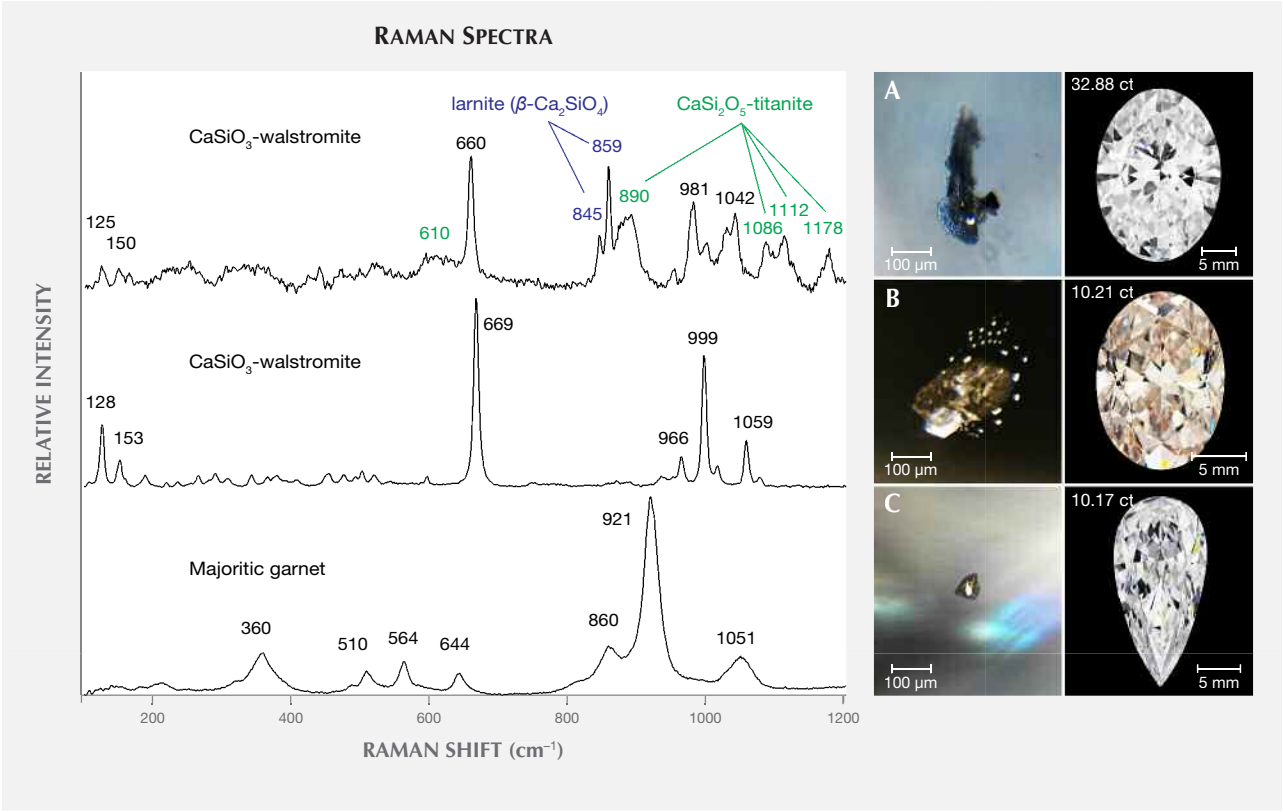

Figure 4. Raman spectra representative of the silicates in CLIPPIR diamonds. Spectra are offset vertically to avoid overlap. A: The principal silicate phase $CaSiO_3$-walstromite is accompanied by Ca_2SiO_4 and $CaSi_2O_5$ in a small colorless inclusion with a large graphitic fracture in a 32.88 ct D-color type IIa diamond. The middle spectrum shows $CaSiO_3$-walstromite alone, with peak positions noticeably shifted due to high remnant pressure inside the inclusion, on the order of several gigapascals (Anzolini et al., 2017). B: This $CaSiO_3$-walstromite inclusion in a 10.21 ct light pinkish brown type IIa diamond is a good example of the main part of the inclusion being accompanied by many smaller satellite inclusions, presumably from inclusion rupture/expansion during inversion from CaPv. C: Majoritic garnet in the bottom spectrum was observed in a 10.17 ct D-color type IIa diamond. Note this 10.17 ct sample contained both majorite and $CaSiO_3$-walstromite, and the bottom two spectra were actually both collected from this diamond. Photomicrographs by Evan M. Smith, face-up diamond photos by Jian Xin (Jae) Liao.

note that sulfide (pyrrhotite) appears to have been exsolved from the Fe-Ni-C-S mixture, suggesting that the original metallic liquid would have dissolved any sulfide minerals in this geologic environment, making it unlikely that discrete sulfide mineral grains would be available to be trapped as inclusions.

The fluid jacket with hydrogen and methane surrounding these inclusions is detectable with Raman spectroscopy, although the fluid is not uniformly distributed over the inclusion interface (figure 5). Methane (CH_4) is most easily detected and has a peak at 2918 cm^{-1}, while hydrogen (H_2) is generally less abundant but has its main peak at 4156 cm^{-1} (Smith et al., 2016). Peaks may be shifted by a few wavenumbers due to residual pressure inside the inclusions (Frezzotti et al., 2012). Methane is present at the inclusion-diamond interface in all metallic and most silicate inclusion assemblages in every CLIPPIR diamond and is often accompanied by hydrogen. The fluid is not thought to have existed as a free fluid phase while the diamond grew. Rather, it is interpreted to have formed as a result of hydrogen atoms exsolving out of the metallic liquid, and perhaps to some extent the silicates as well, forming CH_4 and H_2 by reacting with the surrounding diamond (Smith and Wang, 2016).

SILICATE INCLUSIONS IN CLIPPIR DIAMONDS: EVIDENCE FOR DEEP ORIGIN

The second most abundant inclusion is a mix of calcium silicates interpreted as retrogressed $CaSiO_3$-perovskite (CaPv), a perovskite-structured high-pressure mineral stable at depths beyond about 360 km (see box A and Brenker et al., 2005). The most common

BOX A: POST-ENTRAPMENT RECRYSTALLIZATION OF INCLUSIONS

Diamond excels at preserving trapped inclusions by virtue of its physical strength and chemical inertness. Even if they are protected and isolated, however, some inclusions may nevertheless recrystallize in response to the ambient temperature and pressure, especially when a diamond is transported to surface. This is true of the metallic Fe-Ni-C-S inclusions in CLIPPIR diamonds, which are thought to be trapped as a homogenous melt but later unmix into multiple phases (figure A-1). Textures within these metallic inclusions are essentially igneous, reflective of solidification and crystallization processes.

In addition to the crystallization of trapped melt inclusions, solid mineral phases can also undergo post-entrapment changes. Some minerals are only stable deep in the earth, at elevated pressure and temperature, and become unstable under conditions at the earth's surface. This is an important concept for inclusions in diamond because it explains how mineral inclusions can change after being trapped in a diamond. A mineral inclusion trapped very deep in the earth can undergo retrogression or inversion on its way to surface, meaning the inclusions we observe might be the breakdown products of some original high-pressure phase. When minerals break down, they are said to have undergone retrogression if the breakdown results in multiple phases, or inversion if the result is a single mineral phase. For example, the high-pressure mineral $CaSiO_3$-perovskite could undergo retrogression to produce two complementary minerals, larnite (β-Ca_2SiO_4) and $CaSi_2O_5$-titanite, or inversion to produce a single mineral, $CaSiO_3$-walstromite. In either case the bulk composition remains unchanged. Often, high-pressure phases are known mainly from experimental work and are referred to by their crystal structure. For example, the mineral perovskite ($CaTiO_3$) has a closely packed cubic crystal structure that is emulated by calcium silicate at high pressures, and this phase is called "perovskite" (broadly) or $CaSiO_3$-perovskite.

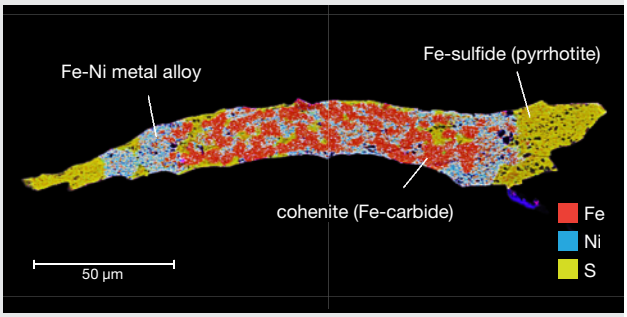

Figure A-1. An exposed polished metallic Fe-Ni-C-S inclusion. This inclusion was originally a homogeneous molten metal, but as it cooled and solidified the mixture crystallized into three separate phases: cohenite, Fe-Ni alloy, and Fe-sulfide. It is shown here as an energy-dispersive X-ray elemental map from an electron microscope, with the three phases colored according to where iron, nickel, and sulfur are more strongly concentrated. Fe (red) is concentrated in cohenite, Ni (blue) in Fe-Ni alloy, and S (yellow) in Fe-sulfide. The host diamond is a 2.14 ct offcut from a larger type IIa diamond from the Letšeng mine, Lesotho (sample Letseng_889, inclusion F). For methods, see Smith et al. (2016).

breakdown product of CaPv is $CaSiO_3$-walstromite (figure 4). Other calcium silicate phases encountered are larnite (β-Ca_2SiO_4), $CaSi_2O_5$-titanite, and, less commonly, wollastonite ($CaSiO_3$). All four phases are sometimes found together (metastably) in a single inclusion. If the inclusion contains sufficient titanium, it can be present as perovskite ($CaTiO_3$). Although it is still unclear, there may be two possible $CaSi_2O_5$ polymorphs in retrogressed high-pressure calcium silicate inclusions, corresponding to monoclinic and triclinic structures that have been observed in high-pressure experimental products (e.g., Kubo et al., 1997). Two different sets of Raman features have been interpreted as $CaSi_2O_5$-titanite. One signature encountered, as in figure 4, resembles monoclinic titanite ($CaTiSiO_5$) with its prominent 890 cm^{-1} band (see also database S3 in Smith et al., 2016). Another Raman signature corresponding to a synthetic $CaSi_2O_5$ sample (figure 2 in Nasdala et al., 2003) has also been observed in CaPv inclusions (Nasdala et al., 2003; Anzolini et al., 2016; Smith et al., 2016).

The CaPv inclusions are colorless and transparent, with surface textures ranging from flat-faced, sharp cuboctahedra to more ragged-looking irregular surfaces, especially for larger inclusions. Some inclusions have small opaque portions that are magnetic, interpreted as traces of metallic liquid trapped along with the silicate inclusion. Many CaPv inclusions possess small droplet-like satellite inclusions, all of the same mineralogy, grouped in one or more tabular lobes that appear to have been introduced from the main inclusion outward along localized cracks (figure 4B). The satellite inclusions are interpreted as the byproduct of pressure buildup sufficient to rupture

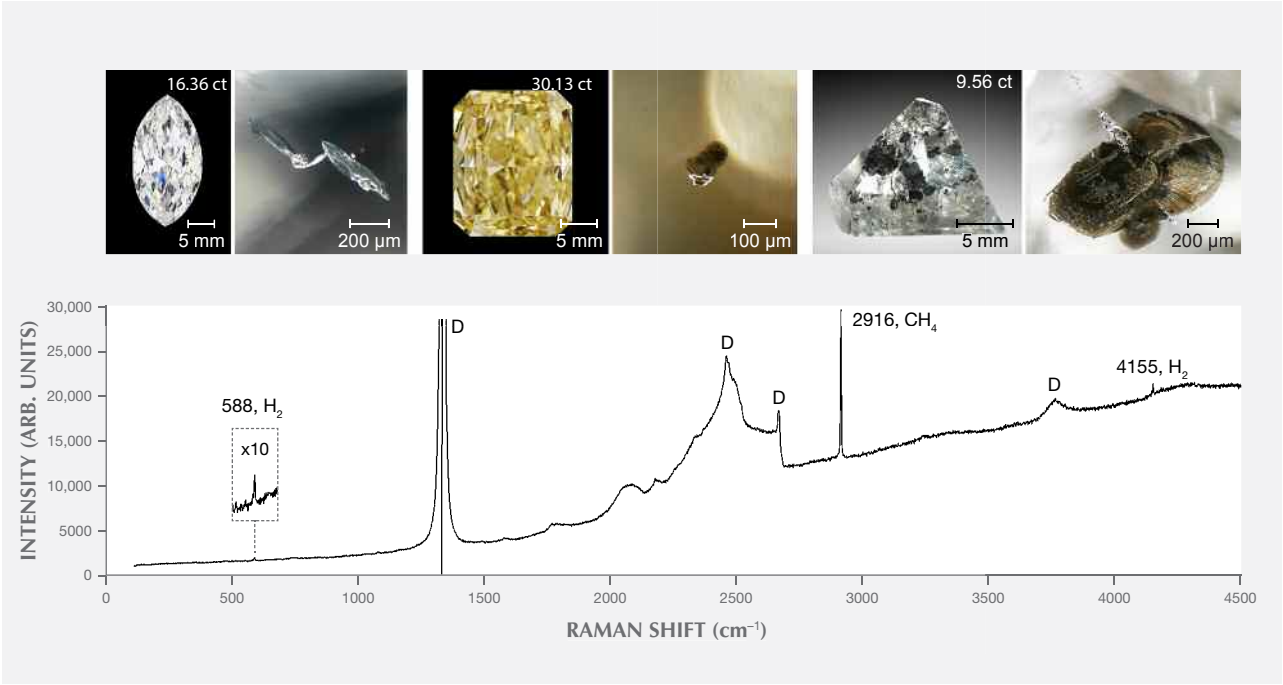

Figure 5. Metallic Fe-Ni-C-S inclusions with a representative Raman spectrum. All three CLIPPIR diamonds shown are type IIa. The faceted diamonds (left and center) are D-color and Fancy yellow-brown, respectively. The rightmost sample is a more heavily included offcut trimmed from an even larger, potentially D-color diamond. The Raman spectrum shows the typical lack of diagnostic mineral peaks (within the 100–1200 cm^{-1} range) coupled with methane (CH_4) and molecular hydrogen (H_2). Diamond Raman features are marked "D." Face-up faceted diamond photos (16.36 ct and 30.13 ct) by Jian Xin (Jae) Liao; other photos by Evan M. Smith.

the surrounding diamond, followed by injection of inclusion material out into the crack. A large volume increase of about 30% is estimated to accompany the inversion from CaPv to $CaSiO_3$-walstromite (Anzolini et al., 2016). The cracks have healed, and the diamond between individual satellite inclusions is optically continuous. Although this initial crack is healed, the main inclusion and sometimes even the satellite inclusions are each surrounded by a graphitic black fracture (figure 4B), an indication of further inclusion expansion during exhumation from the mantle by the erupting kimberlite. As a diamond is transported to the surface, the confining pressure acting on it gradually decreases and there is less pressure pushing in on its inclusions. In this situation, some inclusions push out against the diamond host, potentially causing a buildup of elastic strain and brittle rupturing around the inclusions. It is also possible that the surrounding diamond can deform plastically, thereby reducing the tendency for brittle failure. Such inclusions demonstrate the complex histories of brittle, elastic, and plastic deformation the host diamond can endure in response to inclusion pressure during ascent to surface.

An additional inclusion phase found was low-chrome majoritic garnet, a high-pressure form of garnet containing excess silica (figure 4C). The garnets are a pale orange color, again surrounded by large graphitic fractures, and sometimes have a coexisting magnetic, metallic component. The garnet provides a convenient maximum depth of derivation, since it is not stable deeper than about 750 km (Wijbrans et al., 2016). Silicate inclusion phases therefore bracket the depth between 360 and 750 km, overlapping the region of the mantle known as the mantle transition zone, which marks the transition between the upper mantle and lower mantle.

Examples of former $CaSiO_3$-perovskite (CaPv) and majoritic garnet inclusions coexisting with a metallic component and $CH_4 \pm H_2$ demonstrate a close association between the metal-only inclusions and the silicate-dominated inclusions and confirm that they are derived from a common, very oxygen-poor setting in the mantle. The best-studied example, since it

could be polished and examined in cross section with electron microscopy, is in one of the large diamond offcut samples from the Letšeng mine in Lesotho. In it, two majoritic garnets were observed, each trapped with a Fe-Ni-C-S metallic component alongside the garnet (fig S4 in Smith et al., 2016). The metallic accompaniments were a mixture of iron-carbide, Fe-Ni alloy, and Fe-sulfide, similar to the metallic inclusions seen in other diamonds containing no silicates. Again, CH_4 was present.

The silicate inclusions found in CLIPPIR diamonds are comparable to inclusions that have been described before in other sublithospheric diamonds (see summaries by Stachel et al., 2005; Kaminsky, 2012; Harte and Hudson, 2013). Here, these silicate inclusions are consistent with a mafic (eclogitic) host rock affiliation in the sublithospheric mantle. In the CLIPPIR diamond suite, however, the inclusion assemblages are somewhat different because they are associated with metal and the reduced volatiles methane and hydrogen.

CRYSTALLOGRAPHIC ORIENTATION OF METALLIC INCLUSIONS IN CLIPPIR DIAMONDS

In addition to their surprising metallic nature, the most common inclusions in CLIPPIR diamonds also have a spatial distribution that is striking. The metallic inclusions are often spatially grouped in one or more chains, all parallel to a single <111> vector (figure 6). This is a line oriented perpendicular to an octahedral {111} plane. Individual chains can waver slightly, with jogs and discontinuities, but can reach several millimeters in length. When multiple metallic inclusion chains are present, they are often parallel and define a pervasive linear fabric with no tendency to radiate from the center or otherwise align to any obvious diamond growth pattern. Instead the chains define a lineation within the diamond. The uniform, parallel, and crystallographically controlled orientation of the chains suggests they are like an overprinted fabric established after diamond growth. Cathodoluminescence or UV luminescence imaging sometimes reveals bright curviplanar features where the linear extension of an internal chain pierces the diamond surface. Figure 6 shows an example of these features extending radially from the point where an inclusion chain vector meets the polished surface. These otherwise invisible features are interpreted as healed cracks with roughly {110} orientation, of which there are three potential {110} plane orientations that intersect along the chain-defining <111>

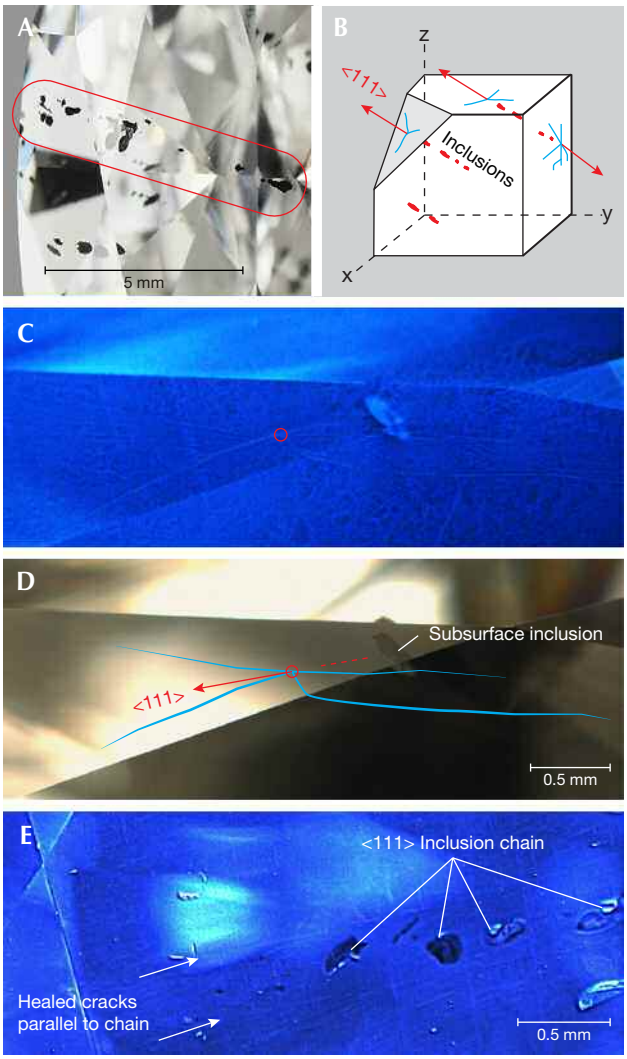

Figure 6. Metallic inclusions in CLIPPIR diamonds often occur in linear chains. A: Long, discontinuous inclusion chain in a 2.05 ct D-color type IIa diamond. B: Sketch showing a volume of diamond with multiple parallel <111> inclusion chains. Healed cracks of imperfect {110} orientation (blue) can be seen on the surface, at points where chain-defining vectors exit the diamond. C: DiamondView UV luminescence image revealing healed cracks related to a subsurface metallic inclusion in a 15.25 ct D-color type IIa diamond. Also visible are web-like dislocation networks. D: The same area shown in visible light, with blue traces drawn over the invisible healed cracks and the <111> vector extending from the inclusion, circled where the vector pierces the diamond surface. E: DiamondView image showing a <111> inclusion chain just below the surface, within the plane of the page, and two related healed cracks of {110} orientation running parallel to the inclusions. Two sets of finely spaced {111} slip traces are also seen, overprinting and cross-cutting the <111> vector and healed cracks. Photos by Evan M. Smith.

BOX B: DIAMOND DEFORMATION AS A WAY TO MAKE <111> CHAINS

Metallic inclusions in CLIPPIR diamonds frequently occur as chains of a few inclusions, aligned in a <111> crystallographic orientation (figures 3A, 3B, and 6). These chains are challenging to explain, but here we consider that they may be a consequence of diamond deformation in the mantle. At the elevated temperatures in the earth's mantle, diamond can deform plastically, though it can still develop cracks under high stress. If the 3-D stress is non-uniform and causes plastic deformation within the diamond, there will be a concentration of stress at the liquid metallic inclusions, where dislocation movement is interrupted and the inclusion itself is a strengthless fluid. Under these conditions, cracks might develop locally at the inclusion site. Given that the geometry of a <111> vector can be produced by the intersection of two or three {110} planes, the next step is to consider whether or not the diamond could crack on a {110} plane in a systematic way. In fact, brittle failure on {110} planes has been experimentally produced in diamond at elevated temperatures, concurrent with plastic deformation on {111} planes (Brookes et al., 1999). In this deformation experiment, the {110} cracks were parallel to the compressional axis.

Bulk plastic deformation of the diamond may have led to stress concentration and brittle failure localized at the metallic melt inclusions. The single <111> vector expressed by the chains could correspond to the direction of maximum compressive stress, resolved to the diamond lattice. At the inclusion site, {110} cracks can develop parallel to the compressional axis, like those observed by Brookes et al. in their deformation experiment. It would be possible to develop two or three symmetrically equivalent {110} cracks, such that the intersection of the cracks defines a short-lived dilatant <111> channel along which metallic melt inclusions can redistribute. In other words, the chains may be a redistribution of primary liquid metallic Fe-Ni-C-S inclusions, along a strain-controlled <111> direction, during brittle-plastic deformation of the diamond in the mantle. Redistribution of melt inclusions provides immediate local stress relief conducive to crack closure and healing. In two diamonds, the metallic inclusions have been observed as a planar group arranged in a {110} orientation, interpreted as a rare case of metallic liquid redistributed into a single planar {110} crack rather than the linear intersection of two or more cracks. Compared to the solid silicate inclusions, the metallic inclusions may be prone to this deformation-induced redistribution simply because they were in a liquid state. Inclusions containing both Fe-Ni-C-S metal and silicate trapped together do not exhibit the linear spatial distribution, possibly because the solid silicate portion strengthened the inclusion. It is very unlikely that the metallic liquid could have originated outside the diamond and penetrated into fine, parallel <111> channels. The graphitic {111} fractures currently visible around the Fe-Ni-C-S inclusions postdate this deformation.

The interpreted scenario of melt inclusion redistribution suggests these diamonds were deformed deep enough that the metallic inclusions were still liquid and had not unmixed. Development of the {110} healed cracks in the diamond likely predates the development of dislocation networks because dislocation networks appear to conform to the cracks rather than being crosscut by them. These two observations suggest that the development of <111> chains may have occurred in a discrete deformation episode at depth in the sublithospheric mantle. This deformation could be related to mantle convection and deep plate tectonic processes, or some other physical mechanism.

vector (see box B). The observations suggest that primary metallic melt inclusions were rearranged into chains during deformation of the host diamond at depth in the mantle. The significance is difficult to interpret without more detailed knowledge of the deformation behavior of diamond in the mantle, but likely speculation would relate diamond deformation to the pervasive deformation of mantle host rock that accompanies mantle convection.

METAL IN THE MANTLE: WHAT DOES IT MEAN?

Much of our knowledge of the earth comes from studying rocks near its surface, yet the deeper interior remains wholly inaccessible. While the continuous action of plate tectonics and the magmatism caused by it allows geologists to relate plate deformation and volcanism to Earth's deeper interior, magmas react, crystallize, and degas on their way to the surface, which changes their composition. The inevitably modified magmas make it difficult to discern the true nature of solid deeper mantle except by inference. It is well known that the increase in temperature and pressure with depth in the earth causes some minerals to break down and new minerals to form that are only stable at the more extreme pressure and temperature conditions. When considering the deep interior of the earth, this effect is fundamental. High-pressure experiments are used by scientists in the field of mineral

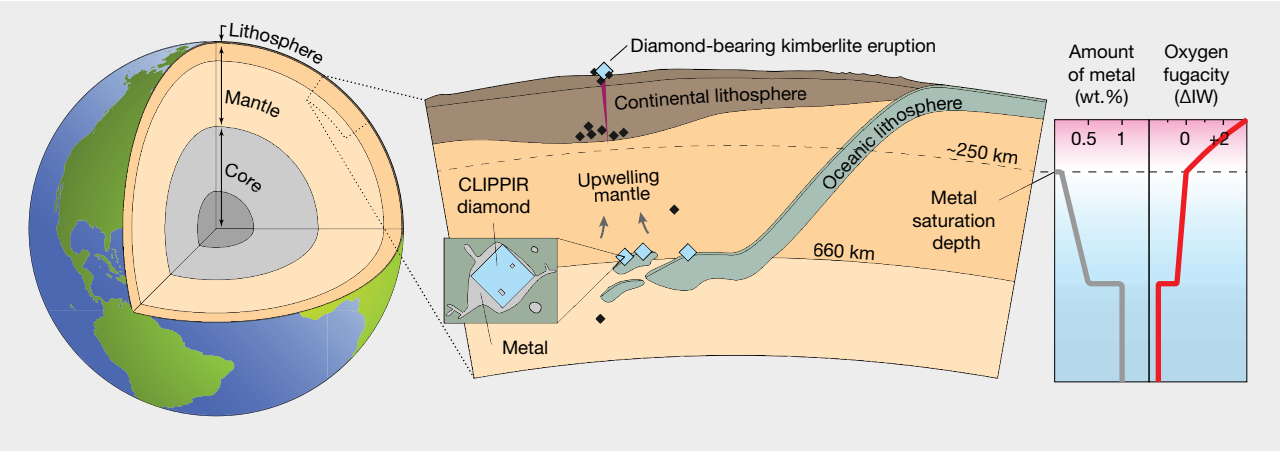

Figure 7. Cross section of the uppermost 1,000 km of the earth (center) illustrating the origin of CLIPPIR diamonds, shown as large blue diamond symbols. Smaller black diamond symbols indicate other varieties of diamond formed mainly in the continental lithosphere. Oceanic lithosphere subducted into the mantle provides the rocks necessary to explain the CaPv and majoritic garnet inclusions. CLIPPIR diamonds are thought to grow from liquid metal. Following growth, they may be carried upward with thermally or chemically buoyant upwelling mantle material and entrained in a kimberlite eruption to the surface. Profiles at the right show how the amount of metal in the mantle is expected to increase with depth starting from 250 km down, reaching up to approximately 1 wt.% below 660 km and buffering oxygen fugacity to reducing conditions (ΔIW, log units relative to the iron-wüstite buffer). Profiles after Rohrbach and Schmidt (2011).

physics to predict what kinds of mineral assemblages will occur even within the lower mantle. One important prediction to come out of these considerations of mineral physics is the idea that there is a depth, around 250 km, below which metallic iron might become one of the stable phases within deep mantle rocks (Frost et al., 2004). This prediction for metallic iron is fundamental to understanding the basic properties of the mantle. We know that at the bottom of the mantle it is in direct contact with the iron-nickel metal of the core, whereas at the top of the mantle, iron metal is not even stable during mantle melting. What happens, mineralogically speaking, in between?

The mechanism thought to be responsible is the progressive increase in the capacity for silicate minerals to host Fe^{3+} (iron with a 3+ oxidation state) relative to Fe^{2+} at high pressures (Ballhaus, 1995; Frost et al., 2004). The preference for Fe^{3+} in certain minerals under extreme pressure induces a disproportionation reaction, whereby valence electrons in the existing Fe^{2+} atoms are redistributed according to the reaction $3Fe^{2+} \rightarrow 2Fe^{3+} + Fe^{0}$. The Fe^{3+} is partitioned into the silicates, but the Fe^{0} separates into its own metallic phase. Iron disproportionation is thought to generate up to about 1 wt.% metal in the lower mantle (Frost et al., 2004; Rohrbach et al., 2007). Nickel, carbon, sulfur, and other elements are expected to dissolve into this metallic phase. This prediction is based on experiments (Bell et al., 1976; Ballhaus, 1995; Frost et al., 2004; Rohrbach et al., 2007; Rohrbach and Schmidt, 2011) but has never before been verified by actual observation of mineral grains.

The Fe-Ni-C-S melt inclusions in CLIPPIR diamonds are interpreted to be samples of such a metallic liquid, thereby confirming the fundamental process of Fe^{2+} disproportionation at depth (Smith et al., 2016) and providing evidence for a metallic liquid mechanism for diamond formation. This is the reason why CLIPPIR diamonds are so significant for earth science. The metal has large-scale implications for the behavior and evolution of the mantle over geologic time because it will influence the storage and cycling of the many elements that dissolve into it, such as oxygen, carbon, nitrogen, and hydrogen. The tendency for metallic iron to react with oxygen is expected to regulate or buffer the oxygen fugacity (the chemical availability of oxygen in the mantle) and maintain reducing conditions in the ambient mantle below about 250 km depth (figure 7). The projected low oxygen fugacity below 250 km, shown in figure 7, is a direct consequence of Fe^{2+} disproportionation (Rohrbach and Schmidt, 2011).

GEOLOGICAL ORIGIN OF CLIPPIR DIAMONDS

The consistent association of the mineral assemblages found in CLIPPIR diamonds with metal and methane, and its limitation to the CLIPPIR category, indicate that these diamonds form in a unique way. The CaPv and majoritic garnet inclusions, as well as the light carbon isotopes of the diamonds themselves, imply an association with subducted eclogite at extreme depths, likely within 360–750 km in the convecting mantle (Smith et al., 2016). This is much deeper than other gem diamonds, nearly all of which contain much more nitrogen (type I) and form in the lowermost parts of thick, old continental lithosphere at depths of 150–200 km. This extreme depth is, however, within the range of other rare "superdeep" diamonds in the sublithospheric mantle (figure 7).

The source of the carbon that crystallized into diamond is also important. Carbon has two stable isotopes, ^{13}C and ^{12}C, whose ratio varies according to the source, such as ambient mantle carbon or subducted, organic carbon. Variably light carbon isotopes in CLIPPIR diamonds, having $^{13}C/^{12}C$ ratios lower than the convecting mantle (Smith et al., 2016), suggest derivation from organic carbon (e.g., Kirkley et al., 1991; McCandless and Gurney, 1997), which implies the carbon was originally sourced at Earth's surface and then subducted.

CLIPPIR diamonds, as described above, appear to grow in close association with metallic liquid in the sublithospheric mantle. In this deep environment, the metallic Fe-Ni-C-S melt inclusions are hypothesized to represent small retained traces of the actual growth medium (Smith et al., 2016). Experiments and routine HPHT synthetic diamond growth processes show that iron-nickel mixtures are effective media at elevated temperatures and pressures, similar to the conditions in the deeper mantle. Diamond growth from metallic liquid could help explain the large size of CLIPPIR diamonds and their near-complete lack of nitrogen. Interestingly, the $CH_4 \pm H_2$ fluid jackets surrounding inclusions in natural CLIPPIR diamonds are a feature also seen in metal/carbide inclusions in HPHT synthetic diamonds (Smith and Wang, 2016), further supporting their interpretation as primary melt inclusions. Natural CLIPPIR diamonds may have crystallized inside small pockets of molten metallic liquid in Earth's deep mantle (figure 7). Small droplets of this metallic liquid would have occasionally been trapped within the diamonds as they grew, preserving the inclusion assemblages that we now sample.

As shown in figure 7, the eclogitic host rocks responsible for the silicate inclusions in CLIPPIR diamonds likely represent a basaltic crustal layer of the oceanic lithosphere that was subducted into the deeper underlying mantle. Below a depth of approximately 250 km, iron disproportionation can lead to metal saturation in mantle rocks. Both eclogite and the surrounding peridotite, including the mantle portion of the oceanic lithosphere, have the potential to generate metal by disproportionation. The source of the metal can be constrained by its bulk composition, roughly estimated as $Fe_{0.61–0.75}Ni_{0.10–0.13}C_{0.15–0.20}S_{0.05–0.12}$ based on the measured composition and relative cross-sectional area of cohenite, Fe-Ni alloy, and Fe-sulfide exposed in four polished inclusions (Smith et al., 2016). The modest Ni/(Ni+Fe) ratio (<0.2) is lower than the 0.3–0.5 range proposed for metal compositions precipitating in upper mantle peridotites (Rohrbach et al., 2014). Combined with the notion that the metallic liquid should be nearly immobile, tending to become trapped as disconnected droplets in the intergranular spaces of silicate mantle rocks (Rohrbach and Schmidt, 2011; Rohrbach et al., 2014), it is tempting to infer that the metal was generated locally, within the eclogitic host rocks where the diamonds grew. However, the observed Ni/S and Ni/(Ni+Fe) ratios in the inclusions are significantly higher than expected for equilibrium with eclogite (e.g., Ni/S=0.3 and Ni/(Ni+Fe)=0.02 reported for a metallic inclusion found in eclogitic garnet [Jacob et al., 2004]). To explain this discrepancy, the metal could have formed in equilibrium with peridotite (e.g., Zhang et al., 2016) and subsequently migrated into the eclogite before diamond crystallization occurred, but this scenario would imply significant metal precipitation, segregation, and liquid metal mobility in order for large diamonds to ultimately crystallize. If metal in the mantle is typically distributed along grain boundaries in silicates at low abundances of around 1%, then segregation and mobilization of the liquid metal may rely on deformation of surrounding rocks. However, other rock types or localized irregular rock compositions within the proposed growth setting of subducted oceanic lithosphere could also play a role in the metal and diamond formation. Further inclusion analyses and experimental constraints are needed to clarify the exact provenance of the metal.

Metallic iron has already been suggested to play a role in the formation of other types of superdeep diamonds, by its proposed ability to reduce subducted carbonate species (CO_3^{2-}) to diamond (C), also called "redox freezing" (Rohrbach and Schmidt, 2011). It is not clear how or even if carbonate would be involved

in CLIPPIR diamond growth since an oxygen-deficient mantle region is a prerequisite for metallic inclusions. But the expected high calcium content of carbonate might be one explanation for the abundance of CaPv inclusions as a reaction byproduct (Walter et al., 2008; Bulanova et al., 2010; Harte and Richardson, 2012; Thomson et al., 2016). Alternatively, other forms of subducted carbon such as abiogenic, organic carbon could be involved where carbonate does not play a significant role. The main point here is that metallic Fe-Ni-C-S inclusions clearly show that the metallic iron-rich phase plays the key role for CLIPPIR superdeep diamond formation.

Once formed, CLIPPIR diamonds, like other sublithospheric diamonds, require some mechanism to transport them upward to be sampled by kimberlite magmatism and brought to surface where they are mined. The mechanism is uncertain but may involve thermochemically buoyant, ascending solid mantle that is part of the general upwelling associated with mantle convection (figure 7) prior to being entrained in erupting kimberlite. The dynamic action of the mantle may be cryptically recorded in the crystal strain in CLIPPIR diamonds. There is a remarkably strong association between CLIPPIR diamonds and dislocation networks (De Corte et al., 2006) that can be better understood in light of the present study. This web-like feature, rare in other diamonds, is visible in cathodoluminescence or UV fluorescence imaging in almost all 83 CLIPPIR samples examined (e.g., figure 6C). The network is interpreted as a dislocation structure arising from plastic deformation followed by recovery (Hanley et al., 1977). The high temperatures afforded by a sublithospheric origin as well as the minimal nitrogen contents in CLIPPIR diamonds are conducive to the development of dislocation networks. These diamonds have witnessed severe conditions in the deep mantle—a likely consequence of mantle convection. Earth's mantle convects in the solid form, introducing strain on the scale of the mineral lattice at extremely high pressure. Despite their often exquisite gem quality, these diamonds have an internal structure that preserves evidence of this strain and their journey from the deep mantle to the surface.

CONCLUSIONS

It has long been recognized that a curiously high proportion of large, gem-quality diamonds are type IIa, an otherwise rare designation. But now we have learned that these special gems, termed CLIPPIR diamonds, actually form in a unique way, in a different part of the mantle compared to other kinds of diamonds. Many inclusion-free, nitrogen-deficient diamonds, especially those with dislocation networks, are expected to belong to the CLIPPIR category (figure 2). The "superdeep" (i.e., sublithospheric) origin of CLIPPIR diamonds, which leaves them free of inclusions associated with shallower, lithospheric mantle diamond host rocks, helps explain why exploration geologists and miners have never been able to correlate these diamonds with traditional indicator minerals (Bowen et al., 2009; Gurney and Helmstaedt, 2012). The rarity and extraordinary value that have made research study prohibitive over the years also contributes to this fact. Indicator minerals such as chrome-rich pyrope and ilmenite, the fragments of diamond host rocks from the lithospheric mantle keels of Archean continents, are useful for finding lithospheric diamonds. CLIPPIR diamonds, however, originate deeper in the mantle, far below the lithosphere where these indicator minerals are not stable and cannot be included. Finding CLIPPIR diamonds is all the more difficult. Predicting their ore grade, even in promising mines, requires large bulk sampling and carries great uncertainty.

Large and pure diamonds are nevertheless a highly sought prize. Prior to the study by Smith et al. (2016), there was no accepted model describing how these large type IIa diamonds form in nature. We can now appreciate that these exceptional diamonds are coincidentally some of the most scientifically valuable samples of our planet's interior. They are a window into the deep convecting mantle, providing a glimpse through the shroud of Earth's tectonic plates and surface magmatism.

Previous experiments and theory have predicted for many years that parts of the deep mantle below about 250 km contain small amounts of metallic iron and have limited available oxygen. Now, the metallic inclusions and their surrounding methane and hydrogen jackets in CLIPPIR diamonds provide physical evidence to support this prediction. This is a key observation for our understanding of planet Earth, having broad implications for its geologic evolution through time, such as the behavior and cycling of carbon and hydrogen, which are the primary fluxes for rock melting and the generation of new crust. Confirming the existence of metallic iron containing nickel, carbon, sulfur, and other elements as a discrete liquid also impacts our understanding of the seismic velocity and thermal and electrical conductivity of the mantle, as well as the way it deforms and flows. This result is a sign that there is still much to be learned from diamonds and their inclusions.

ABOUT THE AUTHORS

Dr. Smith is a research scientist, and Dr. Wang is vice president of research and development, at GIA in New York. Dr. Shirey is a senior scientist in the Department of Terrestrial Magnetism of the Carnegie Institution for Science in Washington, DC.

ACKNOWLEDGMENTS

The authors thank GIA's Ulrika D'Haenens-Johansson and Paul Johnson for assistance with sample selection, Alex Balter for help handling data for figure 2, and Jian Xin (Jae) Liao for acquiring face-up images of the diamonds in figures 4 and 5. This work was completed with the support of GIA's Liddicoat Postdoctoral Research Fellowship program.

REFERENCES

Anzolini C., Angel R., Merlini M., Derzsi M., Tokár K., Milani S., Krebs M., Brenker F., Nestola F., Harris J. (2016) Depth of formation of $CaSiO_3$-walstromite included in super-deep diamonds. *Lithos*, Vol. 265, pp. 138–147, http://dx.doi.org/10.1016/j.lithos.2016.09.025

Anzolini C., Prencipe M., Alvaro M., Romano C., Vona A., Lorenzon S., Smith E.M., Brenker F.E., Nestola F. (2017) Depth of formation of super-deep diamonds: Raman barometry of $CaSiO_3$-walstromite inclusions. *American Mineralogist*, in press.

Ballhaus C. (1995) Is the upper mantle metal-saturated? *Earth and Planetary Science Letters*, Vol. 132, No. 1-4, pp. 75–86, http://dx.doi.org/10.1016/0012-821X(95)00047-G

Bell P., Mao H., Weeks R., Valkenburg A. (1976) High pressure disproportionation study of iron in synthetic basalt glass. *Carnegie Institution of Washington Yearbook 1975*, pp. 515–520.

Bowen D.C., Ferraris R.D., Palmer C.E., Ward J.D. (2009) On the unusual characteristics of the diamonds from Letšeng-la-Terae kimberlites, Lesotho. *Lithos*, Vol. 112S, pp. 767–774, http://dx.doi.org/10.1016/j.lithos.2009.04.026

Breeding C.M., Shigley J.E. (2009) The "type" classification system of diamonds and its importance in gemology. *G&G*, Vol. 45, No. 2, pp. 96–111, http://dx.doi.org/10.5741/GEMS.45.2.96

Brenker F.E., Vincze L., Vekemans B., Nasdala L., Stachel T., Vollmer C., Kersten M., Somogyi A., Adams F., Joswig W. (2005) Detection of a Ca-rich lithology in the Earth's deep (> 300 km) convecting mantle. *Earth and Planetary Science Letters*, Vol. 236, No. 3-4, pp. 579–587, http://dx.doi.org/10.1016/j.epsl.2005.05.021

Brookes E., Greenwood P., Xing G. (1999) The plastic deformation and strain-induced fracture of natural and synthetic diamond. *Diamond and Related Materials*, Vol. 8, No. 8-9, pp. 1536–1539, http://dx.doi.org/10.1016/S0925-9635(99)00080-1

Bulanova G.P., Walter M.J., Smith C.B., Kohn S.C., Armstrong L.S., Blundy J., Gobbo L. (2010) Mineral inclusions in sublithospheric diamonds from Collier 4 kimberlite pipe, Juina, Brazil: Subducted protoliths, carbonated melts and primary kimberlite magmatism. *Contributions to Mineralogy and Petrology,* Vol. 160, No. 4, pp. 489–510, http://dx.doi.org/10.1007/s00410-010-0490-6

Crookes W. (1909) *Diamonds*. Harper & Brothers, London, New York.

De Corte K., Anthonis A., Van Royen J., Blanchaert M., Barjon J., Willems B. (2006) Overview of dislocation networks in natural type IIa diamonds. *G&G*, Vol. 42, No. 3, pp. 122–123.

Frezzotti M.L., Tecce F., Casagli A. (2012) Raman spectroscopy for fluid inclusion analysis. *Journal of Geochemical Exploration*, Vol. 112, pp. 1–20, http://dx.doi.org/10.1016/j.gexplo.2011.09.009

Frost D.J., Liebske C., Langenhorst F., McCammon C.A., Trønnes R.G., Rubie D.C. (2004) Experimental evidence for the existence of iron-rich metal in the Earth's lower mantle. *Nature*, Vol. 428, No. 6981, pp. 409–412, http://dx.doi.org/10.1038/nature02413

Gurney J.J., Helmstaedt H.H. (2012) The origins of type IIa diamonds and their enhanced economic significance. *10th International Kimberlite Conference, Short Abstract No. 10IKC-123*, pp. 247–248.

Gurney J.J., Helmstaedt H.H., Richardson S.H., Shirey S.B. (2010) Diamonds through time. *Economic Geology*, Vol. 105, No. 3, pp. 689–712, http://dx.doi.org/10.2113/gsecongeo.105.3.689

Hanley P.L., Kiflawi I., Lang A.R. (1977) On topographically identifiable sources of cathodoluminescence in natural diamonds. *Philosophical Transactions of the Royal Society of London. Series A, Mathematical and Physical Sciences*, Vol. 284, No. 1324, pp. 329–368, http://dx.doi.org/10.1098/rsta.1977.0012

Harte B., Hudson N.C.F. (2013) Mineral associations in diamonds from the lowermost upper mantle and uppermost lower mantle. *Proceedings of 10th International Kimberlite Conference: Volume 1*, pp. 235–253.

Harte B., Richardson S. (2012) Mineral inclusions in diamonds track the evolution of a Mesozoic subducted slab beneath West Gondwanaland. *Gondwana Research*, Vol. 21, No. 1, pp. 236–245, http://dx.doi.org/10.1016/j.gr.2011.07.001

Iron in diamonds (1877) *Scientific American Supplement*, Vol. 3, p. 877.

Jacob D.E., Kronz A., Viljoen K.S. (2004) Cohenite, native iron and troilite inclusions in garnets from polycrystalline diamond aggregates. *Contributions to Mineralogy and Petrology,* Vol. 146, No. 5, pp. 566–576, http://dx.doi.org/10.1007/s00410-003-0518-2

Kaminsky F. (2012) Mineralogy of the lower mantle: A review of 'super-deep' mineral inclusions in diamond. *Earth-Science Reviews*, Vol. 110, No. 1-4. pp. 127–147, http://dx.doi.org/10.1016/j.earscirev.2011.10.005

Kaminsky F.V., Wirth R. (2011) Iron carbide inclusions in lower-mantle diamond from Juina, Brazil. *Canadian Mineralogist*, Vol. 49, No. 2, pp. 555–572, http://dx.doi.org/10.3749/canmin.49.2.555

Kirkley M.B., Gurney J.J., Otter M.L., Hill S.J., Daniels L.R. (1991) The application of C isotope measurements to the identification of the sources of C in diamonds: a review. *Applied Geochemistry*, Vol. 6, No. 5, pp. 477–494, http://dx.doi.org/10.1016/0883-2927(91)90048-T

Kubo A., Suzuki T., Akaogi M. (1997) High pressure phase equilibria in the system $CaTiO_3$-$CaSiO_3$: stability of perovskite solid solutions. *Physics and Chemistry of Minerals*, Vol. 24, No. 7, pp. 488–494, http://dx.doi.org/10.1007/s002690050063

McCandless T.E., Gurney J.J. (1997) Diamond eclogites: comparison with carbonaceous chondrites, carbonaceous shales, and microbial carbon-enriched MORB. *Russian Geology and Geophysics*, Vol. 38, No. 2, pp. 394–404.

Mikhail S., Guillermier C., Franchi I.A., Beard A.D., Crispin K., Verchovsky A.B., Jones A.P., Milledge H.J. (2014) Empirical evidence for the fractionation of carbon isotopes between diamond and iron carbide from the Earth's mantle. *Geochemistry,*

Geophysics, Geosystems, Vol. 15, No. 4, pp. 855–866, http://dx.doi.org/10.1002/2013GC005138
Moore A.E. (2014) The origin of large irregular gem-quality type II diamonds and the rarity of blue type IIb varieties. *South African Journal of Geology*, Vol. 117, No. 2, pp. 219–236, http://dx.doi.org/10.2113/gssajg.117.2.219
Nasdala L., Brenker F.E., Glinnemann J., Hofmeister W., Gasparik T., Harris J.W., Stachel T., Reese I. (2003) Spectroscopic 2D-tomography: Residual pressure and strain around mineral inclusions in diamonds. *European Journal of Mineralogy*, Vol. 15, No. 6, pp. 931–935, http://dx.doi.org/10.1127/0935-1221/2003/0015-0931
Rohrbach A., Schmidt M.W. (2011) Redox freezing and melting in the Earth's deep mantle resulting from carbon-iron redox coupling. *Nature*, Vol. 472, No. 7342, pp. 209–212, http://dx.doi.org/10.1038/nature09899
Rohrbach A., Ballhaus C., Golla-Schindler U., Ulmer P., Kamenetsky V.S., Kuzmin D.V. (2007) Metal saturation in the upper mantle. *Nature*, Vol. 449, No. 7161, pp. 456–458, http://dx.doi.org/10.1038/nature06183
Rohrbach A., Ghosh S., Schmidt M.W., Wijbrans C.H., Klemme S. (2014) The stability of Fe–Ni carbides in the Earth's mantle: Evidence for a low Fe–Ni–C melt fraction in the deep mantle. *Earth and Planetary Science Letters*, Vol. 388, pp. 211–221, http://dx.doi.org/10.1016/j.epsl.2013.12.007
Scarratt K., Shor R. (2006) The Cullinan diamond centennial: A history and gemological analysis of Cullinans I and II. *G&G*, Vol. 42, No. 2, pp. 120–132, http://dx.doi.org/10.5741/GEMS.42.2.120
Sharp W.E. (1966) Pyrrhotite: A common inclusion in South African diamonds. *Nature*, Vol. 211, No. 5047, pp. 402–403, http://dx.doi.org/10.1038/211402b0
Shirey S.B., Shigley J.E. (2013) Recent advances in understanding the geology of diamonds. *G&G*, Vol. 49, No. 4, pp. 188–222, http://dx.doi.org/10.5741/GEMS.49.4.188
Smith E.M., Wang W. (2016) Fluid CH_4 and H_2 trapped around metallic inclusions in HPHT synthetic diamond. *Diamond and Related Materials*, Vol. 68, pp. 10–12, http://dx.doi.org/10.1016/j.diamond.2016.05.010
Smith E.M., Shirey S.B., Nestola F., Bullock E.S., Wang J., Richardson S.H., Wang W. (2016) Large gem diamonds from metallic liquid in Earth's deep mantle. *Science*, Vol. 354, No. 6318, pp. 1403–1405, http://dx.doi.org/10.1126/science.aal1303
Stachel T., Harris J.W. (2009) Formation of diamond in the Earth's mantle. *Journal of Physics: Condensed Matter*, Vol. 21, No. 36, 364206, http://dx.doi.org/10.1088/0953-8984/21/36/364206
Stachel T., Brey G., Harris J.W. (2005) Inclusions in sublithospheric diamonds: glimpses of deep earth. *Elements*, Vol. 1, No. 2, pp. 73–78, http://dx.doi.org/10.2113/gselements.1.2.73
Thomson A.R., Walter M.J., Kohn S.C., Brooker R.A. (2016) Slab melting as a barrier to deep carbon subduction. *Nature*, Vol. 529, No. 7584, pp. 76–79, http://dx.doi.org/10.1038/nature16174
Walter M.J., Bulanova G.P., Armstrong L.S., Keshav S., Blundy J.D., Gudfinnsson G., Lord O.T., Lennie A.R., Clark S.M., Smith C.B., Gobbo L. (2008) Primary carbonatite melt from deeply subducted oceanic crust. *Nature*, Vol. 454, No. 7204, pp. 622–625, http://dx.doi.org/10.1038/nature07132
Wijbrans C.H., Rohrbach A., Klemme S. (2016) An experimental investigation of the stability of majoritic garnet in the Earth's mantle and an improved majorite geobarometer. *Contributions to Mineralogy and Petrology*, Vol. 171, No. 5, pp. 1–20, http://dx.doi.org/10.1007/s00410-016-1255-7
Wilks J., Wilks E. (1994) *Properties and Applications of Diamond*. Butterworth-Heinemann, Oxford, UK.
Zhang Z., Dorfman S.M., Labidi J., Zhang S., Li M., Manga M., Stixrude L., McDonough W.F., Williams Q. (2016) Primordial metallic melt in the deep mantle. *Geophysical Research Letters*, Vol. 43, No. 8, pp. 3693–3699, http://dx.doi.org/10.1002/2016GL068560

GEM VIRTUOSOS: THE DREHERS AND THEIR EXTRAORDINARY CARVINGS

Robert Weldon, Cathleen Jonathan, and Rose Tozer

The German towns of Idar and Oberstein (now Idar-Oberstein) have a rich history of gem cutting and carving, notably in agate. The profession continues to be passed on from one generation to the next, as it has been for over five centuries. One of these families, the Drehers, has worked with gem materials for 13 generations. Gerd Dreher apprenticed gem carving with his father starting in 1955, while Gerd's son, Patrick, began his apprenticeship in 1988. While they carve individually, occasionally they work together as a team. The family creates fine carvings from agates and from single crystals of high-quality rough gem minerals. These unique pieces are extraordinarily detailed and utilize natural color zoning to achieve a remarkably lifelike effect.

Viewed from any direction, the gem carvings by the father-and-son team of Gerd and Patrick Dreher are remarkably lifelike. Agate toads appear bumpy, glistening, and slippery. Brimming with personality, their eyes appear to follow the viewer around the room. A carved tiger lily emerges from banded agate (figure 1) as a velvety, dappled flower, its petals enticingly curling inward. And on the backs of these petals, details of the flower's physiognomy are scrupulously maintained. Much like the gem materials from which they are carved, these works are one-of-a-kind creations.

Decades of experience between the two imparts virtuosity to their work, as well as a sense of humor often depicted in the subjects. Today, Gerd is globally acknowledged as a master of the craft, while Patrick has emerged from the younger generation, adding new carving techniques to the family repertoire. This enhances the formidable range of skills that have been passed down through the Dreher family for 13 generations.

Following in the path of their ancestors, the Drehers' ability to render the anatomy of flora and fauna in astonishing detail demands an intimate knowledge of their subject matter, not to mention a deep understanding of the characteristics and attributes of the gem materials they carve. The Drehers study rough gem material, sometimes for years. From these observations they conceive a three-dimensional outcome and then set to work bringing the stone to life (figure 2). A growing collection of diamond-sintered tools, and a thorough understanding of how to use them, underpins their closely guarded lapidary techniques.

IDAR-OBERSTEIN'S GEM INDUSTRY

An understanding of the environment that gave rise to the Dreher dynasty—as well as hundreds of other celebrated practitioners of the lapidary arts—is essential to appreciating their story. Idar and Oberstein (figure 3), two picturesque German towns separated by the Nahe River in the state of Rhineland-Palatinate, were united in 1933 to form Idar-Oberstein.

This area in southwestern Germany, nestled in the Hunsrück mountain range, became famous for its agate and quartz deposits, as well as its residents' expertise in gem-related professions such as mining and cutting and more recently goldsmithing. Idar lore suggests that agate nodules and quartzes, such as chalcedony, jasper, carnelian, and petrified wood, were discovered by farmers as they plowed their fields centuries ago (figure 4). Agate mining and cutting flourished there for at least five hundred years. Some believe the Romans who conquered the region used Idar's agates more than two thousand years ago. A cameo found at Hidera, a Roman settlement in the mountains above present-day Idar, suggests this ancient glyptic

See end of article for About the Authors and Acknowledgments.
GEMS & GEMOLOGY, Vol. 53, No. 4, pp. 404–422,
http://dx.doi.org/10.5741/GEMS.53.4.404

Figure 1. This Gerd Dreher lily carving (2005) is from a single piece of Brazilian agate and measures 11.0 cm in length. His skills are on exhibit through his use of the material and his technique, such as the curled petals that demonstrate a wealth of detail even on their undersides. The leaf, stamen, and enameled pistil accents are crafted from 18K gold and set with diamonds. Patrick Dreher's citrine mouse (2015), 6.0 cm in length, shows attention to the animal's stance and demeanor as well as fine detail in the carving of the fur. Photo by Robert Weldon/GIA, courtesy of the William F. Larson family.

use of its agates (Rapp, 2002). Other scholars dispute the Roman connection, but there is agreement that the deposits were mined during the Middle Ages. Cutters worked with gem materials from the area, and by the fourteenth century the region's agate cutting industry was established (Ball, 1931). Traditionally, the gem cut-

Figure 2. Natural bands of color in a single piece of jasper were used to accentuate Gerd Dreher's 1993 carving of an orangy red toad sitting on a green leaf (left). The small cross section to the right shows how he used the gem's natural color banding to create the effect. The finished piece measures 10.20 cm in length. Photo by Robert Weldon/GIA, courtesy of Leslie Hindman Auction House.

Figure 4. This agate with an amethyst-lined cavity exhibits banding that is typical of the Hunsrück deposit near Idar-Oberstein. The slice measures 27.94 cm in length. Photo by Robert Weldon/GIA, courtesy of Friedrich August Becker Edelsteine.

ting trade has been centered in Idar, with jewelry manufacturing and related professions evolving in neighboring Oberstein and other hamlets (Frazier, 1978).

In the early days of the agate cutting industry in Idar, water from nearby rivers—the Nahe, the Idarbach, and others—provided energy used to turn massive sandstone wheels for cutting (Frazier, 1978). Large wheels, up to three meters in diameter, were used to shape the agate's exterior. Cutters from the area developed a technique in which they lay stom-

Figure 3. Left: The town of Oberstein as it looked in the late 1700s. The picturesque Schloss Oberstein (the castle at the top of the hill) and Felsenkirche (the church built into the wall of the mountain) have changed little since this engraving was made. Colorized by Robert Weldon, from Collini (1776), courtesy of the Richard T. Liddicoat Library and Information Center. Right: Oberstein, as photographed in late 2015, bears a remarkable similarity to the sketch from nearly 250 years ago. Photo by Robert Weldon/GIA.

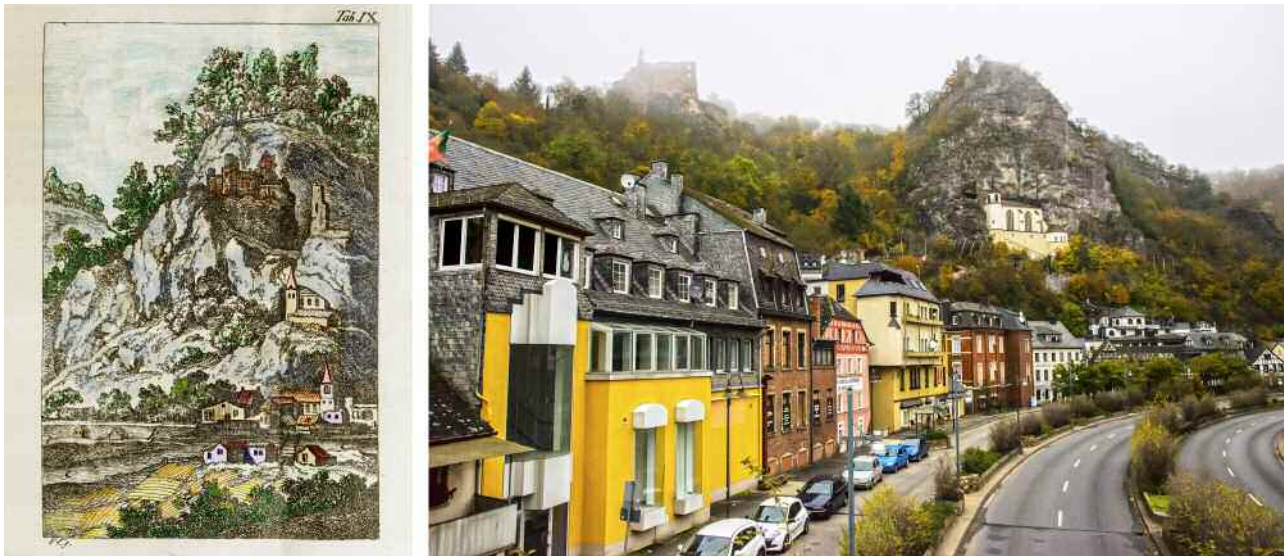

ach-down on a wooden bench. This position, with their feet pressed against the floor, or against a block of wood nailed to the floor, gave them the necessary leverage to push the gem material against the rotating wheel and cut it (figure 5). The first record of a water mill used to grind stone was in 1454 (Gerdt, 2017). A Grinder's Guild document dating back to 1609 bears witness to the profession, including strong advice to its members: "No stranger must acquire the trade of a grinder, but the craft must be handed down from father to son" (Hadley, 1984).

It was long, difficult work that demanded physical strength. Smaller wheels were used to refine the interior—to hollow out preform bowls, for example. Accounts passed down through the Dreher family

In Brief

- Idar and Oberstein, two German towns united in 1933, have an agate carving tradition that dates back to the Middle Ages.
- The Dreher family has been involved in the agate trade near Idar-Oberstein for 13 generations. The modern Dreher family, believed to have carved animal figures for Fabergé in the 19th century, has produced three-dimensional carvings for five generations.
- Modern carving tools allow for much greater detail in hardstone carving.
- The Drehers' superb library of animal images taken from various angles and studies of live animals gives their carvings exceptional detail and realism.

note that agate cutters rose at 4:00 a.m. and went to the water mills in Vollmersbach to await their turn at the wheel. Much of the work had to be done around farming obligations since cutting alone could not support the tradesmen. Throughout the small artisan workshops of Idar, family secrets learned at the cutting wheel were passed down through generations. Gem carving techniques and individual styles evolved with specific creative refinements and specialties that in many cases could be attributed to different carvers or their families (Dreher, 1979).

Gem cutters later developed foot-powered devices to cut the agates, which was followed by the advent of electric-powered engines to turn the spindles. These refinements allowed cutters to sit upright rather than lying on their stomachs. One technique did not change: While in many other parts of the world the gem material is held stationary and the craftsman moves a flexible tool around it to form the desired shape, Idar's cutters have always held the gem rough, as steadily as they can, in two hands.

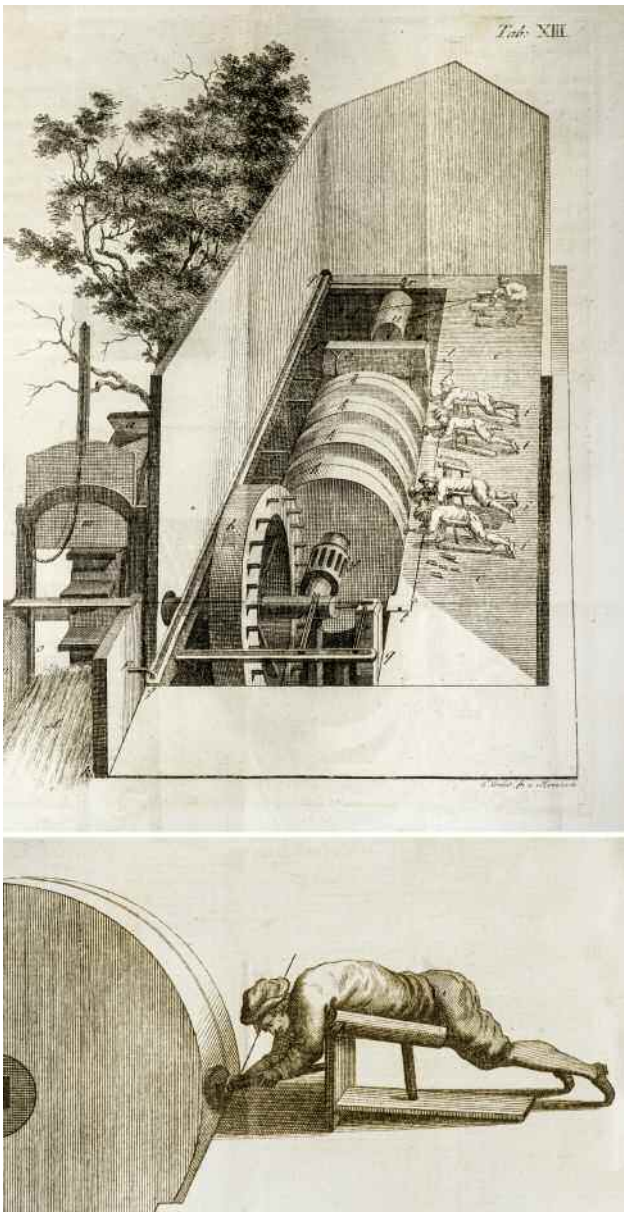

Figure 5. Top: This engraving from a 1776 book by Colosimo Collini, who explored the agate mining regions of southern Germany, shows a water mill cross-section in Oberstein along the Nahe River. The river current rotates the water wheel, which turns a geared axis. The gears turn the large sandstone wheels used to grind and form agate. Bottom: Another engraving illustrates in detail the arduous cutting process practiced by the German agate cutters, who used their bodies and the wheel to work the object. Courtesy of the Richard T. Liddicoat Library and Information Center.

Figure 6. Gerd Dreher shapes the preform of the jasper toad seen in figure 2. Gerd and Patrick Dreher both use a fixed-spindle technique while holding the gem material in their hands, a carving technique that has been used in Idar-Oberstein for centuries. Courtesy of the Dreher family.

This practice continues today. The gem is moved around a fixed spindle, progressively grinding down the material. A wide variety of diamond tools are mounted on these spindles, depending on the effect that is needed, and the speed can range from 3,000 to 11,000 revolutions per minute (rpm). According to Patrick Dreher, both the spindles and the diamond tools are manufactured in Idar-Oberstein to each cutter's specifications. Gradually, the process reveals the carver's vision (figure 6).

A dramatic change in the supply of agate and quartz occurred in the early nineteenth century. The Hunsrück deposit was nearing depletion following centuries of exploitation. The resulting decline in centuries-old mining traditions could have spelled the end of Idar's cutting trade. Fortunately, between the 1820s and 1850s, German explorers and farmers homesteading in southern Brazil found new and vastly richer sources for agate and quartz along the border with Uruguay. The agate and quartz were discovered the same way they had been in Idar centuries before: by plowing the fields. Starting in 1825, shipments of the rough gem material made their way to Idar. The quantity and quality of the Brazilian agate surpassed anything that had been known from the Hunsrück deposit. According to a *Scientific American* report from the time, up to 300 tons of agate were shipped each year to Idar and Oberstein, where some 6,000 people were employed in the trade ("Where agates come from," 1882). Other Brazilian gems such as quartz, tourmaline, topaz, and beryl were eventually imported, greatly expanding the town's offerings. The variety and availability of gem materials brought new opportunities and challenges for the cutting center.

Germany exported much of its new material to French artists in the mid-1800s, during the waning days of Romanticism. Paris was a magnet for artists of all disciplines, including fine art stonecutters and gem engravers. The new Brazilian agate spurred a revival of gem engraving and carving, enabling cutters to create cameos, intaglios, and seals using its multicolored layers for relief (Lindemann, 2017).

Young craftsmen from Idar began flocking to Paris, learning refined engraving and cameo carving techniques from Parisian masters. The start of the Franco-Prussian War in 1870, however, hastened the Germans' return to their native land. These artists, who now had abundant raw imported material at home, were soon able to surpass the skills they had learned in France. With the sudden influx of skilled carvers, Idar's renaissance as a gem center was well on its way. Many artists formed engravers' guilds upon their return, with more than 230 members in Idar and Oberstein (Pauly, 2012). The guilds helped train apprentices and enabled members to hone their cutting and carving skills. They also established a stable pricing structure for products. These developments cemented Idar-Oberstein's modern role as a center for agate cutting and engraving. The new skills acquired in Paris also prepared the cutters for the development of three-dimensional carving.

THE DREHER DYNASTY

Accounts suggest that one of the most admired cutters and engravers in nearby Vollmersbach during the late 1800s was Wilhelm Dreher (1840–1900). His meticulous work was widely commissioned both in Germany and internationally. An agate bowl of Wilhelm's, weighing 43 kilograms, was sent to French emperor Napoleon III (Dreher, 1979). Other items were sent to British royalty. One of Wilhelm's sons, possibly Karl (1861–1943), produced a lapis lazuli bowl for Emperor Nicholas II of Russia in the early 1900s. While the whereabouts of the bowl are unknown today, its sale was documented in the Dreher family history (Dreher, 1979). Karl Dreher's work, and that of other German artists at the time, marked the beginning of Idar's three-dimensional gem-carving tradition.

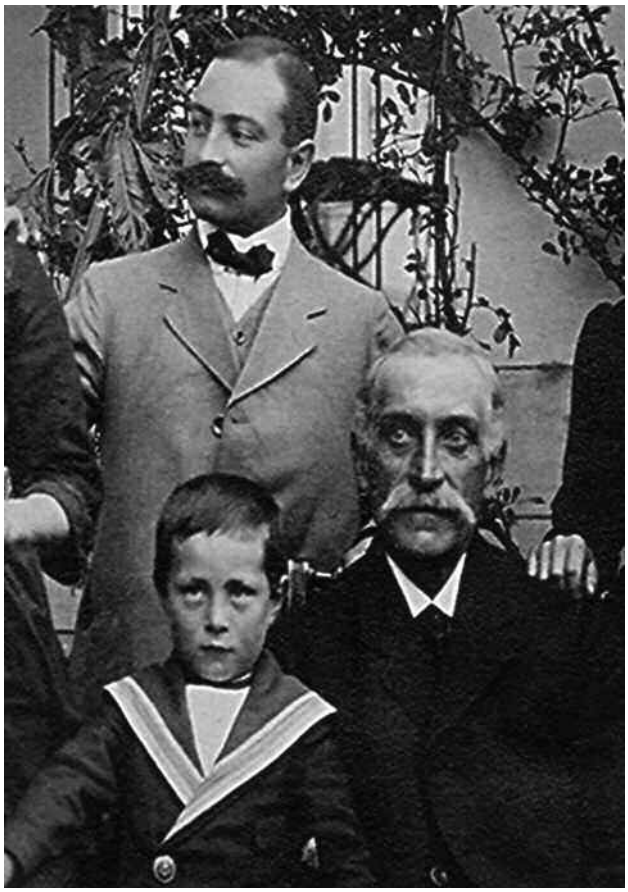

Figure 7. Three generations of Drehers (clockwise from top): Hermann Dreher (1886–1960), Karl Dreher (1861–1943), and a young Paul Dreher (1910–1968). Courtesy of the Dreher family.

The Dreher lineage has been traced back to 1620, but the family believes their ancestors began working with gems from the region much earlier. Some details were recorded in birth, marriage, and death certificates. Dreher activities were also gleaned from property ownership records, particularly with regard to lapidary mills the family bought, owned, or sold over time.

Unfortunately, many Idar and Oberstein records before 1620 were destroyed during the Thirty Years' War (1618–1648), a religious conflict in central Europe. This period witnessed considerable devastation of churches and the loss of parish records. Destruction of records was repeated in both World Wars, leading to ambiguities about the provenance of some important unsigned works of art, where the craftsmen cannot be verified with certainty. This was true for the Drehers and many other notable agate cutting families in Idar.

Wilhelm's son Karl was the first in the modern line of Drehers (figure 7) who developed skills as gemstone carvers, instead of simply cutters. As a young man he trained under a master carver who had returned from Paris, learning how to carve cameos, monograms, and other ornaments. These skills greatly expanded the Drehers' repertoire as they began to add engraving and carving to their skills. With the increased exposure to international carving styles and art movements, the family's worldview began to expand as well.

Meanwhile, Karl Wild, a contemporary of Karl Dreher who was related to the Dreher family, saw opportunities outside of Idar and traveled to Russia, acquiring the nickname "Russ-Karl." There he not only sold finished carvings and objects of art by Karl Dreher and others from Idar but also took orders and brought back raw materials (such as Russian lapis lazuli) to be carved. The lapis lazuli bowl mentioned earlier is one such piece.

THE DREHERS DURING THE ERA OF FABERGÉ

The Dreher family, like many others in Idar, relied primarily on a series of brokers to sell their work. One notable gem dealer was Moritz Stern, who brought specific orders to Idar from abroad. These orders were placed with the town's best carvers. Among those who recognized Idar's lapidary talent, and who would soon use Stern's services, was Carl Fabergé, who developed an appreciation for hardstone cutting while traveling through Florence, Dresden, and Idar in the late 1880s (von Habsburg, 1988). Fabergé was also influenced by Japanese *netsuke*[1] carvings, amassing a collection of some 500 pieces. These were popular items from sixteenth-century Japanese clothing.

As a result of these influences, lapidary orders coming into Idar at the turn of the twentieth century included specific requests from Fabergé in St. Petersburg. Fabergé developed small plaster models of animals, which were supplied to the gem cutters and replicated in stone (Adams, 1988). These works were either assembled pieces or objects made from a single piece of stone. After the finished pieces were returned to Fabergé, his workmasters would apply embellishments such as gold legs and feet (Wild, 1981). Patrick Dreher credits these Fabergé orders

[1] *Netsuke* refers to a toggle or button adorned with a miniature carving, often depicting animals, made from ivory, wood, lacquer, bone, or metal.

Figure 8. Fabergé representatives provided plaster models, such as the toad on the left, as a sample for German carvers in the Idar region to reproduce in agate. The Drehers have kept this plaster model for generations. Photo by Patrick Dreher, courtesy of the Dreher family. Right: Gerd Dreher's multicolored jasper toad (1985), measuring 6.5 cm in height, was carved from the family's Fabergé plaster keepsake. Photo by Robert Weldon/GIA, courtesy of the William F. Larson family.

with changing the family's focus from the simple cutting of agates toward carving in more artistic forms. Karl Dreher's son, Hermann (1886–1960), is one of the artists who provided carvings purchased by Fabergé. The Drehers say these works were faithfully carved from plaster models provided by Fabergé craftsmen (figure 8, left; Ovchinnikov, 2017). Although these models were considered worthless after the hardstone work was done (figure 8, right), and most were lost to time and history, the family managed to keep one such model.

This period marks the earliest shift to three-dimensional gem carvings. The Dreher family maintains only two such early carvings in its possession: the rock crystal bowl seen in figure 9, and the figure of a gem carver with a bowl in figure 10.

Figure 9. This rock crystal quartz bowl by Hermann Dreher, ca. 1910, is one of the oldest items in the family's possession. Photo by Robert Weldon/GIA, courtesy of the Dreher family.

Figure 10. Paul Dreher's figure of a gem carver holding a bowl (1935) is another of the earlier pieces in the Dreher collection. Photo by Robert Weldon/GIA, courtesy of the Dreher family.

Even with family members brokering some of the business, the hardstone carvings went unsigned and were subsumed under the Fabergé name. The venerable Russian firm relied to some extent on outside vendors for a variety of goods they could not manufacture themselves. The items supplied had to be of the highest caliber and craftsmanship, reflecting expertise simply not found in Russia at the time.

German lapidary craft is acknowledged in the Fabergé literature. References indicate that the first carved hardstone animals likely came from Idar. In *Fabergé*, Dr. Géza von Habsburg writes: "Fabergé took up the search for hardstone carving outside of Russia… [H]is journey led him to Idar-Oberstein, a little town specialized in the cutting and engraving of Brazilian agate." Von Habsburg singles out the German carver Alfred Heine, working for the Wolff Company, who "produced stone animals for Fabergé." He goes on to say that "Fabergé's numerous commissions brought about a new flowering for the old stone cutting center" (von Habsburg, 1988). This is also acknowledged by Russian experts. "It is a well-known fact that the Idar-Oberstein masters made large quantities of carvings for Fabergé," said Galina Gabriel, a member of the International Association of Art Critics and the Russian Union of Artists who spoke at the 2015 International Fabergé Conference in St. Petersburg.

After 1908, Fabergé acquired the Woerffel factory in St. Petersburg to handle the firm's lapidary needs. Orders for the carved animals, commissioned through Fabergé and originally carved in Idar, consequently slowed in Germany. After World War I (1914–1918), such carvings came to an abrupt halt. Widespread social unrest in Russia culminated in the 1917 Russian Revolution and the execution of Emperor Nicholas II and his family in July 1918. Fabergé lost all of its wealthy Russian patrons. The firm was nationalized, closing its doors in November 1918 (Snowman, 1962; Faber, 2008). The destruction of records in both Germany and Russia left a gap in the full understanding of Idar carvers' links to Fabergé. Nonetheless, the seeds had been sown for the growth of some of the world's greatest three-dimensional gem carvers.

MASTER CARVERS: FROM FATHER TO SON

Having learned the trade from his father, Hermann, Paul Dreher (1910–1968; figure 11) was third in a line of carving masters. The absence of influence from Fabergé or any other major buyer provided Paul with greater creative latitude, allowing him to render animal sculptures with rich variations. A delicate, life-like deer and a large, sinuous puma are two Paul Dreher carvings owned by the family (figures 12 and 13). In homage to his innovations, the firm today

Figure 11. Paul Dreher (1910–1968) working in his studio. Courtesy of the Dreher family.

Figure 12. Viewed from any angle, this Paul Dreher doe (1957) is remarkably lifelike. These realistic pieces marked a new design direction in animal carvings for the Dreher family. Photo by Robert Weldon/GIA, courtesy of the Dreher family.

Figure 13. This puma by Paul Dreher (1965) shows exquisite overall form and beauty in its smoothness, but without the nuanced details that diamond-sintered tools would later allow. It measures 32.5 cm in length. Photo by Robert Weldon/GIA, courtesy of the Dreher family and the Deutsches Edelsteinmuseum.

bears the name Paul Dreher Edelsteine und Gravuren (Paul Dreher Precious Stones and Engraving).

Aside from his large, single-stone carvings, Paul Dreher also experimented with combinations of several carved gem materials in composite sculptures. These animal figures became very popular and were of such exceptional quality that they were sometimes misidentified as Fabergé pieces. According to Gerd Dreher (2012), "We were rather surprised to see two original carvings made by my father in the second edition (1962) of the book *The Art of Carl Fabergé* by A. Kenneth Snowman." The mistake is somewhat understandable: Unsigned pieces by the Drehers, and others in Idar-Oberstein, continued to be sold through brokers or dealers. The style once inspired by Fabergé had endured for decades, long after the legendary company had ceased to exist.

Why did the pieces go unsigned? The brokers had the luxury of travel and fluency in languages used in international commerce. They often presented the pieces as a shared Idar-Oberstein quality brand. Based in Idar-Oberstein and abroad, these brokers sold the carvings internationally or in some cases passed them along as examples of their own work (P. Dreher, pers. comm., 2017). This was considered normal business practice. There were positive and negative effects of this business model. On one hand, carving families in Idar-Oberstein did not have to concern themselves with marketing and sales. They could concentrate on producing the work and take the time to develop new skills. The obvious drawbacks, however, were that the carvers did not receive recognition, build a reputation, or understand their own market. This business arrangement lasted well into the career of Gerd Dreher. The unfortunate result was that the Dreher name was not widely recognized outside of Idar-Oberstein.

Figure 14. "Love Birds" (1979) was created during Gerd Dreher's early years, when he carved various stones and composited them to form a whole sculpture. The birds are carved from aventurine quartz, black agate, and yellow jasper with obsidian tail feathers. They are perched on a base of preserved petrified wood. The piece measures 25.40 cm tall. Photo by Robert Weldon/GIA, courtesy of Leslie Hindman Auction House.

Gerd Dreher, born in 1939, was trained by his father starting at the age of 16, in the time-honored local tradition of passing these skills from father to son (see "Idar-Oberstein's Gem Industry" section above). Between the 1960s and 1980s, Gerd followed a path sim-

Figure 15. "Red Baron" (Gerd Dreher, 2015) is a mostly rubellite tourmaline toad that gradually transitions to green tourmaline toward the base. The toad measures 7.10 cm in height and weighs 280 g (1,400 ct). Photo by Robert Weldon/GIA, courtesy of the William F. Larson family.

ilar to that of his father, carving various gem materials, often in ways that could be composited to create animal figures such as the one in figure 14.

After Gerd Dreher took over the family business, he realized the need to change how his carvings were brought to market. He finally began to sign Dreher animal carvings in the 1970s, and collectors quickly seized upon the crisp logo they saw etched along the edges of the artwork. Dreher carvings began to emerge from relative obscurity.

He observed that his artwork would benefit from carving single pieces of gem material—demonstrating what can be done with a single gem—albeit with accents, or an occasional quartz base to help a carving stand upright. Accents include gold fins for fish, feathered crests for birds, and tails for various animals. These accents are carved in wax and then cast in gold. Eyes are also added features, and they are sufficiently unique as to require particular attention. They are made from small translucent to opaque sections of agate, or black agates cut as cabochons. The translucent areas are lined internally with gold leaf. This results in the shimmering appearance seen in an amphibian's eye (figure 15) or the brilliant, dark stare of a mouse. Both appear startlingly similar to real eyes.

By 1980, much finer diamond-sintered tools became available. "It allowed us to carve mammals, reptiles, and amphibious creatures with much finer detail than before," Patrick Dreher recalls. These tools could also cut faster. But as Gerd Dreher cautioned his son, who was an apprentice by then, "The tools are not meant for us to produce faster. We will only use them to produce better." Elaborate carving techniques they continue to master show refined, individual detail in fur, where even single strands can be identified (see box A). Varying degrees of carving depth create selected areas of translucency or opacity,

Box A: The Drehers and the Gem Carving Process

Idar-Oberstein's artists exert far more control over the shape, symmetry, details, and final polish of finished work than they did fifty years ago, thanks largely to modern diamond-sintered tools. The speed of cutting (the revolutions per minute of the spindle) has also increased. However, the Drehers prefer to use today's tools to increase the quality and fine detail of the work, rather than to improve turnaround time. The family has maintained their proprietary secrets, but they continue to use the traditional technique of holding the gem material against a spindle to grind away gem material. The following images and short descriptions provide a step-by-step progression resulting in a final carved object of art.

- An agate nodule (figure A-1) is carefully chosen and sliced using a diamond saw into an angular, blocked shape, from which the subject size and dimensions are determined. The Drehers sometimes sketch the animal onto the flat surfaces of the agate using a pencil or marker. This helps them to visualize the finished carving and determine how the material's color zoning will define the animal's characteristics and personality. Gerd and Patrick Dreher use color zoning in a single block of agate to determine how the animal will be posed. Both the agate and dozens of photos of the subject—in this case, a mouse—are studied to ensure anatomical correctness.
- In the second photo, Gerd Dreher has defined the three-dimensional object (a mouse), including the outlines of its tail and ears. All of the aspects of the creature's demeanor, stance, and position have been carved into the agate (figure A-2). The Drehers use 4–6 cm diamond-sintered tools at this stage, spinning at 8,000–9,000 revolutions per minute (rpm), with continuous water drip for cooling and cleaning. Patrick Dreher explains, "This step is one of the most difficult states, because you have to cut away a lot of material; but you can't cut too much because you cannot get it back if there is a mistake." This stage is also critical for observation: The artist must frequently pull away from the grinding to assess the material, sketch new drawings, study color separations, and correct any mistakes. In agates, the color

Figure A-1. The first step in carving is to saw the agate nodule, revealing the interior banding and zones of color. Photo by Robert Weldon/GIA, courtesy of the Dreher family.

Figure A-2. Once the concept for a mouse subject is conceived, large sections of the agate are removed in the initial carving stage. Photo by Robert Weldon/GIA, courtesy of the Dreher family.

borders are sometimes hard to see, which may require a redesigned mouse if color patterns are off.

- At this stage, the mouse has much finer characteristics, with translucent ears and more pronounced facial characteristics and tail (figure A-3). The Drehers generally use smaller diamond-sintered tools at this stage, varying from 5 mm to 2 cm. Different steps in carving require an assortment of tools and shapes as the carver exerts variable speeds (between 8,000 and 14,000 rpm) with a continuous water drip. The carver determines the thickness and fineness of the piece by varying the applied pressure. At this stage, the object, which must now have the animal's correct proportions, begins to appear lifelike.
- Gerd Dreher finishes this mouse (figure A-4) by carving extremely detailed strands of fur, defining the translucency and delicacy of the ears, adding small dimples denoting the mouse's whiskers, and fashioning the characteristics of the rock the mouse is standing on (consider that the mouse and rock on which he stands are all *one* piece). At least three degrees of polishing occur: pre-polish, fine polish, and high polish. Additionally, some sandblasting takes place on the rock portion for a different degree of texture. These polishing details are performed with small brushes and diamond powder (grits not disclosed). The powder is mixed with oils to create slurry, which can easily be cleaned with water. Dreher leaves small divots in the carving in which to place the animal's eyes, which are carved from black agate and prepared separately, then glued into place (figure A-4). Other accents may be added at this time as well, such as a gold tail or gold-feathered crests. Paraffin is never used to finish off the carvings, ensuring they will last for generations with proper care and handling. Both carvers serve as each other's quality control, Patrick Dreher adds. "It is always great to have a new pair of eyes look at something. But this I know is true: If my father says it is finished, it is finished!"

Figure A-3. Smaller tools are used for additional definition and detail. Photo by Robert Weldon/GIA, courtesy of the Dreher family.

Figure A-4. The final step is to carve minute details including fur, dimples, and muscles, and to polish the finished product. Photo by Robert Weldon/GIA, courtesy of the Dreher family.

Figure 16. Gerd Dreher's evocative, softly undulating carved agate (2004) emulates coral. With delicately carved translucent agate fins, the fish appears to swim through the coral. The piece measures 25 cm high and weighs 1,960.8 g (9,804 ct). Photo by Robert Weldon/GIA, courtesy of the William F. Larson family.

which often evoke comparisons with actual animals. Ears on a mouse or rabbit are strikingly thin and translucent, yet they still exhibit the detailed dimples and folds seen in a live animal. Advancements in the quality of the tools, merged with a deep understanding of the subject's appearance, imbue the creatures with stunning personalities (figures 16 and 17). Art critic Galina Gabriel considers the present generation of Drehers consummate masters, and Gerd specifically the "world's most prestigious gemstone carver" (Gabriel, 2015; Gabriel, 2017).

THE DREHER PHILOSOPHY

Neatly categorized shoeboxes line the walls of the tiny Dreher studio, packed with photographs and sketches of fauna in various poses. Some are copied from books or magazines for reference. The photographs also feature animals that are live-captured by the Drehers to act as models for the carvers. It is the Drehers' impressive collection of images and sketches that gives the family a depth of understanding about their subjects that few other carvers enjoy. Patrick Dreher recalls that on one occasion he was looking for a "preening" mouse. He could not photograph the desired pose in a captured mouse until a tiny bit of strawberry jam was strategically smeared on a small patch of the mouse's fur. It had the intended effect: The mouse soon went to work cleaning himself. The photographs, which are taken from multiple angles, help the Drehers interpret and in-

Figure 17. This Gerd Dreher chameleon (2000), measuring 12.4 cm tall and weighing 2,390 ct, was carved from a single crystal of gem-quality Brazilian green beryl. Photo by Robert Weldon/GIA, courtesy of Silverhorn Jewelers.

Figure 18. A startled mouse (1997) assesses his options from inside an upturned mushroom. Carved by Gerd Dreher from smoky quartz, it measures 12.4 cm wide. Photo by Robert Weldon/GIA, courtesy of Leslie Hindman Auction House.

corporate three dimensions into the finished object. These live animals fulfill their role as models, resulting in carvings such as the startled mouse (figure 18). After that, they are carefully released back into the wild, unaware that their likenesses are sought by collectors around the world.

The Drehers carve a variety of rough gem material ranging from 5 to 9 on the Mohs hardness scale, though their stated preference is always agate. They appreciate agate's toughness but also its wide-ranging color variations, which guarantee distinctive works of art. Carving into the layers of color zoning in agate provides the "canvas" and opportunity for three-dimensionality. Dreher carvings also appear regularly in rock crystal quartz, ruby-in-zoisite, beryl, topaz, rhodonite, obsidian, and tourmaline, among other gem materials. Here, too, the Drehers use color zoning in single crystals to their advantage, or to reveal a story in the carving.

Collectors generally supply the raw material in crystal form or as rough chunks. It is always valuable and often extremely rare. One notable example is a toad (figure 19) carved from a single piece of Brazilian tourmaline crystal provided by California gem mineral collector William Larson.

"This piece came to us in colors of black, red, green, and black again," Patrick Dreher recalls. "As we began to remove the black material, we saw a thin layer of blue we hadn't seen before. This increased the value and became the head of the toad. The pink and red colors that emerged became the body of the toad, and the green color became the feet. This 'Queen of the Toads' is the most valuable piece we have ever carved."

Patrick, born in 1970, apprenticed with his father, in keeping with the family's tradition. "My father is

Figure 19. This particolored tourmaline (2013) revealed its rich colors as it was being cut. Gerd Dreher did not know at the outset that the toad's head would be blue. It measures 10.8 cm tall and weighs 1,226 g (6,130 ct). Photo by Robert Weldon/GIA, courtesy of the William F. Larson family.

Figure 20. Gerd Dreher's "Three Young Birds" (2006), a carving in Ukrainian heliodor, incorporates part of the natural beryl face in the base. The accents are 18K gold. The piece measures 11.5 cm tall and weighs 922 g (4,610 ct). Photo by Robert Weldon/GIA, courtesy of Silverhorn Jewelers.

the best teacher I could possibly get," he says. Both work together at their home-based studio. "It's not like a traditional job where you go home after work. I'm home already. And my boss is also my father!" Patrick explains that he was exposed to the craft as a toddler, with ample opportunities to absorb his father's carving methods. Actual hands-on work began by the age of 18. In 1997, Gerd and Patrick traveled to Rio Grande do Sul, Brazil's southernmost state, and brought back 3.5 tons of handpicked agate rough, which they continue to work with to this day.

The 1980s and '90s also provided incredible new gemstone finds, such as large beryl crystals from Ukraine that were available after the fall of the Soviet Union. Gem materials were also emerging from Brazil and from newer sources such as Afghanistan, East Africa, and Madagascar. This gemstone windfall dovetailed nicely into the family's growth, with two decades of some of the finest, largest, single-crystal gem materials that had been found in the twentieth century. A young bird's nest lavishly carved from an enormous hexagonal Ukrainian green heliodor (figure 20) exemplifies the era. Sensitive to the beauty of the geometric etched pits on the crystal, Gerd Dreher left one face of the beryl intact with the gem's natural surface. Similarly, a mouse carved from African ruby and zoisite (figure 21) illustrates the massive ornamental materials beginning to emerge from Africa at the time.

Patrick says that he and his father consistently carve 12–20 new works every year, each of which may take 300–400 hours to complete. Father and son work both independently and collaboratively on pieces and continue to find new collectors to supply them with exceptional gem material.

Figure 21. Gerd Dreher's ruby-in-zoisite mouse (1993), carved from a single piece of rough, has sapphire cabochon eyes and an 18K gold tail. It measures 6.8 cm tall and weighs 246 g (1,230 ct). Photo by Robert Weldon/GIA, courtesy of Silverhorn Jewelers.

Box B: Dreher Carving Quality Factors

Figure B-1. Gerd Dreher's "Tree Frog" (2002) was carved from chrysoprase and meticulously worked so that the frog's feet would curve to grasp the gold accents. The base of the carving is rock crystal quartz; the stem of the pond reed is 18K gold. The combined artwork weighs 1,032 g. Photo by Robert Weldon/GIA, courtesy of the Deutsches Edelsteinmuseum.

Quality of the Rough: The rough gem material must be extraordinary and rare, such as larger agates with unusual color banding and strength of color. This allows for the development of a themed finished carving. In transparent gems, the material is often crystalline and devoid of any obvious inclusions, resulting in clean, luminous carvings.

Quality of the Carving: The carving must maintain lifelike proportions throughout, and symmetry from all viewing angles should be comparable to an actual animal's appearance (figure B-1).

Details: Dreher carvings are studies in minute detail. How are these details rendered? Does the fur of a bear overlap? Are the ears of a mouse fine and translucent?

Use of Material: The Drehers sometimes spend years looking at a rough gemstone before starting to carve it. Considerable thought, planning, and execution go into the use of the gem's color zoning to convey lifelike features, or to distinguish an animal from its environment.

Uniqueness: Dreher carvings are always original works of art. Though some poses might be similar, no two carvings are identical; there is always variation because they are carved in different materials and at different times.

Signatures: Contemporary work is signed by Patrick or Gerd Dreher. In figure B-2, "GD" is Gerd Dreher and "PD" is Patrick Dreher.

Composite Works: Some Gerd Dreher carvings are composites of various gem materials. This generally dates a piece before the 1980s, expressing the material, the know-how, the demand, and the tools that were available at the time.

Single-Gem Carvings: Large single-crystal carvings reflect the company's change in artistic direction and philosophy in the 1980s. Single-gem carvings reveal not only the rarity of the gem material but also the Drehers' ability to render a complete three-dimensional carving from it.

Accents: Gold accents, such as tails and feathers, carved eyes and quartz bases, are used in both composite and single-gem carvings (figure B-1).

Figure B-2. Unlike their Idar-Oberstein predecessors, the Drehers started signing their contemporary work in 1975. The signature on the left is that of Gerd Dreher, while Patrick Dreher's initials are seen on the right. Photos by Robert Weldon/GIA.

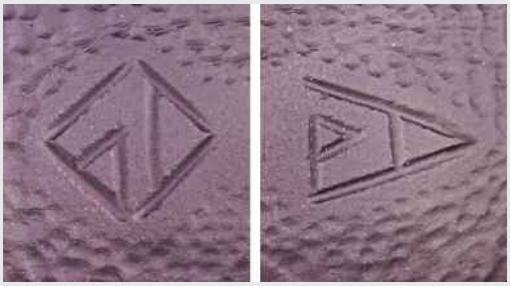

Figure 22. This hippopotamus in citrine (2015) shows Patrick Dreher's mastery in rendering the animal, which exhibits a highly polished, glistening surface. It measures 12.0 cm long and weighs 526 g (2,630 ct). Photo by Robert Weldon/GIA, courtesy of the William F. Larson family.

Patrick's own mastery of the craft was realized in a dramatic fashion when, after decades of apprenticeship, he detailed a plan to carve a rounded but completely smooth and glassy hippopotamus out of citrine quartz. "It cannot and should not be done—you'll be wasting material," his father chided. Nevertheless, Patrick was steadfast in his resolve, and his father ultimately agreed the piece was masterful (figure 22).

Patrick has since carved a number of important pieces, including a starfish from a strawberry quartz specimen that in its rough state had concealed a secret. It was not until he began the removal of unwanted or damaged sections that the strawberry quartz revealed pale amethyst and colorless rock crystal quartz in the layers beneath. The color variations in the amethyst became a coral reef on an ocean floor of rock crystal (figure 23).

Inside their home studio, the Drehers take turns at the spindle. A collection of diamond-sintered tools, in different sizes and numbering in the hundreds, await their turn at the workstation. These tools, and the skilled use of them, bring out extremely fine detail. With a few exceptions, it is this detail that defines the present era. In his day, Paul Dreher carved unique large items like the puma and deer, in which the personality came to life in the carvings' well-defined but smooth, soft surfaces, reflecting a mastery that was limited only by his tools. Today's carvings have generally lost that smoothness

Figure 23. Patrick Dreher's strawberry quartz starfish (2014), carved from a crystal similar to the one shown on the right, revealed layers of amethyst and rock crystal as he carved into the stone. The "strawberry" portion of the single piece became the shiny starfish, resting upon an amethyst coral. The rock crystal quartz section was carved as the ocean floor. The starfish measures 13.6 cm tall and weighs 1,279.50 g (6,397.50 ct). Photo by Robert Weldon/GIA, courtesy of the William F. Larson family.

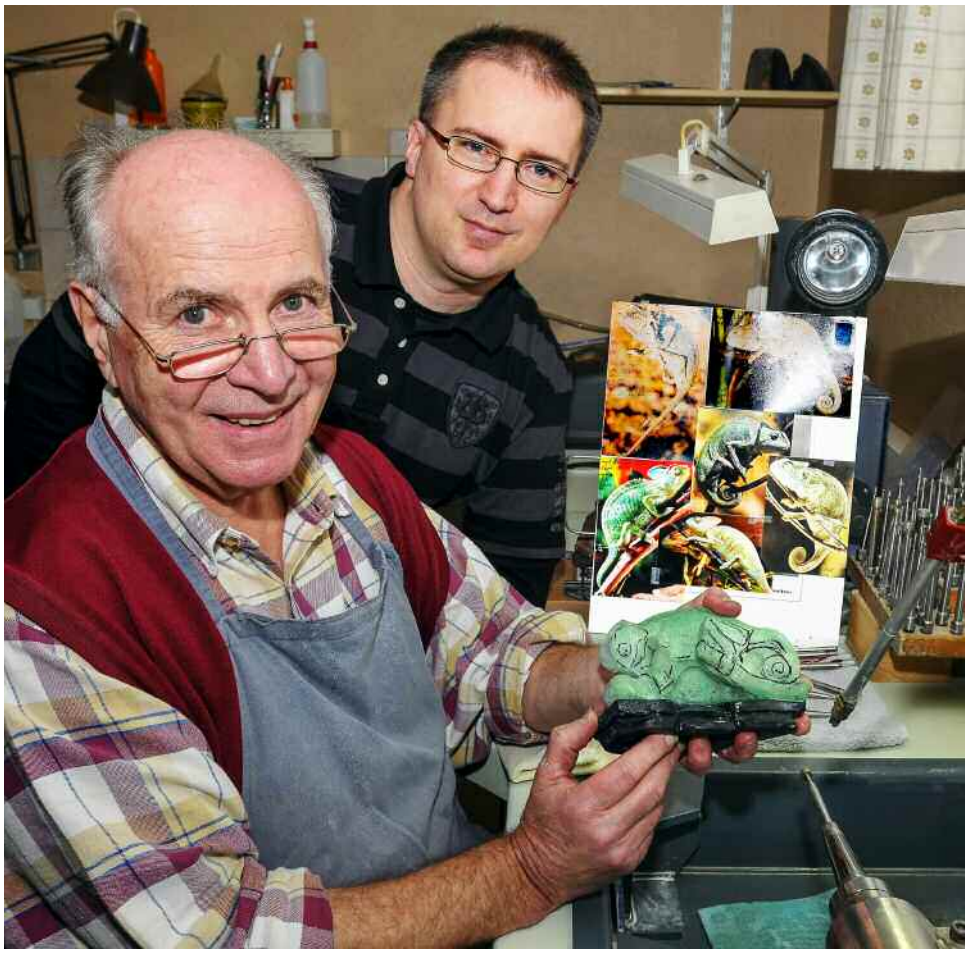

Figure 24. Gerd and Patrick Dreher in their studio. Courtesy of the Dreher family.

in favor of extraordinary detail, attention to realism, and quality (see box B).

CONCLUSIONS

For centuries, the German towns of Idar and Oberstein have been known for agate cutting. Joined as one town before World War II, the region developed into a cutting and carving center for colored gemstones. Two of its principal carvers, Gerd and Patrick Dreher, can trace their family's association with agate back thirteen generations, with the last five involved in three-dimensional gem carving. Father and son (figure 24) are considered by many to be the world's greatest living gem carvers, and their work continues to be acquired by collectors around the world.

ABOUT THE AUTHORS

Mr. Weldon (rweldon@gia.edu) is director, Ms. Jonathan (cjonathan@gia.edu) is a research librarian, and Ms. Tozer (rtozer@gia.edu) is senior librarian at the Richard T. Liddicoat Gemological Library and Information Center in Carlsbad, California.

ACKNOWLEDGMENTS

The authors wish to thank the Dreher family for giving us the opportunity to interview them, for helping us understand their history, and for opening the doors to their house and studio to photograph carvings. We thank Anette Fuhr, director of the Deutsches Edelsteinmuseum in Idar-Oberstein, for our interview with her and her permission to photograph selected pieces from the museum. Thanks also to Dieter Hahn, chairman of the Foundation of the Deutsches Edelsteinmuseum, for his insights into the history of the Idar-Oberstein region. GIA has assembled a large collection of photos of Dreher carvings over nearly a decade, starting when gem dealer Michael Ridding of Silverhorn Jewelers (Santa Barbara, California) brought the Dreher carvings to our attention in 2009, and we thank him. We are grateful to Leslie Hindman Auctioneers (Denver) for allowing us to photograph a major collection of Dreher carvings prior to their sale. Gem and mineral dealer Bill Larson and his sons, Carl and William, all of Pala International (Fallbrook, California), introduced us to the Dreher family. We thank them for accommodating our ongoing requests to photograph their growing collection of Dreher carvings.

REFERENCES

Adams T. (1988) Fabergé's use of oriental motifs. M.A. thesis, San Diego State University. https://archive.org/details/FabergesUseOfOrientalMotifs

Ball S.H. (1931) Historical notes on gem mining. *Economic Geology*, Vol. 26, No. 7, pp. 681–738, http://dx.doi.org/10.2113/gsecongeo.26.7.681

Collini C.A. (1776) *Journal d'un voyage qui contient differentes observations mineralogiques: particulierement sur les agates, et le basalt. Avec un détail sur la maniere de travailler les agates*. C.F. Schwan, Mannheim, Germany [in French].

Dreher E. (1979) Einer Schleiferfamilie mit Tradition uber drei Jahrhunderte. In K. Schultheiss, Ed., *Heimatkalender des Landkreises Birkenfeld*. Gemeinsam Verlegt von Arbogast, Otterbach, und Klebes, Baumholder, Germany, pp. 139–144.

Dreher G. (2012) Die Gestaltung von Tierfiguren aus Schmuckstein im Raum Idar-Oberstein nach 1950. In *Gravierte Kostbarkeiten = Reznyye Sokrovishcha = Carved Treasures: Precious Stone Carvings from St. Petersburg and Idar-Oberstein at the German Gemstone Museum*. Stiftung Deutsches Edelsteinmuseum, Idar-Oberstein, Germany.

Faber T. (2008) *Fabergé's Eggs: The Extraordinary Story of the Masterpieces that Outlived an Empire*. Random House, New York.

Frazier S. (1978) The gem cutting industry of Idar-Oberstein Part II: Origins. *ULW [United Lapidary Wholesalers] Show News*, Vol. 2, No. 3, pp. 6–27.

Gabriel G. (2015) Lapidary centers of modern Russia. International Fabergé Museum Conference, Fabergé Museum, St. Petersburg.

——— (2017) Homage. In W. Lindemann, W. Larson, and E. Schneider, *Dreher Carvings: Gemstone Animals from Idar-Oberstein*. Arnoldsche Art Publishers, Stuttgart, Germany, pp. 230–231.

Gerdt O. (2017) Idar-Oberstein – A gemstone of Europe. In W. Lindemann, W. Larson, and E. Schneider, *Dreher Carvings: Five Generations of Gemstone Animals from Idar-Oberstein*. Arnoldsche Art Publishers, Stuttgart, Germany, pp. 8–13.

von Habsburg G. (1988) *Fabergé*. Habsburg, Feldman Editions, Geneva.

Hadley W. (1984) A new look at Idar-Oberstein. *Rock & Gem*, Vol. 14, No. 10, pp. 48–51.

Lindemann W. (2017) Gerd and Patrick Dreher - The art of stonecutting today. In W. Lindemann, W. Larson, and E. Schneider, *Dreher Carvings: Gemstone Animals from Idar-Oberstein*. Arnoldsche Art Publishers, Stuttgart, Germany, pp. 14–23.

Ovchinnikov M. (2017) The Dreher family cultural code. In W. Lindemann, W. Larson, and E. Schneider, *Dreher Carvings: Gemstone Animals from Idar-Oberstein*. Arnoldsche Art Publishers, Stuttgart, Germany, pp. 34–41.

Pauly H.U. (2012) Hans-Ulrich Pauly. In *Gravierte Kostbarkeiten = Reznyye Sokrovishcha = Carved Treasures: Precious Stone Carvings from St. Petersburg and Idar-Oberstein at the German Gemstone Museum*. Stiftung Deutsches Edelsteinmuseum, Idar-Oberstein.

Rapp G. (2002) *Archaeomineralogy*. Springer-Verlag, Berlin.

Snowman A.K. (1962) *The Art of Carl Fabergé*. Faber & Faber, London.

Where agates come from (1882) *Scientific American*, June 3, p. 352.

Wild K.E. (1981) Ueber die nachbildung Fabergésche Figuren in Idar-Oberstein. *Goldschmiede-Zeitung*, No. 2, pp. 108–109.

More on Dreher Carvings

Interviews and photo galleries capture the lifelike detail and painstaking process followed by Gerd and Patrick Dreher. Visit www.gia.edu/gems-gemology/winter-2017-gem-virtuosos or scan the QR code to the right.

AKOYA CULTURED PEARL FARMING IN EASTERN AUSTRALIA

Laura M. Otter, Oluwatoosin B. A. Agbaje, Le Thi-Thu Huong, Tobias Häger, and Dorrit E. Jacob

Akoya cultured pearls have been produced on the eastern shoreline of Australia since approximately 1999 using *Pinctada imbricata fucata* mollusks native to New South Wales. Unlike many of their Japanese counterparts, Australian akoya cultured pearls are harvested after 18 months of growth and marketed without any post-harvest treatments involving dyes or bleaches. This study presents the first gemological and mineralogical characterization of Australian akoya cultured pearls using Raman, photoluminescence, FTIR, and UV-Vis specular reflectance spectroscopy. Raman and FTIR spectroscopy identified the major mineral phase aragonite as well as some organic compounds. While Raman spectroscopy revealed polyene-related pigments with bands occurring at 1134 and 1532 cm^{-1}, FTIR spectroscopy showed sulfate- and polysaccharide-associated groups occurring at around 1200 and 1115 cm^{-1}, respectively. UV-Vis spectroscopy revealed broad spectral features that provide insight into the distinct bodycolors and enable discrimination from some non-akoya saltwater cultured pearls from *P. margaritifera*, *P. maxima*, and *P. mazatlanica* bivalves, while separation from other untreated akoya pearls is not possible. Production processes are examined to better understand the modern, sustainable, and environmentally friendly pearl farming operations in Australia.

The *Pinctada imbricata fucata* mollusk has long been used to produce akoya cultured pearls, dating back to the pioneering work in the early 1900s by Japanese entrepreneur Kokichi Mikimoto (Strack, 2006). This bivalve is distributed widely across Asia and also occurs on the eastern coast of Australia (Gifford et al., 2004), where it is used to produce untreated and sometimes vibrantly colored cultured pearls (figure 1). With *Pinctada imbricata fucata* populations readily available on New South Wales's Central Coast region between Sydney and the city of Lake Macquarie, a local enterprise called Broken Bay Pearls with expertise in farming of edible Sydney rock oysters (*Saccostrea glomerata*) has been culturing akoya pearls since 2003 (figure 2). The climate in New South Wales is ideally suited for pearl culturing using *Pinctada imbricata fucata*. It is located approximately the same distance from the equator as the southern Japanese pearl farms, and its very similar seasonal variations of water temperature optimize nacre quality during the cultivation process (Strack, 2006; Gilbert et al., 2017).

Australia was originally known for its large-scale production of silver- and gold-colored natural and cultured South Sea pearls from *Pinctada maxima* (Scarratt et al., 2012 and references therein), which are valued for their large sizes of up to 20 mm in di-

Figure 1. A bracelet showing naturally colored blue, cream, yellow, and silver akoya cultured pearls from Broken Bay Pearls. Photo courtesy of Broken Bay Pearls Pty Ltd.

See end of article for About the Authors and Acknowledgments.
GEMS & GEMOLOGY, Vol. 53, No. 4, pp. 423–437,
http://dx.doi.org/10.5741/GEMS.53.4.423

Figure 2. The map of Australia (A) indicates the location of the Broken Bay Pearls farm near Woy Woy in New South Wales, on the southeastern shoreline (B). The akoya pearl farming operation near Woy Woy (C) and some of the long-line systems for juvenile Pinctada imbricata fucata *that are held nearby (D). For scale, the wooden jetty shown in C and D is 1.5 meters wide. Photos by Laura Otter.*

ameter (Strack, 2006). Australian akoya cultured pearls have yet to receive comparable attention in the gemological community. This study aims to characterize the occurrence of akoya cultured pearls in eastern Australia and presents what is believed to be the first thorough gemological and mineralogical characterization through Raman, photoluminescence (PL), ultraviolet-visible (UV-Vis), and Fourier-transform infrared (FTIR) spectroscopic analysis.

Hatchery and Spat Production. For about a decade, the hatchery facilities located at NSW Fisheries, Port Stephens Fisheries Institute (PSFI) have supplied Broken Bay Pearls with young *Pinctada imbricata fucata*. Broodstock are collected from both the farm and in the wild and selected based on nacre color and shell shape. Priority is given to stock with more convex shells, which allow for larger nuclei to be implanted during seeding. These parents are brought to the hatchery, where spawning is induced by increasing water temperatures by about 4°C. Eggs and sperm are mixed in 1,000-liter tanks. They are kept at 24–26°C until they develop into larvae (figures 3A and 3B) after 20–24 hours; water temperature, feeding protocols, and stock density are regulated as needed (O'Connor et al., 2003). The larval cycle takes approximately three weeks before they are ready to settle from the water column and attach to a substrate such as mesh screens or bags.

After settlement, these spat are retained until reaching approximately 1.5 mm in size, whereupon they are transferred from the hatchery in Port

Stephens to the pearl farm near Woy Woy (figure 2). Here, they are placed in 0.5 mm mesh bags (figure 3C) attached to several parallel long-line systems about 200 meters in length and situated at a depth of 4 meters below the low tide water level. As the juvenile *Pinctada imbricata fucata* bivalves grow, they are progressively transferred to larger mesh bags or cages that are cleaned regularly to ensure good water flow.

Broken Bay Pearls is currently the only akoya pearl farm on the New South Wales coastline. Several small islands act as a barrier between the open ocean and the farm, creating a well-protected bay that is ideally suited for pearl farming. This area within the estuary provides stable salinity, nutrient availability, and high levels of dissolved oxygen, which are key factors for the long-term development and cultivation of a healthy stock.

Seeding and Maintaining of Australian Akoya Pearl Oysters. The juvenile pearl oysters are maintained on the farm until they are approximately two years old with shell heights of about 7 cm. Similar to other farms, the mollusks are cleaned with high-pressure cleaners every two to four weeks (Gifford et al., 2004).

It is common practice to condition the pearl oysters for several weeks before seeding by reducing their physiological fitness. At Broken Bay this is achieved by stocking the mollusks at high density within barnacle-overgrown wicker baskets that restrict water flow and food availability. Other farms, such as those in Southeast Asia, cover the mollusks with fabric to achieve the same effect (Hänni, 2007). Either way, they respond to food shortage by ceasing gamete production that would otherwise interfere with the seeding process (Hänni, 2007). This conditioning strategy allows the seeders at Broken Bay Pearls to process the animals without having to apply relaxant drugs to immobilize them (Acosta-Salmón et al., 2005).

The bivalves are seeded in the austral summer month of February using only shells of suitable size (shell height larger than 7 cm) and fitness. This ensures acceptance of the bead, fast recovery from surgery, and a greater chance for successful pearl growth. The production of cultured pearls requires two types of mollusk broodstock. Donor mollusks are selected for nacre color and quality and are sacrificed in the seeding process to extract the mantle tissue graft that is later inserted with the bead. The host animals, on

In Brief

- Gem-quality akoya bead cultured pearls have been produced on Australia's eastern shoreline since 1999, with environmentally friendly strategies to achieve sustainable farming.
- A wide variety of colors occur naturally besides the traditional white and silver. These cultured pearls are marketed without the application of bleaches or dyes.
- Australian retailers have embraced these akoya cultured pearls as locally manufactured jewelry becomes increasingly popular in the country.
- This work suggests that colored akoya cultured pearls produced by *P. imbricata fucata* can be differentiated from pearls from other species such as *P. margaritifera*, *P. maxima*, and *P. mazatlanica* using UV-Vis spectroscopy.

Figure 3. Australian Pinctada imbricata fucata *larvae, shown here at an age of about 25 hours (A) with approximately 200 µm shell size, are reared in 1,000-liter polyethylene tanks at the nursery (B). After 24 days, the larvae mature to spat with approximately 1.5 mm shell lengths. They are transferred to long-line systems and kept in 0.5 mm nylon mesh bags (C). Photos by Wayne A. O'Connor.*

*Figure 4. These photos show the steps involved in the seeding of Australian akoya pearls. A: The outermost part of the mantle lobe is cut from a donor mollusk. B: The outer epithelial tissue is separated from the darker marginal mantle part using a scalpel. C: The outer epithelial tissue is cut into small, approximately 2 × 2 mm tissue grafts (*saibo*). D: An incision is carefully made in the gonad, while the bivalve is affixed to an oyster stand. E: The 6 mm beads are manufactured from American freshwater mussel shells. F: Tissue and bead are inserted into the gonad. Photos by Laura Otter.*

the other hand, are selected for fitness and health to enable optimal proliferation of the tissue graft into a nacre-producing pearl sac (Hänni, 2012). The two Australian seeders at Broken Bay Pearls were trained by Japanese specialists who also visit regularly during harvests. Each year they insert several thousand beads—exact numbers remain confidential—together with tissue grafts. Two beads are inserted per mollusk.

Tissue grafts are prepared following the Japanese method. First, the outermost part of the mantle lobe is removed from the donor (figure 4A) and the outer epithelial tissue is carefully separated from the darker marginal mantle tissue (figure 4B). Then the outer epithelial tissue is cut into approximately 2 × 2 mm pieces, known as the *saibo* or graft (figure 4C). The gonad in the donor mollusk is opened (figure 4D), and each tissue graft is carefully inserted into the mollusk together with a 6 mm bead manufactured from American freshwater mussel shells (figure 4E). Graft and bead are carefully placed in contact with each other (figure 4F). Since the gonad tissue itself is unable to produce pearls, the bead must be accompanied by the mantle tissue graft. Following the seeding process, the graft proliferates to form a pearl sac, fully enclosing the bead (Hänni, 2012) and pro-

TABLE 1. Characteristics of natural-color cultured pearls from *Pinctada imbricata fucata* bivalves from eastern Australia.

Photo[a]	Sample no.	Diameter (mm)	Weight (ct)	Bodycolor[b]	Hue[b]	Overtone[b]
	BBP01	7.3	3.01	Light yellow	Green	Yellow
	BBP02	6.7	2.20	Light yellow	Orange	Gold
	BBP03	7.0	2.51	Dark yellow	Orange	Green
	BBP04	6.9	2.48	Dark yellow	Orange	Gold, orange
	BBP05	6.9	2.50	Orange	Brown	Pink
	BBP06	7.5	3.03	Pinkish orange	Green	Pink
	BBP07	7.4	2.90	Silver	Blue	Blue, pink
	BBP08	6.8	2.31	White	Silver	Pink
	BBP09	7.2	2.66	White	Cream	Pink
	BBP10	7.0	2.49	Silver	Green	Blue
	BBP13	7.9	3.56	Green	Silver	Pink
	BBP14	7.7 × 8.2	3.65	Green	Silver	Blue
	BBP11[c]	6.7	2.00	Dark blue	Green	Silver, blue
	BBP12	7.2	2.48	Silver (darker than BBP07 and BBP10)	Green	Blue, pink

[a]*Images not to scale. Bead sizes are 6 mm for all specimens shown.*
[b]*Bodycolor, hue, and overtone were determined by visual examination. Bodycolor descriptions follow the GIA scheme (https://www.gia.edu/pearl-description), but extending the scheme was necessary to incorporate the large range of color in these samples.*
[c]*Color was found to vary from blue on one side to silver with only a blue hue and overtone on the other. All spectroscopic measurements were taken from the blue side.*

ducing calcium carbonate, causing the deposition of nacre onto the bead (Jacob et al., 2011). Hence, the relative position between tissue graft and bead as well as the position within the pearl sac determine the eventual shape of the pearl: In the ideal case, when tissue graft and bead are in tight contact, a round pearl is formed. Near-round, semi-baroque, or baroque pearls are formed by an irregular contact between bead and graft that results in cavities or even loose beads (Hänni, 2012; Otter et al., 2014).

Harvesting and General Farming Procedures of Australian Akoya Cultured Pearls. After seeding, the *Pinctada* bivalves are returned to the long-line systems in bags or cages, where their food supply is no longer restricted. Their metabolic activity increases, and the production of nacre needed for shell growth and pearl development returns to normal. Hence, the bulk of pearl growth occurs during the austral summer months (December to February), when the animals have an increased metabolism and food is abundant. In contrast, a finer and therefore more lustrous outermost layer of nacre is deposited in austral winter (June to August), when colder temperatures slow down metabolic and biomineralizing processes (Gilbert et al., 2017).

Bead rejection rates are approximately 10%, which is relatively low compared to farms in the Federated States of Micronesia (28%) or southwest India (14%), while recent rejection rates from Japan were not available in the literature (Kripa et al., 2007 and references therein; Cartier et al., 2012). Broken Bay Pearls generally allows a longer cultivation time of 18 months to achieve a thicker nacre, compared to the standard 6–12 months in Japan (Strack, 2006). The longer cultivation time results in a nacre layer around the bead measuring approximately 0.8 mm, estimated from pearls used in this study (see bead sizes and diameter measurements in table 1) as well as verification measurements on a cross section of a low-quality pearl.

Figure 5. The steps involved in the process of harvesting Australian akoya pearls. A: Bivalves are removed from their cages. B: The separator cleans the pearls from the tissues. C: Separated pearls are collected by opening a valve at the bottom of the machine. D: Wooden revolving drums are used to wash the pearls in a saltwater solution. E: A selection of the day's harvest with the range of colors displayed at the front. Photos by Laura Otter.

This is high compared to Japanese akoya, whose nacre thickness averages only 0.2 mm in the northern islands and rarely exceeds 0.3 mm in the warmer waters of the southern islands (Strack, 2006).

The pearls are harvested in the austral winter months of June and July. Following the Japanese akoya culturing tradition, pearl oysters at Broken Bay Pearls are generally not seeded a second time but are

removed from their cages (figure 5A) and sacrificed by cutting through the adductor muscle. A motorized separator (figure 5B) reduces the soft tissues to small pieces while the relatively heavy pearls collect at the bottom of the machine and are extracted by opening a valve (figure 5C). Adhesive organic remains are removed by using a suspension of salt in freshwater (figure 5D), while walnut shells are used to buff the pearls, a common practice in Japan. The pearls are spread out on cloth for air drying in sunlight (figure 5E), which could be understood as a minimal *maeshori*[1] luster enhancement, depending on how strictly this is defined. However, it is emphasized here that no color- or luster-improving substances or processes are otherwise applied—e.g., dyes, bleaches, or alcohol, which are traditionally used for Japanese akoya (Gervis and Sims, 1992). After drying, the pearls are graded for quality, color, luster, shape, and size.

Figure 6. This silver pendant features a round 7.5 mm silver akoya pearl from Broken Bay. The silver disk is etched with a pattern resembling the reflection of the moon on the rippling ocean. Photo courtesy of AngelRock Jewellers.

Figure 7. Naturally white cultured pearls from Broken Bay: two necklaces, a pair of stud earrings, and three loose pearls. Photo courtesy of Percy Marks Jewellers.

The farm in Broken Bay produces several thousand pearls per year, and about 50% are of gem quality. The average size ranges from 6.5 to 8 mm and in very rare cases up to 10 mm. Keshi pearls also occur as a result of the seeding process, as the fragile epithelial cells of the mantle tissue can be injured or separated and develop into small pearl sacs that produce an additional though unintended small pearl (Hänni, 2006). Broken Bay pearls are cultured in a wide range of colors. Bodycolors include the traditional akoya silver and white (figures 6 and 7, respectively), though light and dark yellows appear almost as frequently and blues are also occasionally seen (again, see figure 1). Intense orange bodycolors (as in BBP05 and BBP06, table 1) occur very rarely. Overtones range from orange, pink, silver, white, silver-green, and cream through yellow to gold.

The two seeders at Broken Bay have noticed a difference in the respective proportions of silver to white, yellow, and blue bodycolors they produced (figure 8). After tracing back and comparing their in-

[1]*Maeshori* treatment aims to enhance a pearl's luster. This can involve different chemical (e.g., alcohol or salty solutions) or physical (e.g., heating and cooling) treatments. It is traditionally applied to Japanese akoya cultured pearls, often in combination with dyes or bleaches.

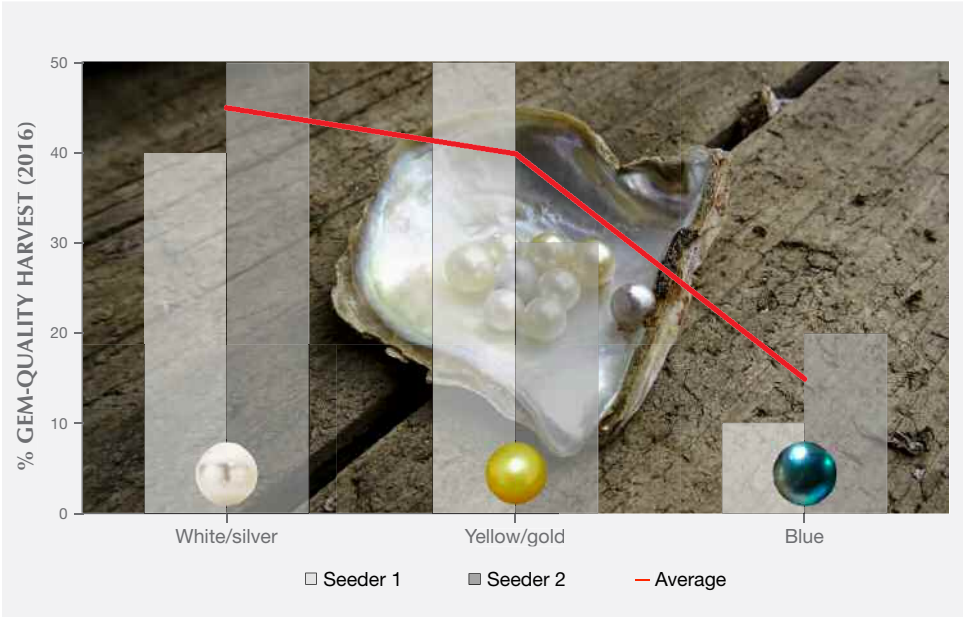

Figure 8. Broken Bay's two seeders tag their own cages of freshly seeded bivalves to track the proportions of bodycolors produced. The proportion of white, yellow, and blue bodycolors is seen to vary between the seeders, and this is attributed to slight variations in the selection of appropriate tissue graft. The red line shows the overall abundance of each bodycolor as an average of both seeders. Photo by Laura Otter.

dividually seeded bivalves, which had been color coded on their cages, the seeders concluded that while cutting and preparing the tissue grafts, they each favored slightly different colored tissue pieces, thus influencing the harvested colors.

It is understood that modern pearl farming yields many positive consequences for the local ecosystem. The exceptionally high filtering capabilities of the *Pinctada* species, up to 25 liters per gram of dried tissue each day, effectively remove heavy metals, organic pollutants, and nutrient overloads from coastal environments (Gifford et al., 2004). Hence, pearl farming reduces turbidity and eutrophication—i.e., the excess supply of nutrients coupled with high biomass loads. Turbidity is reduced by the long-line systems, with their many large cages that act as a barrier for near-surface currents. Eutrophication is reduced by the high filter-feeding capacities of the bivalves. Furthermore, the timber-free long-line systems prevent entanglement of dolphins and other marine species. Following these environmentally friendly principles, Broken Bay Pearls has been successful in supplying a wide range of Australian wholesalers and jewelers each year.

MATERIALS AND METHODS

The lead author attended Broken Bay's annual pearl harvest in June 2016 to obtain pearls for this study. The mollusks were brought to the farm by boat and taken from the nets and opened by hand. After extraction from the separator, the pearls were spread out on a cloth and examined. The author visually determined a wide range of bodycolors, including yellow, silver, white, cream, orange, blue, and light silver-green of various shades and intensities (again, see figure 5E). A total of 14 saltwater cultured pearls were selected as representative of each bodycolor group for the present study. The pearls were found to be mostly round (samples BBP01 to BBP13) to semi-round (BBP14) in shape. They measured 6.7–8.2 mm in diameter with an average of 7.2 mm, while their weight varied from 2.0 to 3.7 ct (table 1).

Raman spectra of each pearl were collected at room temperature using a Horiba Jobin Yvon LabRAM HR Evolution confocal spectrometer with 473 nm laser excitation. All Raman spectra were recorded in the 100–2000 cm^{-1} range using a spectral acquisition time of 12 seconds and four accumulations. A grating with 1800 grooves/mm was used with a slit width of 100 µm to ensure a high spectral resolution of approximately 0.8 cm^{-1}. PL spectra were collected using the same instrument, although measurement conditions were adjusted to a spectral acquisition time of eight seconds and five accumulations per cycle, with 532 nm excitation wavelength. Data were collected in the 537–710 nm range using a grating with 600 grooves/mm to achieve higher intensities at a spectral resolution of approximately 2 cm^{-1}.

Mid-FTIR spectra were recorded with a Thermo Scientific Nicolet iN10 infrared microscope using a 149 × 149 µm aperture and an acquisition time of five seconds per spectrum. All data were collected with 16 scans per spectrum in the range of 675–3970 cm^{-1} using a liquid-nitrogen-cooled MCT-A detector sys-

tem and a spectral resolution of 4 cm^{-1}. A background spectrum was collected in air before each sample spectrum. Raman, PL, and FTIR data were collected at Macquarie University's Department of Earth and Planetary Sciences in Sydney.

UV-Vis spectra were recorded 16 times per sample in the 380–800 nm range using a Leica Orthoplan microscope in combination with a Leica MPV-SP UV-Vis spectrophotometer at Johannes Gutenberg University in Mainz, Germany. Microscope-based UV-Vis data acquisition is generally performed without the use of an integrated sphere accessory, which made it necessary to collect all spectra in specular reflection mode with well-defined incident and reflected light angles (2° in this study). Specular reflection mode uses a thin plate of polished aluminum as reference material, since it has higher reflectance properties than $BaSO_4$ or Spectralon, which are only used when data collection is performed in diffuse reflection mode. All spectra were collected using 32× magnification by focusing on the surface of each pearl. Some individual samples (namely BBP05, BBP07, BBP11, and BBP12) yielded reflectance values greater than 100%, which made it necessary to focus slightly subsurface.

RESULTS AND DISCUSSION

Raman Spectrometry. Figure 9 presents seven representative Raman spectra of Australian akoya cultured pearls across the range of bodycolors as outlined in table 1 (yellow, orange, silver, white, green, and blue). The most prominent peaks are assigned to aragonite (black lines), the crystalline calcium carbonate polymorph generally associated with lustrous pearls of the *Pteriida*e family (e.g., Jacob et al., 2011; Wehrmeister et al., 2011; Hänni, 2012). Among these, the highest-intensity band was observed at 1085 cm^{-1}, as well as a doublet with peak centers at 701 and 705 cm^{-1}, which are assigned to ν_1 (symmetric stretching) and ν_4 (in-plane bending) modes of the carbonate anion (CO_3^{2-}) in aragonite (e.g., Urmos et al., 1991). The small peak at 1462 cm^{-1} is identified as ν_3 (in-plane asymmetric stretching); due to its low intensity, this peak is not observed equally well in all pearls. In addition, aragonite lattice modes were observed between 170 and 300 cm^{-1} (Urmos et al., 1991). All pearls showed virtually identical peak centers, intensities, and backgrounds except for the darkest one (BBP11), which had a slightly increased background (again, see figure 9). This is due to a stronger contribution of luminescence in the background signal, pos-

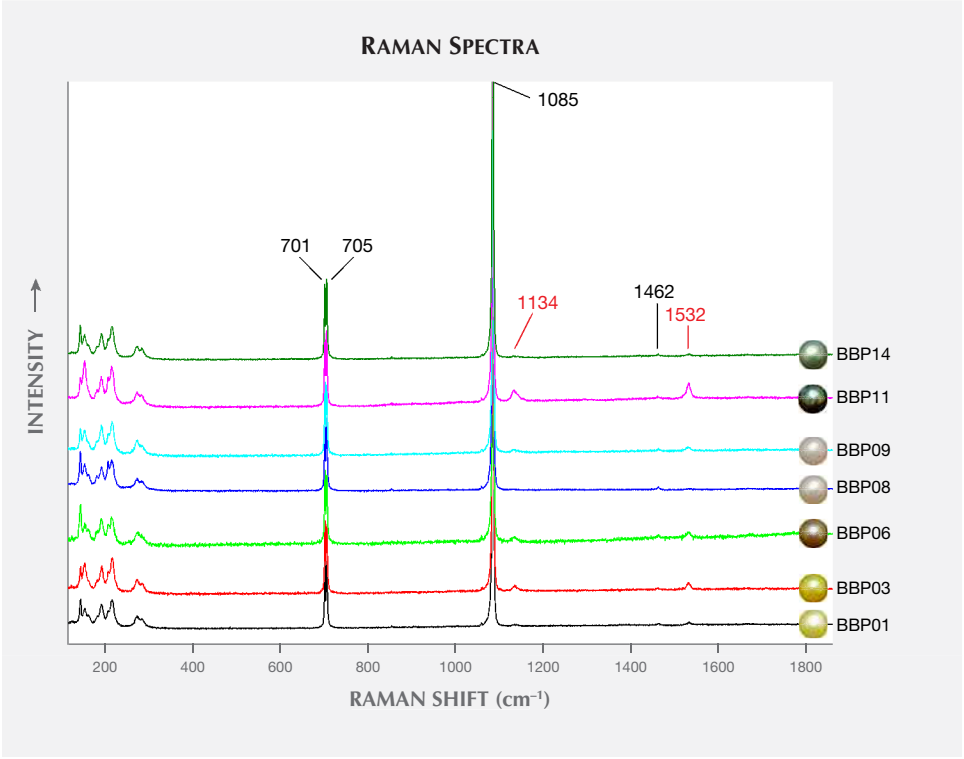

Figure 9. Raman spectra of seven Broken Bay akoya cultured pearls from Pinctada imbricata fucata *normalized to the highest-intensity peak at 1085 cm^{-1} and offset for clarity. The selection shows a cross section of bodycolors ranging from light yellow (BBP01, BBP03), orange (BBP06), white (BBP08), silver (BBP09), and dark blue (BBP11) to green (BBP14). The spectra show identical bands for aragonite (black lines), while two remaining peaks are attributed to pigments (red lines).*

sibly related to pigments contributing to the pearl's dark blue color.

Peaks of weaker intensity (figure 9, red lines) corresponded to distinct bands of pigments (polyenes) consistent with previously published values (e.g., Karampelas et al., 2007; Soldati et al., 2008; Karampelas et al., 2009; Bersani and Lottici, 2010). These include peaks at 1134 and 1532 cm^{-1} that belong to the stretching modes of the C-C single bond (ν_2) and C=C double bond (ν_1) in the polyene chain biomolecule, respectively. Samples with darker bodycolors such as dark blue (BBP11), orange (BBP06), and dark yellow (BBP03) displayed the highest intensities for both pigment-related peaks, while green (BBP14), white (BBP09), and light yellow and yellow (BBP01) pearls exhibited much lower intensities. For the white specimen BBP08, the peaks were undetectable.

Photoluminescence Spectrometry. All PL spectra showed virtually identical features in the yellow to red region at 585, 610, 625, and 685 nm (figure 10). Sharp peaks in the spectra resulted from the Raman effect and occurred independently of the PL bands. These included features in the 538–540 nm region (vibrational properties of the aragonite lattice modes), as well as discrete peaks, caused by vibrational modes of the carbonate ion, at 552 nm (in-plane bending, ν_4), 565 nm (symmetric stretching, ν_1), 577 nm (in-plane asymmetric stretching, ν_3), and 630 nm (caused by $\nu_1 + \nu_3$; Xu and Poduska, 2014). The four PL bands had positions similar to those previously published for cultured pearls from *Pinctada maxima*, *Pinctada margaritifera*, *Pinctada mazatlanica*, and *Pteria sterna*, at 620, 650, and 680 nm; however, the weak band at 585 nm has not been described for these species (Miyoshi et al., 1987; Kiefert et al., 2004; Karampelas et al., 2011; Karampelas, 2012). It should be noted that all bands appear less defined for the akoya pearls than for those produced by *Pinctada maxima*, *Pinctada margaritifera*, and *Pteria sterna*. PL features in pearls are generally thought to result from organic compounds within the nacre composite material (Karampelas et al., 2007). This is consistent with our observation that the relative PL intensity correlated with color intensity in the specimens and stronger pigment-related Raman bands (figure 9).

Mid-FTIR Spectrometry. The most prominent features observed in the spectra of cultured pearls from Australian *Pinctada imbricata fucata* were caused by the

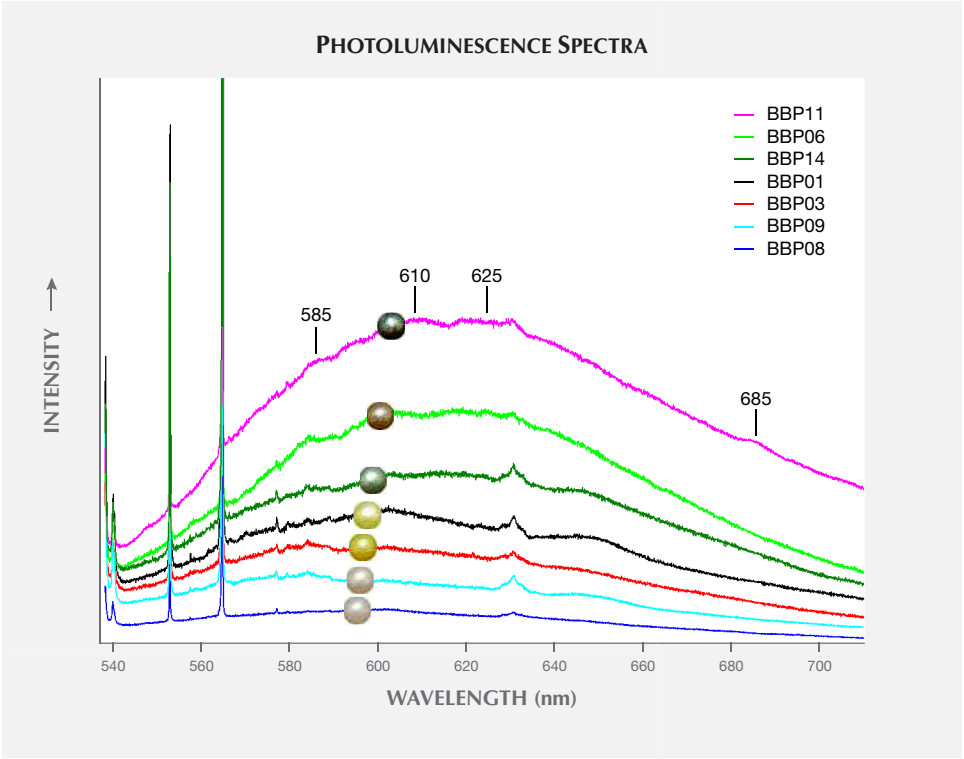

Figure 10. Uncorrected photoluminescence (PL) spectra of the seven akoya cultured pearls whose Raman spectra are shown in figure 9. Spectra are offset for clarity while maintaining their original order of relative PL intensities. All spectra show identical features at 585, 610, 625, and 685 nm, with varying amounts of luminescence that correlate with the color intensity of the samples. Peaks in the 538–540 nm region as well as at 552, 565, 577, and 630 nm originate from the Raman effect of aragonite.

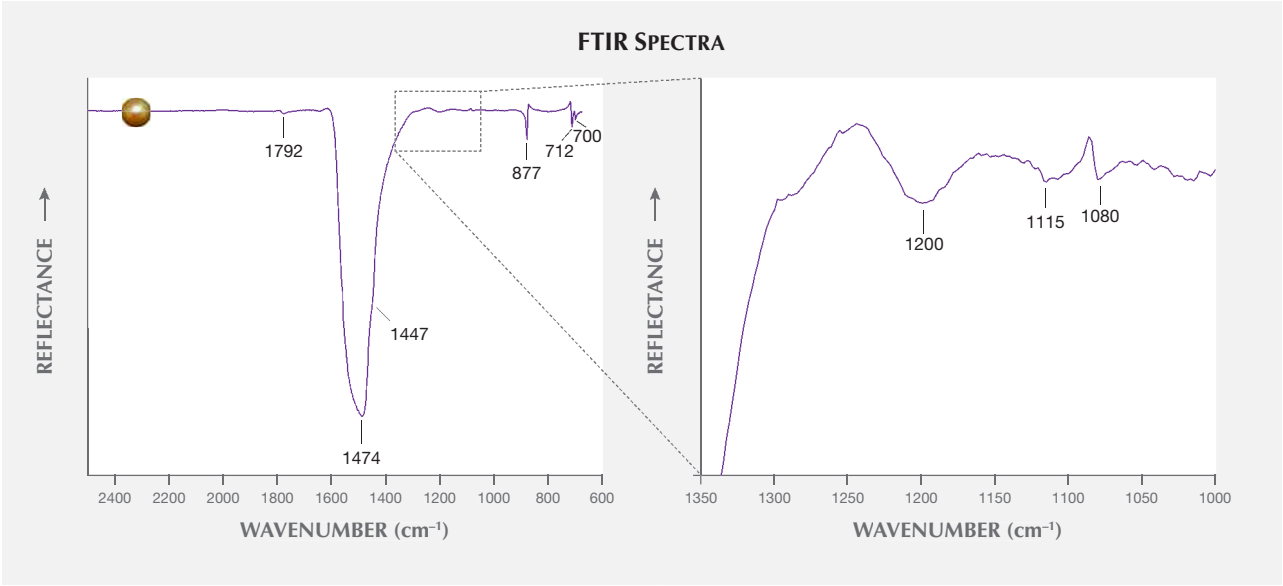

Figure 11. Left: The mid-FTIR spectrum of an orange sample from Broken Bay Pearls (BBP05) shows bands at 700, 712, 877, 1447, 1474, and 1792 cm^{-1} that are characteristic for aragonite and were found in all other samples. However, this sample also shows several weak peaks in the 1000–1350 cm^{-1} region (red box in A). Right: Enlargement of this region reveals several small peaks at around 1200 and 1115 cm^{-1} that are assigned to sulfate and polysaccharide groups of the organic component. The weak band at 1080 cm^{-1} results from stretching vibrations of the carbonate.

intrinsic vibrational modes of the aragonite crystal lattice (figure 11, left), namely ν_{4b} and ν_{4a} at 700 and 712 cm^{-1} (internal modes), ν_2 at 877 cm^{-1} (out-of-plane bending mode), and ν_3 at 1447 cm^{-1} (in-plane asymmetric stretching). Strong absorption bands in the 1600–1400 cm^{-1} range resulted from several closely spaced peaks at 1570, 1525, 1488, 1474, and 1440 cm^{-1} (Andersen and Brecevic, 1991; Xu and Poduska, 2014). The highest-intensity band at 1474 cm^{-1} was previously found to result from a combination of the lattice mode peaks at 220, 263, 290, and 700 cm^{-1} (Andersen and Brecevic, 1991; Xu and Poduska, 2014). A weak band at 1792 cm^{-1} was caused by a combination of the ν_1 and ν_{4a} modes, while ν_1 (symmetric stretching vibration) was observed in figure 11, right (an enlargement of the red box in figure 11, left). Three other bands in figure 11 (right) can be attributed to different organic compounds in nacre: Broad bands at around 1200 and 1115 cm^{-1} likely resulted from S-O of sulfate and C-O of polysaccharide groups, respectively (Marxen et al., 1998). The peak at 1080 cm^{-1} is assigned to the symmetric stretching vibration (ν_1) of CO_3^{2-}.

UV-Vis Spectrometry. The pearls were grouped into different UV-Vis spectra with similar characteristics. For better readability, overlapping spectra were offset by adding or subtracting each measured intensity value with a fixed offset value expressed as a percentage relative to the original measured intensity (figure 12). The specimens shown in figure 12A consist of two pearls of a rather cooler shade of yellow, which might result from green hues and/or overtones (BBP01 and BBP03), plus silver (BBP10) and green (BBP14) samples. They are characterized by a slight spectral trough in the blue-green to yellow region between 450 and 600 nm (except for BBP01) and have a sharp drop in relative intensity from approximately 645 nm onward. The light yellow specimen BBP01 (table 1) has the brightest bodycolor, which correlates with the highest relative intensity. Of the two pearls in figure 12B, one has a light silver bodycolor with a blue hue and overtone (BBP07) and the other a dark blue (BBP11) bodycolor with green, blue, and silver hues and overtones (hues and overtones determined by visual observation). The spectrum of the dark blue pearl (BBP11) shows two distinct troughs at 425–530 nm (blue to green region) and 550–625 nm (green to orange region), while the silver specimen (BBP07) has a trough at 425–625 nm. Both pearls display a sharp drop in reflectance at 625 nm. A lower intensity over the full spectral range is responsible for the dark color of BBP11; specimen BBP07 shows a similar pattern, but at an overall higher relative intensity that corresponds to its brighter color. Figure 12C shows spectra

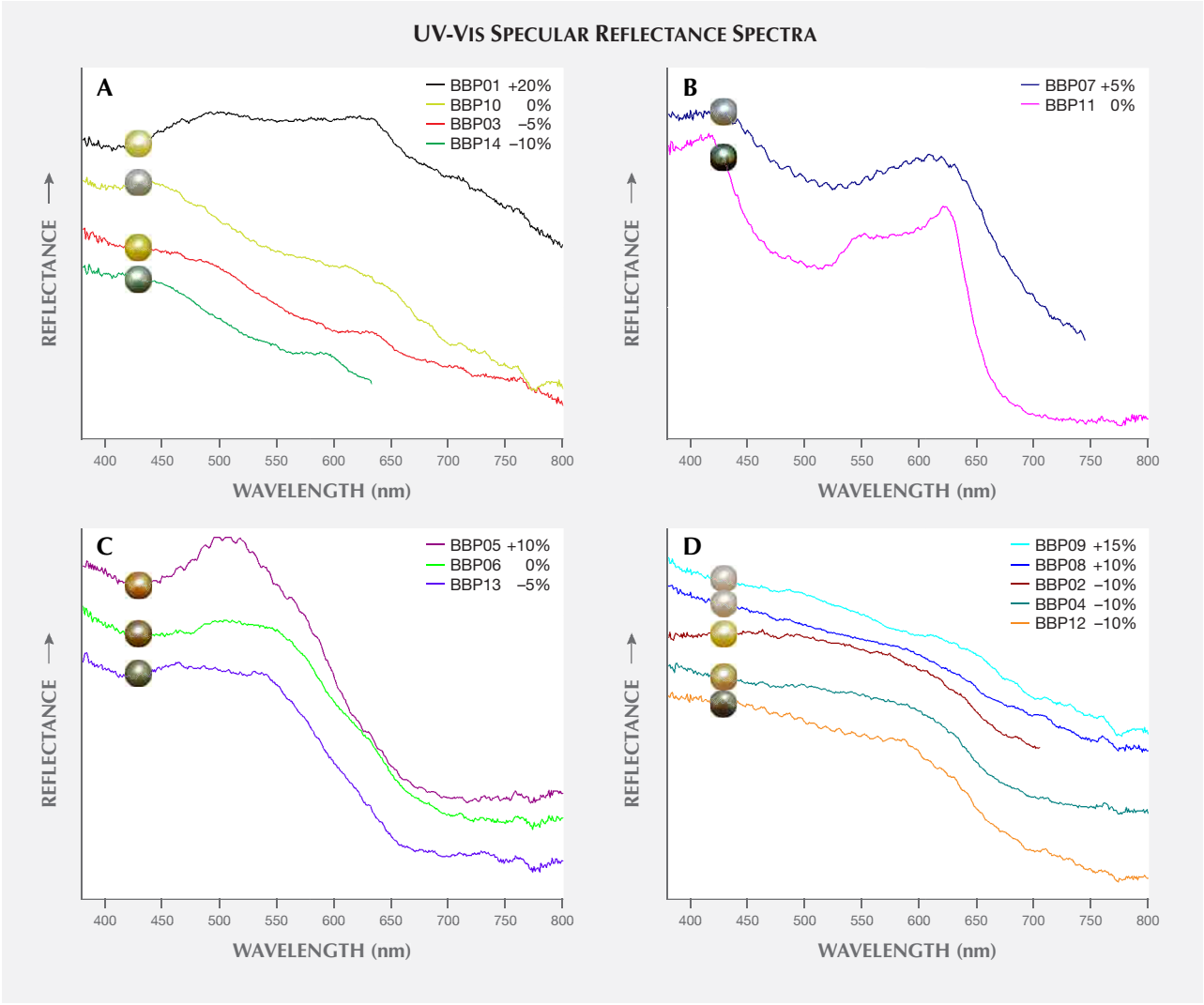

Figure 12. UV-Vis specular reflectance spectra of 14 Australian akoya samples normalized to the reflectance yield of a polished aluminum plate. Some spectra are offset for clarity, with offset values provided in the legends.

for the pearls with orange bodycolor (BBP05 and BBP06) as well as for a green specimen with warm pink and silver hues and overtones (BBP13). These specimens exhibit distinct absorption features between 400 and 475 nm and between 600 and 800 nm that correspond to the blue region and the orange to red region, respectively. At 800 nm, relative intensities drop to below 55%. Lastly, figure 12D shows spectra for pearls that exhibit white (BBP08 and BBP09), dark silver (BBP12), and yellow bodycolors (BBP02 and BBP04). Note that the pearls with yellow bodycolor from figure 12D have orange and golden hues and overtones, while the other yellow specimens in figure 12A show green and yellow hues and overtones. Their spectra lack distinct absorption features and differ only in relative intensity.

Altogether, each pearl's bodycolor is strongly dependent on its specific absorption features and relative intensities, which are produced by different combinations of pigments present in the organic compound of the nacre (Soldati et al., 2008; Karampelas et al., 2009; Karampelas, 2012). The bodycolor was found to correlate with the overall relative intensity of the PL spectra (figure 10), where the dark blue specimen (BBP11) exhibited the highest relative PL intensity, while the yellow, white, and silver samples had the lowest.

Although the pearls from this study show a wide variety of spectral features, they can be differentiated from untreated pearls of some other species: Gray, yellow, and black pearls from *Pinctada margaritifera* as well as gray, yellow, and green pearls from *Pinc-*

tada mazatlanica show a distinct trough at 700 nm that is not present in any of the akoya pearls from this study. In those pearls, the feature is associated with the presence of pigments (Miyoshi et al., 1987; Elen, 2002; Karampelas et al., 2011; Cartier et al., 2012). Further, dark gray pearls from both *Pinctada margaritifera* and *Pinctada mazatlanica* show an absorption feature at 405 nm that is known to result from uroporphyrin pigments (Homkrajae, 2016, and reference therein). Yellow pearls from *Pinctada maxima* show a broad trough from 310 to 510 nm, with individual absorption features centered at 360 and 430 nm. This distinguishes them from the *Pinctada imbricata fucata* pearls from this study, which also show various absorption features at higher and lower wavelengths (table 2). While discrimination between naturally colored pearls across different saltwater species appears promising, naturally colored white akoya pearls remain indistinguishable from untreated white pearls produced by other mollusks, due to the absence of characteristic spectral features. Also, the discrimination of naturally colored akoya cultured pearls produced in eastern Australia from others of different geographic origin is considered beyond the capability of this method.

CONCLUSIONS

We have presented a description and characterization of akoya cultured pearls from the Central Coast region of New South Wales in eastern Australia. Apart from the absence of bleaching or dyeing procedures, the pearls are cultured following the Japanese tradition. Their natural variety of bodycolors ranges from lighter and darker golden yellows to different shades and intensities of orange and blue to the classic silver and white. These colorful akoya pearls can be used to create modern, nature-inspired jewelry (see figures 1 and 6) as well as classic pieces (figure 7).

Raman and FTIR spectroscopy verified the main mineral phase as aragonite (figures 9 and 11), and pigment-related Raman bands were observed at 1135 and 1530 cm^{-1}. These belong to stretching modes of the C-C single bond and C=C double bond of the polyene chain biomolecules. These peaks were found to have the highest intensities for samples with darker bodycolors, such as dark blue, orange, and yel-

TABLE 2. Summary of color and corresponding absorption centers of untreated cultured pearls from *P. fucata*, *P. margaritifera*, and *P. maxima*.

Mollusk species	Pearl bodycolor	Absorption centers in specific range (nm)				References
		350–450	450–550	550–650	650–800	
P. imbricata fucata	Silver	None	None	~550[a]	775	This study
	Yellow (cool hue and overtone)	None	None	~550[a]	c.a.[b]	
	Yellow (warm hue and overtone)	None	None	None	c.a.	
	White	None	None	None	c.a.	
	Orange	430	None	None	~720[a]	
	Green	~430[a]	None	~550[a]	~720[a]	
	Silver with strong blue overtone	None	513	None	c.a.	
	Dark blue	None	510	580	~750[a]	
P. margaritifera	White and silver	None	None	None	None	Elen (2002)
	Gray	None	460, 495	None	700	Karampelas (2012)
	Yellow	None	None	None	700	Elen (2002)
	Black	405	495	None	700	
P. maxima	Yellow	360, 430	495	None	None	Elen (2002)
	Gray	None	460, 495	None	None	Karampelas (2012)
P. mazatlanica	Dark gray	405	None	None	700	
	Yellow to green	~358[a]	~423[a]	None	700	Homkrajae (2016)
	White and silver	None	None	None	None	

[a]*Approximate peak center due to a very broad or indistinct feature*
[b]*c.a. = continuous absorption*

low (figure 9, red lines). The pearls showed four rather indistinct PL bands in the yellow to red region of the electromagnetic spectrum (figure 10), which were similar to the band positions observed for *Pinctada maxima*, *Pinctada margaritifera*, *Pinctada mazatlanica*, and *Pteria sterna* bivalves (though not as prominent). FTIR spectroscopy of an intense orange pearl revealed the presence of sulfates and polysaccharides representative of organic compounds (figure 11). Lastly, UV-Vis specular reflectance spectroscopy showed several absorption features in the visible range that result from the pearls' different bodycolors, hues, and overtones (figure 12, A–D). This technique was found to be useful in discriminating between diverse colorful akoya pearls from this study and cultured pearls from *Pinctada margaritifera*, *Pinctada mazatlanica*, and *Pinctada maxima* bivalves (table 2), while akoya pearls from other locations as well as white specimens from various species are likely not distinguishable.

ABOUT THE AUTHORS

Ms. Otter (laura.otter@hdr.mq.edu.au) and Mr. Agbaje are PhD candidates at the Macquarie University Department of Earth and Planetary Sciences in Sydney. Dr. Huong is postdoctoral researcher at the Institute of Earth Sciences, Karl Franzens University in Graz, Austria. Dr. Häger is a scientist at the Centre for Gemstone Research at Johannes Gutenberg University in Mainz, Germany, and lectures at the Gemstone and Jewelry Design Department at the University for Applied Sciences in Idar-Oberstein. Dr. Jacob is professor of earth sciences and biomineralization at Macquarie University.

ACKNOWLEDGMENTS

We gratefully acknowledge Ian and Rose Crisp as well as Peter Clift from Broken Bay Pearls Pty Ltd for the opportunity to visit their pearl farm during seeding and harvest season, and for providing all the pearls shown in this study and answering all our questions. Dr. Jennifer Rowland is kindly thanked for skillful editing of the final manuscript. We thank Ursula Wehrmeister, Dilmi Herath, Michael Förster, Christoph Lenz, and Matthew A. Kosnik for many enriching discussions. Dr. Wayne O'Connor, center director for aquaculture at the Port Stephens Fisheries Centre, NSW Department of Primary Industries, is kindly acknowledged for insightful comments on an earlier draft. Furthermore, we thank Celeste Boonaerts from AngelRock Jewellers, Cameron Marks from Percy Marks Jewellers, and Wayne O'Connor for providing photographs. This work is part of the lead author's PhD thesis; she is supported by an Australian Government International Postgraduate Research Scholarship (IPRS). Mr. Agbaje is supported by a Macquarie University Research Excellence Scholarship, and Dr. Jacob is financially supported by the Australian Research Council via a Future Fellowship and a Discovery Grant. Lastly, we thank three anonymous reviewers for providing very constructive and valuable comments.

REFERENCES

Acosta-Salmón H., Martínez-Fernández E., Southgate P.C. (2005) Use of relaxants to obtain saibo tissue from the blacklip pearl oyster (*Pinctada margaritifera*) and the Akoya pearl oyster (*Pinctada fucata*). *Aquaculture*, Vol. 246, No. 1-4, pp. 167–172, http://dx.doi.org/10.1016/j.aquaculture.2004.12.010

Andersen F.A., Brecevic L. (1991) Infrared spectra of amorphous and crystalline calcium carbonate. *Acta Chemica Scandinavica*, Vol. 45, No. 10, pp. 1018–1024, http://dx.doi.org/10.3891/acta.chem.scand.45-1018

Bersani D., Lottici P.P. (2010) Applications of Raman spectroscopy to gemology. *Analytical and Bioanalytical Chemistry*, Vol. 397, No. 7, pp. 2631–2646, https://doi.org/10.1007/s00216-010-3700-1

Cartier L.E., Krzemnicki M.S., Ito M. (2012) Cultured pearl farming and production in the Federated States of Micronesia. *G&G*, Vol. 48, No. 2, pp. 108–122, http://dx.doi.org/10.5741/GEMS.48.2.108

Elen S. (2002) Identification of yellow cultured pearls from the black-lipped oyster *Pinctada margaritifera*. *G&G*, Vol. 38, No. 1, pp. 66–72, http://dx.doi.org/10.5741/GEMS.38.1.66

Gervis M.H., Sims N.A. (1992) *The Biology and Culture of Pearl Oysters (Bivalvia: Pteriidae)*. Overseas Development Administration of the United Kingdom (London) and International Center for Living Aquatic Resources Management (Manila).

Gifford S., Dunstan R.H., O'Connor W., Roberts T., Toia R. (2004) Pearl aquaculture—profitable environmental remediation? *Science of the Total Environment*, Vol. 319, No. 1-3, pp. 27–37, http://dx.doi.org/10.1016/S0048-9697(03)00437-6

Gilbert P.U., Bergmann K.D., Myers C.E., Marcus M.A., DeVol R.T., Sun C.-Y., Blonsky A.Z., Tamre E., Zhao J., Karan E.A. , Tamura N., Lemer S., Giuffre A.J., Giribet G., Eiler J.M., Knoll A.H. (2017) Nacre tablet thickness records formation temperature in modern and fossil shells. *Earth and Planetary Science Letters*, Vol. 460, pp. 281–292, https://doi.org/10.1016/j.epsl.2016.11.012

Hänni H.A. (2006) A short review of the use of 'keshi' as a term to describe pearls. *Journal of Gemmology*, Vol. 30, No. 1/2, pp. 52–58 http://dx.doi.org/10.15506/JoG.2006.30.1.51

——— (2007) A description of pearl farming with *Pinctada maxima* in South East Asia. *Journal of Gemmology*, Vol. 30, No.

7/8, pp. 357–365, http://dx.doi.org/10.15506/JoG.2007.30.7.357
——— (2012) Natural pearls and cultured pearls: a basic concept and its variations. *The Australian Gemmologist*, Vol. 24, No. 11, pp. 256–266.
Homkrajae A. (2016) Gem News International: Spectral characteristics of *Pinctada mazatlanica* and *Pinctada margaritifera* pearl oyster species. *G&G*, Vol. 52, No. 2, pp. 207–208.
Jacob D.E., Wirth R., Soldati A.L., Wehrmeister U., Schreiber A. (2011) Amorphous calcium carbonate in the shells of adult *Unionoida*. *Journal of Structural Biology*, Vol. 173, No. 2, pp. 241–249, https://doi.org/10.1016/j.jsb.2010.09.011
Karampelas S. (2012) Spectral characteristics of natural-color saltwater cultured pearls from *Pinctada maxima*. *G&G*, Vol. 48, No. 3, pp. 193–197, http://dx.doi.org/10.5741/GEMS.48.3.193
Karampelas S., Fritsch E., Mevellec J.-Y., Gauthier J.-P., Sklavounos S., Soldatos T. (2007) Determination by Raman scattering of the nature of pigments in cultured freshwater pearls from the mollusk *Hyriopsis cumingi*. *Journal of Raman Spectroscopy*, Vol. 38, No. 2, pp. 217–230, http://dx.doi.org/10.1002/jrs.1626
Karampelas S., Fritsch E., Mevellec J.-Y., Sklavounos S., Soldatos T. (2009) Role of polyenes in the coloration of cultured freshwater pearls. *European Journal of Mineralogy*, Vol. 21, No. 1, pp. 85–97, http://dx.doi.org/10.1127/0935-1221/2009/0021-1897
Karampelas S., Fritsch E., Hainschwang T., Gauthier J.-P. (2011) Spectral differentiation of natural-color saltwater cultured pearls from *Pinctada margaritifera* and *Pteria sterna*. *G&G*, Vol. 47, No. 2, p. 117.
Kiefert L., Moreno D.M., Arizmendi E., Hänni H.A., Elen S. (2004) Cultured pearls from the Gulf of California, Mexico. *G&G*, Vol. 40, No. 1, pp. 26–39, http://dx.doi.org/10.5741/GEMS.40.1.26
Kripa V., Mohamed K.S., Appukuttan K.K., Velayudhan T.S. (2007) Production of Akoya pearls from the Southwest coast of India. *Aquaculture*, Vol. 262, No. 2-4, pp. 347–354, https://doi.org/10.1016/j.aquaculture.2006.09.047
Marxen J.C., Hammer M., Gehrke T., Becker W. (1998) Carbohydrates of the organic shell matrix and the shell-forming tissue of the snail *Biomphalaria glabrata* (Say). *The Biological Bulletin*, Vol. 194, No. 2, pp. 231–240, http://dx.doi.org/10.2307/1543052
Miyoshi T., Matsuda Y., Komatsu H. (1987) Fluorescence from pearls to distinguish mother oysters used in pearl culture. *Japanese Journal of Applied Physics*, Vol. 26, Part 1, No. 4, pp. 578–581, http://dx.doi.org/10.1143/JJAP.26.578
O'Connor W.A., Lawler N.F., Heasman M.P. (2003) Trial farming the akoya pearl oyster, *Pinctada imbricata*, in Port Stephens, NSW: Final Report to Australian Radiata Pty Ltd., pp. 1440–3544.
Otter L.M., Wehrmeister U., Enzmann F., Wolf M., Jacob D.E. (2014) A look inside a remarkably large beaded South Sea cultured pearl. *G&G*, Vol. 50, No. 1, pp. 58–62, http://dx.doi.org/10.5741/GEMS.50.1.58
Scarratt K., Bracher P., Bracher M., Attawi A., Safar A., Saeseaw S., Homkrajae A., Sturman N. (2012) Natural pearls from Australian *Pinctada maxima*. *G&G*, Vol. 48, No. 4, pp. 236–261, http://dx.doi.org/10.5741/GEMS.48.4.236
Soldati A.L., Jacob D.E., Wehrmeister U., Häger T., Hofmeister W. (2008) Micro-Raman spectroscopy of pigments contained in different calcium carbonate polymorphs from freshwater cultured pearls. *Journal of Raman Spectroscopy*, Vol. 39, No. 4, pp. 525–536, http://dx.doi.org/10.1002/jrs.1873
Strack E. (2006) *Pearls*. Rühle-Diebener, Stuttgart, Germany.
Urmos J., Sharma S.K., Mackenzie F.T. (1991) Characterization of some biogenic carbonates with Raman spectroscopy. *American Mineralogist*, Vol. 76, No. 3-4, pp. 641–646.
Wehrmeister U., Jacob D.E., Soldati A.L., Loges N., Häger T., Hofmeister W. (2011) Amorphous, nanocrystalline and crystalline calcium carbonates in biological materials. *Journal of Raman Spectroscopy*, Vol. 42, No. 5, pp. 926–935, http://dx.doi.org/10.1002/jrs.2835
Xu B., Poduska K.M. (2014) Linking crystal structure with temperature-sensitive vibrational modes in calcium carbonate minerals. *Physical Chemistry Chemical Physics*, Vol. 16, No. 33, pp. 17634–17639, http://dx.doi.org/10.1039/C4CP01772B

Accurate Reporting of Key Trace Elements in Ruby and Sapphire Using Matrix-Matched Standards

Jennifer Stone-Sundberg, Timothy Thomas, Ziyin Sun, Yunbin Guan, Zachary Cole, Randy Equall, and John L. Emmett

To improve the accuracy and efficiency of trace element analysis in ruby and sapphire, standards sets containing matrix-matched corundum with targeted levels of beryllium, magnesium, silicon, titanium, vanadium, chromium, iron, and gallium were created. Ultra-high-purity corundum was also incorporated as a "true matrix zero." To our knowledge, these sets contain the most accurate standards for the key trace elements in corundum today. The standards were designed to cover the optimal range of the main trace elements typically characterized in natural ruby and sapphire. Additionally, we were able to accurately quantify silicon in corundum by successfully resolving the $^{28}Si^{+}$ peak from the $^{27}Al^{1}H^{+}$ peak using the superior mass resolving power of secondary ion mass spectrometry (SIMS) as compared to laser ablation–inductively coupled plasma–quadrupole mass spectrometry (LA-ICP-QMS).

To correctly assign geographic origin (Emori and Kitawaki, 2015; Sutherland et al., 2015), formation history (Peucat et al., 2007), and color mechanisms (Emmett et al., 2003) in ruby and all colors of sapphire, accurate key trace element data is an essential component. As magnesium, titanium, vanadium, chromium, iron, and gallium are found in all natural sapphire in varying amounts, these trace elements are identified as the key trace elements for natural corundum. Additionally, beryllium is significant to quantify, as the presence of this trace element can indicate treatment. The various quantitative trace element detection techniques used today for analyzing mineral species—electron microprobe, X-ray fluorescence (XRF), secondary ion mass spectrometry (SIMS), laser-induced breakdown spectroscopy (LIBS), and laser ablation–inductively coupled plasma–mass spectrometry (LA-ICP-MS)—require standards for each trace element of interest. Essentially, these sophisticated and expensive instruments that allow us to quantify the trace elements in gems can only be as accurate as the standards used. With gemological laboratories issuing origin reports for ruby, sapphire, and other gems, it is essential to have a high level of certainty associated with the quantitative determination of trace element chemistry. The standard's "matrix," the material that it is comprised of, matters a great deal: Matching both the composition and structure of the standard to those of the sample being analyzed will yield the most accurate results (Sylvester, 2008). For example, trace levels of vanadium in ruby (or any of the colors of sapphire) are most accurately quantified by comparing against a piece of single-crystal corundum with a known level of vanadium in it as opposed to some other material containing vanadium, such as silicate glass.

However, commonly used standards such as those produced by the National Institute of Standards and Technology (NIST) are generally not available in matrix-specific forms, so silicate glasses such as NIST Standard Reference Materials (SRM) 610 and 612 are frequently applied. As the silicate glass matrix differs significantly from the crystalline alumina matrix of sapphires and rubies in both composition and structure, what is known as a "matrix effect" can occur. This effect leads to inaccuracy for many of the key trace elements characterized. A potential outcome of calibrating an instrument with a matrix different from the sample to be measured is the enhancement or suppression of trace element levels detected (Strasheim and Brandt, 1967). Furthermore, NIST SRM 610 and 612 glasses are not certified for many of the trace elements they are being used for, as is the case for corundum, and both have been shown to

See end of article for About the Authors and Acknowledgments.
Gems & Gemology, Vol. 53, No. 4, pp. 438–451,
http://dx.doi.org/10.5741/GEMS.53.4.438

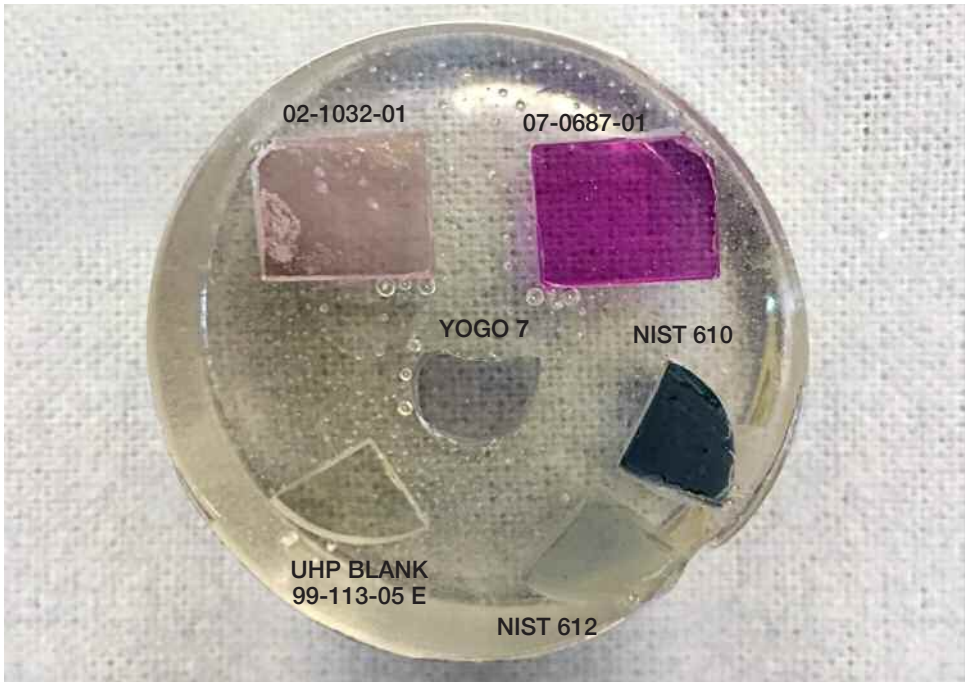

Figure 1. One of GIA's new LA-ICP-MS corundum calibration standards sets (set number 1); the epoxy disk containing the set is 1.5 inches in diameter. NIST SRM 610 and 612 glass standards are included to account for trace and non-trace elements, such as those found in inclusions, that were not incorporated into the synthetic sapphire crystals grown for standards. Photo by Jennifer Stone-Sundberg.

demonstrate variability (Pearce et al., 1997). Of the key trace elements normally analyzed in corundum, these glasses are only certified for iron and chromium (certificates of analysis from NIST are available at https://nemo.nist.gov/srmors/certificates/view_certGIF.cfm?certificate=610 and https://nemo.nist.gov/srmors/certificates/view_certGIF.cfm?certificate=612). Another drawback to the NIST glasses for corundum: Aluminum is present at low concentrations (around 1 wt.%) in the NIST glasses but is a major element in corundum (around 52.9 wt.%). The projection from low concentration to high concentration from the standards to unknowns can introduce significant error—projections work best when similar concentrations are compared between standard and unknown.

In Brief

- New corundum standards have been developed for improved accuracy and efficiency in trace element quantification using LA-ICP-MS.
- A true matrix-matched zero was introduced to further minimize matrix effects.
- The GIA research collection was used to establish meaningful target levels of the trace elements of interest for the standards.

Due to concerns regarding composition and structure matrix effects, GIA decided years ago to generate corundum standards for its LA-ICP-MS instruments (Wang et al., 2006). After a decade of use for both production and research applications, new standards sets have been created to further improve accuracy (discussed in the Background section) and efficiency. To optimize the new standards sets for regular laboratory use, each individual set contains a minimum number of standards (in our case, four pieces of corundum and NIST SRM 610 and 612 glasses embedded in epoxy—see figure 1), reasonably capturing the range of interest for each key trace element to be quantified. As there is a need to characterize many samples routinely for origin reporting, efficiency is paramount. We reduced calibration time by combining as many trace elements as possible into single standards. We accomplished this by growing "multi-doped" synthetic corundum crystals. Instead of having only one or two of the trace elements of interest in a single standard, we worked with FLIR's crystal growth group, Scientific Materials of Bozeman, Montana, to produce highly uniform Czochralski-grown single crystals of corundum containing up to six intentionally doped trace elements (figure 2). To incorporate beryllium into the standards, slices from one of these custom-grown crystals were diffused with beryllium for 100 hours at 1800°C in pure oxygen, generating one standard in which seven trace elements can be calibrated at the same time. Beyond re-

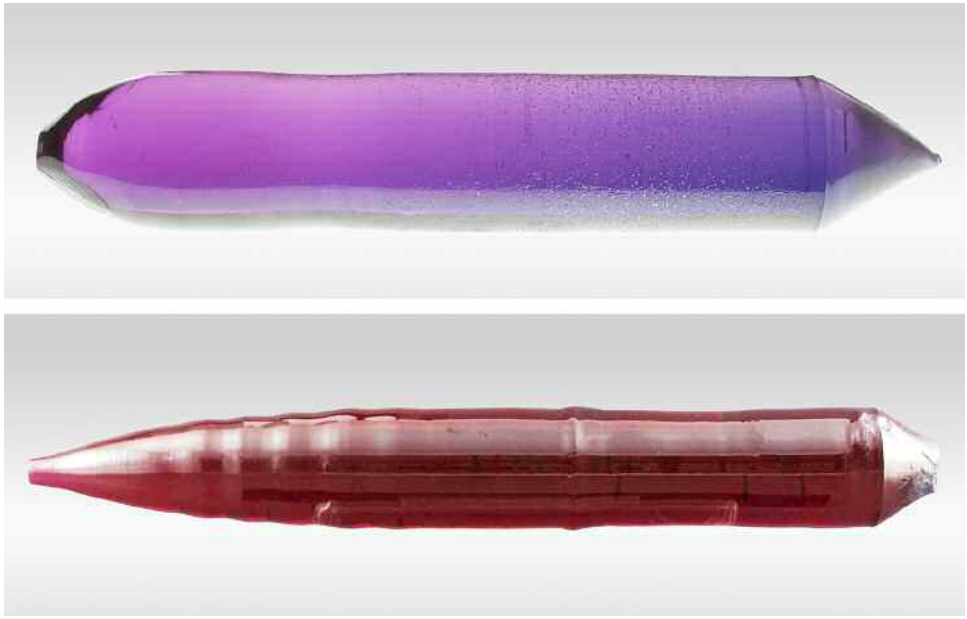

Figure 2. Crystal boules grown by Scientific Materials for multi-doped corundum standards: sample 02-1032 (top) and sample 07-0687 (bottom). Both crystals were doped with Mg, Ti, V, Cr, and Ga in different amounts; only 02-1032 was successfully doped with Fe. Crystal 02-1032 is 40 mm in diameter by 150 mm in length at diameter, and crystal 07-0687 is 30 mm in diameter by 150 mm in length at diameter. Photos courtesy of Scientific Materials.

ducing instrument calibration time, this approach of fewer individual measurements in the calibration cycle also enhances accuracy, precision, and repeatability, as there is less chance for instrument signal drift, and therefore more accurate conversion of instrument signal into trace element concentrations.

Even with this approach, it was impossible to incorporate all of the trace elements of interest into the synthetically grown crystals at levels that best represented what is found in natural corundum. As we were unable to produce a standard for mid-range to higher iron levels and moderate silicon concentrations with Czochralski growth, we selected a series of natural sapphires from Yogo Gulch, Montana.

BACKGROUND

Original and Next-Generation Corundum Standards Sets. The first corundum standards sets GIA created for its LA-ICP-MS instruments focused on accuracy by using matrix-matched standards. These sets consisted of seven different corundum standards: one high-iron natural sapphire and six synthetically grown sapphire crystals with either one or two intentionally doped trace elements each. A need for increased accuracy, better targeting of trace element levels in natural ruby and sapphire, and enhanced efficiency led to the development of the current generation of standards sets. To this end, we focused on the following criteria while minimizing uncertainty:

1. Using corundum that clearly displays highly uniform levels of the trace elements of interest
2. Capturing the appropriate ranges of the trace elements in our standards by matching them to levels occurring naturally in sapphire and ruby
3. Developing a high-purity blank sample to represent the absence of trace elements in corundum
4. Using the most accurate methods available for corundum as the basis of our calibration work

Uniformity of Trace Elements in the Standards. For a standard to produce accurate and reproducible results, it must be extremely homogenous (even more so for a spot method such as LA-ICP-MS than for a bulk method). Czochralski-grown synthetic crystals of corundum and other matrices are known for their exceptional crystal quality, including highly uniform distributions of trace elements. Demand in the 1960s for ruby crystals suitable for lasers led to the refinement of the Czochralski technique for the production of commercial solid-state lasers (Harris, 2004). For this reason, we chose the Czochralski technique as our growth method. As mentioned above, producing Czochralski-grown corundum with mid-range to high levels of iron and moderate levels of silicon was not practical, so we sourced extremely uniform Yogo sapphire crystals (shown in figure 3) from Eric Braunwart of Columbia Gem House (Vancouver, Washington). Surprisingly, we found with SIMS that in addition to iron, several of the other key trace elements of interest for corundum—including Mg, Si, Ti, and Ga—were as uniformly distributed in the natural Yogo sapphires as they were in the Czochralski-

grown material. We have confirmed that silicon and nickel are also present in Yogo sapphires in amounts up to 26 and 12 ppma, respectively, and are likewise homogenously distributed.

Targeting the Trace Element Levels in the Standards. To best determine the concentrations of trace elements in unknown samples, it is optimal to have standards that contain similar to somewhat higher levels of the same trace elements. We attempted to create standards with concentrations at the 50th percentile or higher of the key trace elements found in natural sapphire and ruby based on data from the GIA research collection. GIA has been gathering and cataloging natural ruby and sapphire from identified sources worldwide as part of its reference collection effort. The purpose of this collection is to carefully document material from each accessible source and to produce detailed information on the inclusions and trace element chemistry by location (Chapin et al., 2015; Pardieu and Vertriest, 2016). This collection contains over a thousand samples and is one that GIA adds to each time its field gemologists visit a unique mining area of commercial interest or significance. The collection includes basalt-related sapphire, metamorphic sapphire, marble-hosted ruby, high-iron ruby, and additional types of corundum beyond these four categories. The samples measured include gem and non-gem quality, and for the key trace elements, the data was quantified using the original corundum standards sets. For our purposes, we are limiting the discussion to these key trace elements that are found in the corundum matrix, and not those found in inclusions.

Figure 3. One of the slices of Yogo sapphire selected for its uniformity of blue color. The slice weighs 0.117 grams and measures approximately 5.8 × 7.6 × 0.9 mm. The small dots are laser ablation spots. Photo by John L. Emmett.

TABLE 1. Key trace elements in natural corundum from GIA's reference collection.

	Levels of natural occurrence (ppma)			
	Sapphire		Ruby	
Trace element	50th percentile	75th percentile	50th percentile	75th percentile
Mg	50	75	40	100
Ti	55	100	50	85
V	5	10	15	100
Cr	2	5	900	1300
Fe	210	620	325	845
Ga	20	25	10	15

Using data from the GIA reference collection, we considered the entire range of each key trace element detected, with the 50th and 75th percentiles presented in table 1. It is worth noting that the highest levels detected can be considerably higher than the 75th percentile levels reported. For beryllium, where we were interested in detecting diffusion treatment (Emmett et al., 2003), we targeted around 60 ppma, a level sufficient to distinguish between diffused samples (where the surface of the gem can show significant beryllium levels) and undiffused samples (with beryllium levels that are undetectable or very low, such as 1–2 ppma).

Introduction of a Matrix-Matched Zero. The new standards sets address accuracy in part by incorporating a true matrix-matched "zero"—a piece of ultra-high-purity sapphire containing essentially no detectable trace elements. Using this approach of defining the zero signal point for each of the trace elements as the pure matrix instead of a background of solely helium gas minimizes matrix effects, as interferences will be eliminated and the zero point of the calibration line will now be far more accurate (Lin et al., 2016). Standard undoped colorless sapphire and high-purity alumina powders used commercially still contain several ppmw of various trace elements such as chromium, titanium, magnesium, and iron. For example, high-purity alumina with a 5N designation (meaning "five nines," or 99.999% purity) still contains up to 10 ppmw combined trace elemental

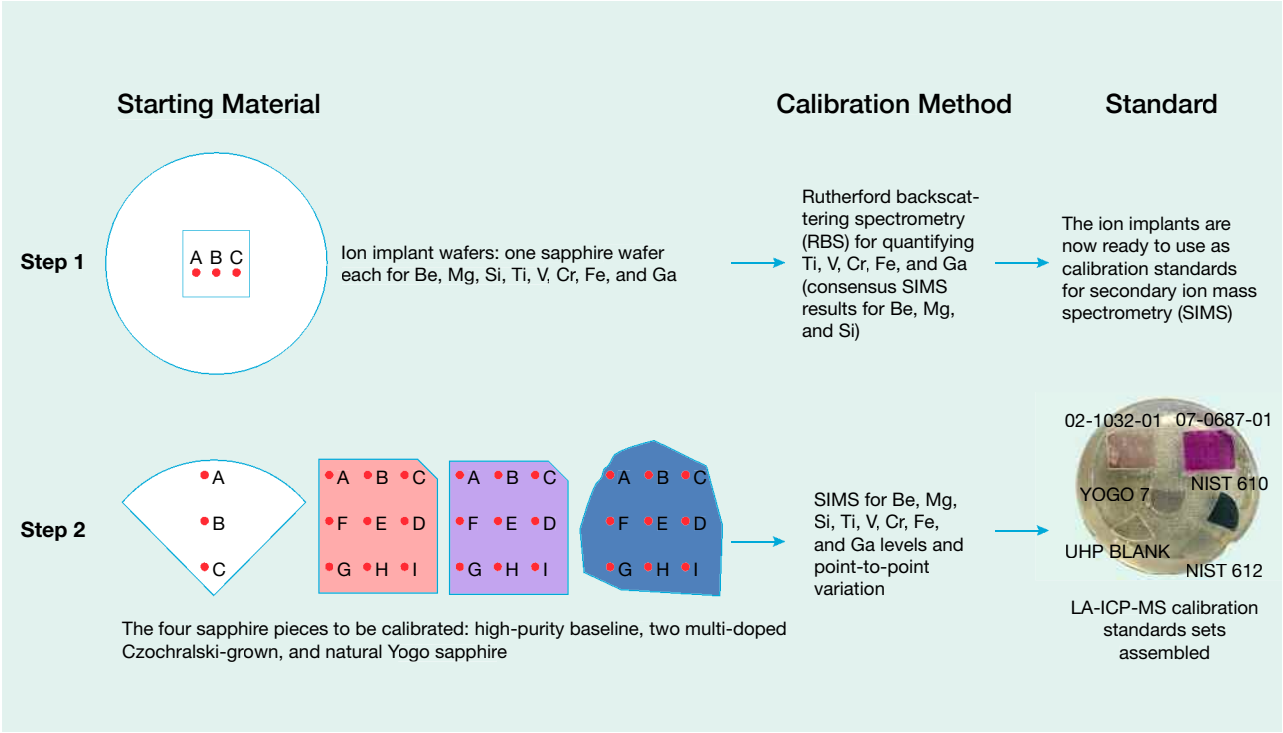

Figure 4. The process outline used to create the new corundum calibration standards.

impurities. For our purposes, it was important to obtain undoped sapphire of significantly higher purity—ideally 6N or better. To accomplish this, the most refined single-crystal sapphire known to us was acquired from Chandra Khattak of the former Crystal Systems Corporation (sold to GT Advanced Technologies in 2010). The single-crystal sapphire was material that had been recrystallized multiple times using the heat exchanger method (HEM) to further reduce the impurity levels found in the original aluminum oxide raw material (Khattak and Schmid, 2001).

Ensuring Accuracy. As mentioned earlier, the accuracy of the measurements obtained from standards-dependent quantitative analytical techniques employed by many research laboratories is limited by the adequacy of the standards used. To improve the accuracy of the new standards sets over the original sets, many steps were taken to develop a highly accurate calibration methodology with minimal combined uncertainty (figure 4). We sought a method based on first principles for determining the levels of the trace elements of interest in our standards. In other words, we wanted a way of determining trace element levels in corundum that did not require referencing the levels of those same trace elements in some other standard (i.e., a noncircular method). This led us to an approach used by the geology community in which individual ion implant doses verified by Rutherford backscattering spectrometry (RBS) are used to calibrate the SIMS apparatus prior to measuring final samples (Burnett et al., 2015). As the concentrations of the ion implants arrived at from the voltage and current settings are accurate to only about 30% (Burnett et al., 2015)—an unacceptable level of uncertainty for our purposes—the actual dosing levels achieved for each ion-implanted wafer were determined through multiple RBS characterizations (or for the lighter isotopes ^{9}Be, ^{24}Mg, and ^{28}Si where this was not practical, through a method described below). RBS is a nondestructive first-principles (standardless) quantitative analytical technique that is capable of 1% absolute accuracy (Colaux and Jeynes, 2014). SIMS was chosen as our technique for performing the ultimate calibration work on the final corundum standards, as it is a precise technique with fine mass-resolving power capable of quantifying all of the elements of interest to us.

As trace elements are not distributed with absolute uniformity in synthetic sapphire, and each natural Yogo sapphire slice will have its own composition, nine points on all individual pieces for

each standards set were characterized by SIMS (see figure 4). Simply put, the same standard type in each standards set has its own unique set of values. This is quite a departure from the SRM NIST 610 and 612 glasses, where most researchers refer to published tables for the concentrations of the trace elements (certified and uncertified) contained within *any* piece of a particular series of NIST glass, of which there are thousands of pieces worldwide (Pearce et al., 1997). For example, the chromium level in a Czochralski-grown corundum crystal is nearly uniform from top to bottom, but its distribution coefficient will result in pieces from the bottom of the crystal having levels slightly lower than those from the top. To label the entire crystal as having a single chromium concentration would result in inaccuracy. As SIMS can easily quantify not only differences between the top and bottom of the crystal, but also point-to-point differences across areas less than one square millimeter, we made sure to quantify the levels of chromium (and all of the other trace elements) individually for each separate standard piece from each source. These characterized standards were now ready to be assembled into finished sets for GIA's LA-ICP-MS instruments.

To most accurately report data based on our new corundum standards, it is necessary to calculate the total uncertainty in the final values for each trace element in each standard, factoring in all measurement and instrument errors and uncertainties. We accounted for all of the sources of errors and uncertainties to the best of our ability and combined them via the root sum of the squares method following the NIST-referenced INC-1 (1980) recommendation reached by the Working Group on the Statement of Uncertainties, approved by both the International Committee for Weights and Measures (CIPM) and the International Bureau of Weights and Measures (BIPM).

MATERIALS AND METHODS

Crystals for Standards. *Crystal Growth*. As mentioned, we selected the Czochralski method, known for producing crystals of high quality with uniform doping of trace elements, to grow synthetic sapphire crystals containing the key trace elements for our standards. After many crystal growth runs to best understand the doping characteristics of each trace element of interest, two final crystals were grown by Scientific Materials to provide material to be used in our standards sets. These two samples were both doped with the trace elements Mg, Ti, V, Cr, Fe, and Ga. Crystal 02-1032 had lower concentrations of Mg, Ti, and Cr and higher concentrations of V, Fe, and Ga; crystal 07-0687 had lower concentrations of V, Fe, and Ga and higher concentrations of Mg, Ti, and Cr (figure 2 top and bottom, respectively). Pieces from crystal 02-1032 were subsequently diffused with Be for a period of 100 hours at 1800°C in pure oxygen to provide a standard for this trace element. From each of the two boules, seven polished slices measuring 8 × 10 × 2 mm were fabricated by Scientific Materials. These seven pieces from each boule constitute only a small fraction of the total available material for the two boules.

Both crystals were grown directly from the melt at approximately 2050°C and pulled from iridium crucibles using seeds at an orientation 60° off the c-axis (the growth direction was perpendicular to the n-plane, to facilitate growth of more defect-free material). The raw materials used were 5N purity powders of Al_2O_3 and dopant metal oxides. After the powders were loaded into iridium crucibles, the crystals were grown in a nitrogen atmosphere containing 3,000 ppmw oxygen. The crystals were pulled at an extraction rate of 0.015 inches (0.38 mm) per hour. The final size of crystal 02-1032 was 40 mm in diameter by 150 mm in length at diameter. The final size of crystal 07-0687 was 30 mm in diameter by 150 mm in length at diameter.

Magnesium, titanium, and vanadium were "well-behaved ions" under the growth conditions used, in that they did not exhibit vaporization and their incorporation into the crystals was predictable based on our knowledge of their distribution coefficients. For chromium, iron, and gallium, some vaporization was noted and they were less predictably incorporated into the grown crystals under the conditions used. Therefore, maintaining well-controlled growth conditions to reduce variability was critical.

Ultra-High-Purity Corundum. The ultra-high-purity corundum was obtained from the former Crystal Systems, which employed the HEM technique for producing UV-grade sapphire. To enhance the purity of the material, the sapphire was recrystallized multiple times (C. Khattak, pers. comm., 2003). Ultimately, we determined a combined total ppma level of less than 0.5 for the key trace elements in this material. Seven finished pieces were fabricated from this material by Scientific Materials.

Yogo Sapphire. Several polished slices of highly uniform light blue Yogo sapphire crystals were carefully selected by Eric Braunwart of Columbia Gem House.

TABLE 2. Consensus SIMS and RBS results in the ion-implanted corundum wafers.

Isotope	Implanter target dose (at/cm^2)	Average of measured fluence (at/cm^2)	Combined uncertainty for mean and measurements	% combined uncertainty for mean and measurements
^{9}Be	1.00 x 10^{15}	1.22 x 10^{15}	3.55 x 10^{13}	2.90%
^{24}Mg	1.00 x 10^{14}	1.00 x 10^{14}	4.60 x 10^{12}	4.60%
^{28}Si	1.00 x 10^{15}	1.32 x 10^{15}	8.45 x 10^{13}	6.40%
^{48}Ti	1.00 x 10^{15}	1.03 x 10^{15}	7.06 x 10^{13}	6.85%
^{51}V	1.00 x 10^{15}	1.09 x 10^{15}	5.46 x 10^{13}	5.03%
^{52}Cr	1.00 x 10^{15}	1.12 x 10^{15}	5.00 x 10^{13}	4.46%
^{56}Fe	1.00 x 10^{15}	1.10 x 10^{15}	5.68 x 10^{13}	5.15%
^{69}Ga	1.00 x 10^{15}	1.05 x 10^{15}	5.29 x 10^{13}	5.02%

We obtained seven for our standards sets. Yogo sapphires are known for mid-range to high iron content and exceptional color uniformity (Mychaluk, 1995; Emmett et al., 2017), which we expected would correspond to trace element uniformity (figure 3).

Standards Characterization. Our pursuit of accuracy led us to create the standards sets using a two-step approach: First, create highly controlled and measurable standards (ion implants) to calibrate extremely precise instrumentation (SIMS), and then use the standardized SIMS to calibrate selected corundum pieces to be incorporated into final product standards sets (see figure 4). The steps taken to create the SIMS calibration standards and then the final product corundum calibration standards for GIA's LA-ICP-MS instruments are listed below.

Ion Implant Standards Creation. The first step was to create a separate calibration standard for each trace element of interest in a corundum matrix. This was accomplished at INNOViON Corporation (San Jose, California) using ion implantation, a method that allows one to precisely control the concentration (dose) and depth profile of a specific amount of a trace element to be placed into a matrix (Ryssel and Ruge, 1986). Single isotopes of ^{9}Be, ^{24}Mg, ^{28}Si, ^{48}Ti, ^{51}V, ^{52}Cr, ^{56}Fe, and ^{69}Ga were implanted separately into their own two-inch-diameter high-purity corundum wafer on top of a four-inch-diameter silicon wafer (except in the cases of ^{24}Mg and ^{28}Si, in which their two-inch-diameter corundum wafers were placed on top of four-inch-diameter gallium arsenide wafers). The four-inch silicon or gallium arsenide wafers functioned as witness samples for the ion implantation process. The target dose (or "fluence") for each isotope was 1.00 × 10^{15} at/cm^2 (except ^{24}Mg, which targeted a 1.00 × 10^{14} at/cm^2 dose). The implant energy used for our wafers was 200 KeV for all isotopes except ^{9}Be, which used an energy of 100 KeV. For all wafers, the tilt angle between the ion beam and the wafer surface normal was 7°.

Verification of the Ion Implant Dosing. For the key trace elements that are significantly heavier than the matrix elements aluminum and oxygen (Ti, V, Cr, Fe, and Ga), RBS was used to determine the actual dosing. The RBS technique can determine the concentrations with depth of isotopes in a matrix of lighter elements by bombarding a sample with a beam of high-energy particles and measuring the number and energy of backscattered ions (Verma, 2007). For those key trace elements that are close in mass or lighter than aluminum and oxygen (Be, Mg, Si), the ion implant dosing had to be verified by a consensus-dosing approach using comparisons to well-characterized existing implants.

The implant doses of the heavier isotopes ^{48}Ti, ^{51}V, ^{52}Cr, ^{56}Fe, and ^{69}Ga were characterized by RBS at Evans Analytical Group (EAG) in Sunnyvale, California; the Ion Beam Laboratory at the University at Albany, State University of New York (SUNY); and the Tandetron Accelerator Laboratory of the University of Western Ontario (UWO) in London, Ontario. For all measurements, a He^{++} ion beam with energy between 2 and 3 MeV was used.

To characterize the ion implant standards lighter than or close in mass to Al (^{9}Be, ^{24}Mg, and ^{28}Si), EAG determined "consensus doses" (doses based on several verifications) using SIMS and their multiple reference standards for Be in Si, and Mg and Si in GaAs. When these lighter ions were implanted in their sapphire substrates, they were simultaneously implanted into larger-diameter "witness" substrates of silicon or gallium arsenide that the sapphire substrates were placed on top of. These witness samples

BOX A: SIMS RSF AND TRACE ELEMENT CONCENTRATION DETERMINATION

With the RBS "dose" or "fluence" values Ψ (units of atoms/cm^2), SIMS RSF values—the conversion factors between SIMS data for a particular element in a sample and its concentration—can be determined in the following way.

We first sputter the ion implant standards with SIMS to collect the counts of the implanted ion and matrix ion. This implanted ion, or "ion of interest," is also referred to as the "secondary ion of interest." We express the ion counting rate of the implanted isotope as $I(x)_1$, which is also the current of the implanted isotope. Similarly, the ion counting rate of the matrix isotope—in the case of a corundum matrix this would be $^{27}Al^+$—is expressed as $I(m)_1$, which is also the current of the matrix isotope. The RSF (units of atoms/cm^3) can be determined using the relationship

$$RSF = \Psi / \int (I(x)_1 / I(m)_1) dx$$

where dx is the depth profile in angstroms and is determined by the product of the sputtering rate (S) in angstroms per second and the time interval in seconds recorded during the SIMS analysis:

$$dx = Sdt$$

The sputtering rate is the ratio of the simulated peak depth to the peak time in seconds:

$$S = \text{Peak depth}/\text{Peak time}$$

We attempted peak depth determination by both physical measurements and calculation with "Stopping and Ranges of Ions in Matter" (SRIM). Because of the small non-flat-bottom craters in sapphire, large uncertainties exist in physical depth measurements. The peak depths are currently calculated with SRIM, before more accurate depth measurements can be achieved.

Once the RSF values for each trace element in the matrix have been determined, the atomic concentrations—n(x)—of these trace elements in other samples can be determined using the product of the RSF with the ratio of the secondary ion counting rates:

$$n(x) = RSF \times (I(x)_2)/(I(m)_2)$$

where $I(x)_2$ is the secondary ion counting rate, or current of the trace element isotope in a sample, and $I(m)_2$ is the secondary ion counting rate, or current of the matrix isotope—in our case, $^{27}Al^+$.

were then measured with SIMS and directly compared to the existing reference standards produced and used by EAG. These standards served as calibrators for the SIMS to determine the doses in our witness samples. For Be, Mg, and Si, EAG had three, four, and five existing standards, respectively. We assumed that the doses in the witness samples were identical to those in the actual sapphire substrates, which was shown to be true for the heavier implants for titanium, vanadium, chromium, iron, and gallium that each had silicon witness samples under them during the implantation process.

Calibration of the SIMS and Characterization of the Final Standards. SIMS is a highly sensitive and precise quantification technique for elements from Be to U (Benninghoven et al., 1987). The technique produces elemental depth profiles by sputtering samples with a primary beam of either oxygen or cesium ions and then analyzing the secondary ions formed with a mass spectrometer. Once the doses in the ion implant standards were accurately characterized, these standards were measured with SIMS under a controlled set of conditions to determine "relative sensitivity factors," or RSF values, for each trace element of interest to be characterized in corundum (Laufer et al., 2011). The RSF simply converts the SIMS signal for a particular trace element in a defined matrix under defined conditions into concentrations (see box A for a more detailed description). Our determined RSF values were then applied to data collected on the pieces of corundum that are now in our corundum standards sets under the same controlled set of operating conditions to accurately quantify these same trace elements. The RSF values for each trace element were determined from a series of two to four spots on the appropriate ion implant standard, verified in two separate measurement sessions on nonconsecutive days. The concentration values with combined uncertainties for each piece of corundum incorporated into the standards sets were obtained with SIMS based on averaging nine spots per piece.

SIMS Instrument Description and Operating Conditions. The CAMECA IMS 7f-GEO at Caltech (Pasadena, California) is a magnetic sector type SIMS instrument with dedicated options for geoscience applications. Modified from the CAMECA IMS 7f-Auto, it is equipped with double secondary Faraday cups for high-precision stable isotope analysis. The primary column consists of a duoplasmatron source; a microbeam Cs ionization source; a primary beam mass filter; fully automated slits and apertures; ion optics (lenses, stigmators, and double deflectors) for primary

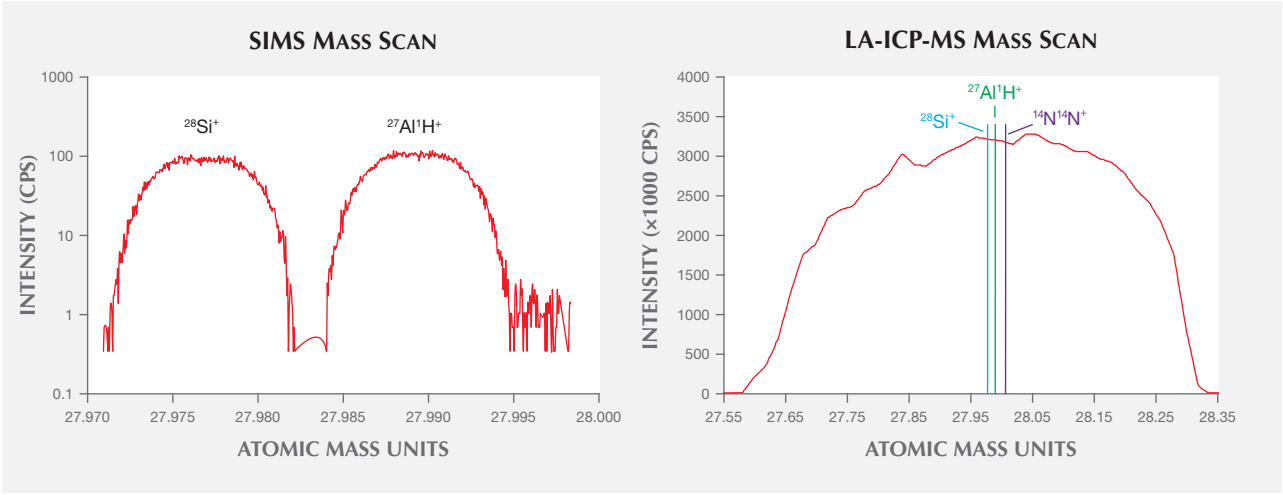

Figure 5. Left: $^{27}Al^1H^+$ interference to $^{28}Si^+$ for sapphire using SIMS. At a mass resolving power (MRP) of 3,000, the $^{27}Al^1H^+$ interference (mass of 27.98936 amu) to $^{28}Si^+$ (mass of 27.97692 amu) can be separated, allowing accurate quantification of Si in corundum. During SIMS measurements, the magnetic field is set to collect signals only from the center of the $^{28}Si^+$ peak. Right: For comparison, the LA-ICP-MS instrument described in the Materials and Methods section cannot resolve the $^{27}Al^1H^+$ interference to $^{28}Si^+$ for sapphire (or even the further away $^{14}N^{14}N^+$ interference). This mass scan shows that the peak width of ^{28}Si is 0.7 amu (vs. around 0.01 amu for SIMS), which means that the peak includes the combination of $^{14}N^{14}N^+$ (mass of 28.00615 amu), $^{28}Si^+$, and $^{27}Al^1H^+$.

beam focusing and rastering; and a high-accuracy primary Faraday cup combined with a fast beam blanking system for monitoring the primary beam intensity during measurements. The secondary ion optics are continuously adjustable from –10 to + 10 kV, with a continuously adjustable imaged field and a dynamic transfer system that optimizes transmission for an analyzed area up to 500 × 500 μm^2. The Nier-Johnson double-focusing mass spectrometer has fully adjustable position and width on automated entrance and exit slits, automated contrast and field apertures, a spherical electrostatic analyzer for energy filtering, an automated continuously adjustable energy slit, and a laminated electromagnet (120 mm radius) for fast peak switching. The detection system consists of an electron multiplier, double Faraday cups, and a microchannel plate assembly.

RSF values for the elements of interest in corundum were determined through SIMS depth profiling of the implant standards. Because sapphire is an insulator and depth resolution is not a concern for this task, an O^- primary beam, which can minimize sample charging during measurement, was used to acquire depth profiles of the implant standards. Matched analytical conditions were then used to determine the element concentrations of the non-implant samples. Specifically, the O^- primary beam current has a potential of –13 KeV, a current of approximately 15 nA, and a size of about 15 μm. Positive secondary ions of 8.5 KeV were generated by the primary beam, rastering an area of 50 × 50 μm^2 on sample surfaces. To avoid crater edge effects, a field aperture was inserted on the secondary ion path so that only the signals from the center 20 μm^2 area were detected. The positive secondary ions collected were ^{9}Be, ^{24}Mg, ^{27}Al, ^{28}Si, ^{46}Ti (samples), ^{48}Ti (implants), ^{51}V, ^{52}Cr, ^{56}Fe, ^{69}Ga (implants), and ^{71}Ga (samples). All secondary ions except ^{27}Al were measured with an electron multiplier (EM). ^{27}Al was measured with a Faraday cup because of its high intensity. The reason for measuring ^{46}Ti instead of ^{48}Ti on samples is to avoid possible unresolvable interference from ^{48}Ca (0.187% natural abundance of all Ca), whereas the isotopic abundance of ^{46}Ca is only 0.004%. The reason for measuring ^{71}Ga instead of ^{69}Ga on samples is to avoid possible unresolvable interferences from $^{56}Fe^{13}C$, $^{57}Fe^{12}C$, and $^{53}Cr^{16}O$, as Fe and Cr are both potentially present in the samples. Because of the high ^{48}Ti fluence of the implant standard, the possible ^{48}Ca interference has no significant contribution to its ^{48}Ti depth profiling results. The mass spectrometer of the SIMS was set at a mass resolving power (MRP) of 3,000 for all the measurements, which is sufficient to resolve all possible interferences to the masses of interest, especially the $^{27}Al^1H^+$ interference (mass = 27.98936 unified atomic mass units, or amu) to $^{28}Si^+$ (mass = 27.97692 amu) with an MRP of 2,251, which is significant due to the abundant Al in sapphire (as shown in figure 5). The lowest concentrations

in ppma we could detect with confidence for the key trace elements were 0.0003 for Be, 0.0002 for Mg, 0.2 for Si, 0.007 for Ti, 0.007 for V, 0.003 for Cr, 0.0006 for Fe, and 0.0005 for Ga.

Testing Standards and Samples with LA-ICP-MS. To examine the differences in using NIST glasses versus our new corundum standards for LA-ICP-MS calibration, we used a Thermo Fisher Scientific iCAP Qc ICP-MS and a New Wave Research UP-213 laser ablation unit with a frequency-quintupled Nd:YAG laser running at 4 ns pulse width. Ablation was achieved using a 55-µm-diameter circular laser spot, a fluence (energy density) of approximately 10 J/cm^2, and a 15 Hz repetition rate. The internal standard used was ^{27}Al with a value of 529,200 ppmw calculated and rounded from pure corundum. The dwell time of each laser spot was 40 seconds. The lowest concentrations in ppma we can detect with confidence by LA-ICP-QMS are 0.5 for Be, 0.1 for Mg, 0.5 for Ti, 0.05 for V, 0.2 for Cr, 3.5 for Fe, and 0.01 for Ga.

RESULTS AND DISCUSSION

Verification of the SIMS Calibration Standards. A summary of the consensus SIMS results from EAG for the actual doses of ^{9}Be, ^{24}Mg, and ^{28}Si as well as the RBS results from the three labs (EAG, SUNY, and UWO) for the actual doses of ^{48}Ti, ^{51}V, ^{52}Cr, ^{56}Fe, and ^{69}Ga in corundum are given in table 2. All values are presented with their combined uncertainties in terms of actual values and as a percentage of the determined doses. It is clear that verifying the ion-implanted doses was important in that the actual doses varied from the target doses from as little as zero to as much as 32%. The combined standard uncertainties at this point contain the uncertainties in the measured fluence values with each RBS measurement (or consensus SIMS measurement) and in calculating the mean values from the multiple RBS measurements for each fluence.

TABLE 3. RSF values for SIMS in corundum.

Isotope	RSF (atoms/cm^3)	%RSD
^{9}Be	1.99 x 10^{23}	2.42%
^{24}Mg	3.12 x 10^{22}	1.30%
^{28}Si	2.87 x 10^{23}	2.05%
^{48}Ti	5.08 x 10^{22}	1.10%
^{51}V	8.73 x 10^{22}	3.60%
^{52}Cr	5.87 x 10^{22}	1.99%
^{56}Fe	8.37 x 10^{22}	0.94%
^{69}Ga	5.31 x 10^{22}	5.76%

Determined RSF Values for SIMS. The RSF values with their relative standard deviations (RSD) are given in table 3. These values allow us to accurately calculate the actual concentrations of the key trace elements in our final standards originating from the custom-grown multi-doped crystals, the Yogo sapphire slices, and the ultra-high-purity blank sapphire.

Measured Values for the Final Corundum Calibration Standards. Using our RSF values, we calibrated the SIMS apparatus and determined the concentrations of the key trace elements in our new corundum standards based on nine separate points each. The

TABLE 4. Range of ppma values within the seven calibrated pieces of each crystal standard type with nine-point RSD value ranges from SIMS.

Trace element	02-1032-01 to 07		07-0687-01 to 07		Yogo-01 to 07	
Be	56–71	2–10%	—	—	—	—
Mg	24–26	1–4%	75–82	1–2%	(85–104)	(1–7%)
Si	—	—	—	—	22–26	1–5%
Ti	40–44	1–3%	106–115	1–4%	(76–104)	(1–8%)
V	39–43	1–3%	7–8	1–3%	(3–12)	(1–12%)
Cr	84–88	1% or less	599–621	1–2%	(3–26)	(4–93%)
Fe	34–36	1–8%	(2–3)	(1–6%)	1200–1410	1–2%
Ga	84–91	1–4%	2–4	2–4%	12–14	2–3%

"—" indicates level too low to calibrate, and "()" indicates that the trace element in the particular standard is not being used for calibration purposes. Gray cells indicate RSD ranges unacceptable for calibration purposes. Note that all of the trace elements in the Yogo sapphire are remarkably uniform except for chromium and vanadium.

ranges for each key trace element by crystal type with relative standard deviation ranges in the new standards sets are presented in table 4. These can be compared to the targeted ranges of values in table 1. The homogeneity achieved in the crystal growth and naturally present in the Yogo sapphires are demonstrated by the low RSD values accompanying the concentration ranges for those trace elements used for calibration purposes. Looking at the range of values by trace element within a standard type underscores the significance of individually calibrating each piece from the same source.

Table 5 presents the final data with total combined uncertainty (includes all measurement uncertainties from all steps) for the first standards set imaged in figure 1. As mentioned, high uniformity of the trace elements within the crystals is necessary to improve accuracy and reproducibility while minimizing uncertainty. For each standard, we used SIMS to collect nine uniformly distributed spots across the entire surface. We found that the relative standard deviations representing the point-to-point variations in the calibrated levels of trace elements within our standards ranged from less than 0.5% to no more than 10%. The highest variation was in the diffused beryllium in the 02-1032 crystal pieces. The lowest variations were in the chromium in the synthetically grown crystals and in the iron in the Yogo sapphire slices (all 2% or less).

Preliminary Comparison of LA-ICP-MS Data Using the New Standards Versus NIST SRM 610 and 612 Glasses. To grasp the significance of matrix effects for key trace element reporting in corundum using NIST SRM 610 and 612 glasses, we compared values determined for one of our standards sets (set 7), first using our RSF values with SIMS and then with LA-ICP-MS using a different corundum standards set (set 1), and finally with LA-ICP-MS using NIST SRM 610 and 612 glasses separately. Additionally, we used the new corundum standards set 1 separately from NIST SRM 610 and 612 glasses to measure a series of other samples using LA-ICP-MS. We were not able to measure this set of samples on SIMS but plan to do so with additional samples in the future. As shown in table 6, using the new standards calibrated by SIMS in the LA-ICP-MS instrument provided agreement within less than 10% of SIMS for standards set 7. Looking at calibrating the LA-ICP-MS with NIST 610 and 612 as compared to the matrix-matched standards, trends in differences between the measured samples for each trace element can be seen. For Be, Ti, V, Fe, and Ga, NIST SRM 610 and 612 glasses produce values consistently lower than the corundum standards. For Mg, NIST SRM 610 and 612 glasses produce values higher than the corundum standards. For Cr, the trend is not so clear, but the differences are within less than 10% of each other.

Accurate Quantitative Reporting of Silicon in Sapphire Using SIMS. Using SIMS with an MRP of 3,000, we were able to completely separate the $^{27}Al^{1}H^{+}$ interference from $^{28}Si^{+}$ (a mass scan around ^{28}Si, collected on a sapphire with 22 ppma Si, at a chamber vacuum level of approximately 2×10^{-9} torr; see figure 5), allowing us to accurately quantify Si concentration in corundum. The quantitative reporting of silicon in sapphire is a problem for many of the

TABLE 5. Trace element concentration values (in ppma) with total combined uncertainty in corundum calibration standards set number 1 (see figure 1).

Trace element	02-1032-01	Uncertainty	07-0687-01	Uncertainty	Yogo-07	Uncertainty
Be	68.5	4.4%	—	—	—	—
Mg	25.3	5.1%	76.0	4.8%	—	—
Si	—	—	—	—	23.9	7.6%
Ti	44.4	7.6%	111	7.2%	—	—
V	42.5	6.3%	7.41	6.3%	—	—
Cr	87.6	5.0%	599	5.2%	—	—
Fe	36.8	5.4%	—	—	1240	5.5%
Ga	86.3	7.7%	3.32	8.6%	12.4	8.0%

"—" indicates a trace element that was not present or not being used for calibration purposes within a standard.

TABLE 6. Comparison of LA-ICP-MS quantitative ppma data using matrix-matched corundum standards and NIST SRM 610 and 612 glass standards.

Sample	Trace element	SIMS	LA-ICP-MS set 1—new standards	LA-ICP-MS NIST 610	LA-ICP-MS NIST 612
02-1032-07	Be	56	56	48	44
77524	Be		69	46	46
02-1032-07	Mg	25	25	26	30
07-0687-07	Mg	76	77	81	95
Yogo-01	Mg	104	107	113	133
67293	Mg		7.6	8.0	9.6
02-1032-07	Ti	43	46	42	43
07-0687-07	Ti	106	110	101	103
76965	Ti		69	64	60
67923	Ti		4.4	4.0	3.8
02-1032-07	V	41	43	38	38
07-0687-07	V	7.2	7.9	6.7	6.7
69501	V		106	91	94
02-1032-07	Cr	86	86	84	83
07-0687-07	Cr	614	619	585	577
67925	Cr		1324	1384	1403
02-1032-07	Fe	36	33	29	14
Yogo-01	Fe	1353	1359	1142	552
67295	Fe		37	24	10
SD1	Fe		4039	2992	1177
02-1032-07	Ga	91	88	83	86
07-0687-07	Ga	3.8	3.5	3.3	3.4
Yogo-01	Ga	12	12	11	11
SD1	Ga		38	36	38
67292	Ga		312	272	306

Nine spots were used in both instruments.

LA-ICP-MS instruments used in gemological labs today, as they may not be capable of removing interferences and background from the isotope of interest, consequently yielding erroneously high results (Shen, 2010; Emmett et al., 2017). Using other techniques such as electron microprobe and XRF is not practical, as the detection limits for Si in corundum are orders of magnitude too high. LIBS with an intensified charge-coupled device (CCD) combined with a Czerny-Turner spectrometer might be more suitable than electron microprobe and XRF, but the limits of detection again for Si in corundum appear to be well above the 1 ppma range we are interested in.

Consider that the MRP for separating $^{28}Si^{+}$ (mass of 27.97693 amu and $^{27}Al^{1}H^{+}$ (mass of 27.98936 amu) is 2,251. The MRP of the instrument for a particular mass is the ratio of the isotopic mass of interest to the peak width at half maximum. To determine the mass resolution required to separate a particular isotope from a close-in-mass interference, we take the mass of the isotope of interest and divide by the absolute value of the difference between that isotopic mass and the mass of the interference of concern. Here, for $^{28}Si^{+}$ and $^{27}Al^{1}H^{+}$, the MRP is: 27.97693/(|27.97693 – 27.98936|) = 2,251. The MRP of quadrupole mass spectrometers used in many laboratories at atomic mass 28 is around 40 at normal resolution and tops out around 90 at high resolution. The required 2,251 MRP far exceeds the capability of these commercial "desktop" ICP-QMS used in a number of gemological labo-

ratories. One could consider trying to determine the Si trace element concentration using the ^{29}Si isotope (mass of 28.97649 amu), which has a much lower natural abundance (4.7% abundance vs. 92.2% abundance for ^{28}Si). However, the signal from such a low-abundance trace element would be very difficult to quantify and distinguish from traces of Si that might be present due to quartz elements in the torch assembly. Even if one could correct for these possible problems, there are still close-in-mass interferences such as ^{28}SiH and ^{29}N-N (28.98475 and 29.00318 amu, respectively) that require finer MRP (3,508 and 1,085, respectively) than the quadrupole detector is capable of. We decided to test measuring trace levels of silicon in corundum using a magnetic sector field ICP-MS paired with a 193 nm LA unit. This work is still ongoing, but signal intensity for our spot size of choice is proving to be an issue for either ^{29}Si or ^{28}Si at the medium mass resolution option (4,000–5,000 MRP) to quantify the levels of silicon we found in our Yogo sapphire samples using SIMS (22–26 ppma).

For further context, the use of the high-purity "blank" sapphire containing essentially no trace elements allows the LA-ICP-MS operator to see at what masses erroneous quantities of trace elements may be detected. Where there is an inexplicable signal compared to what is expected for the matrix alone, one can assume the signal originates from sources including interferences from plasma products, other contaminants, and residual atmospheric components. In an alumina substrate, where Si concentration is very low, the dominant peak at mass 28 is $^{27}Al^{1}H^{+}$, which varies accordingly with the H contents (vacuum level) available during measurements.

To illustrate this further, we measured our ultra-high-purity synthetic sapphire blank using the laser ablation–inductively coupled plasma–quadrupole mass spectrometer (LA-ICP-QMS) calibrated with NIST SRM 610. We found erroneous and highly varying levels of both ^{28}Si and ^{29}Si in our high-purity blank of 1136 ± 333 ppma and 1062 ± 182 ppma, respectively (using SIMS, the ^{28}Si level was below 1 ppma). This could help to explain in part the high levels of Si in corundum reported in previous literature using LA-ICP-MS and NIST SRM 610 or NIST SRM 612 standards (Peretti and Gunther, 2002; Peretti et al., 2003; Sutherland et al., 2015). After running a full mass scan from beryllium to uranium on the high-purity blank standard, also using NIST SRM 610 as a standard, we found that several trace elements beyond ^{28}Si and ^{29}Si would similarly be reported at erroneously high levels. These included ^{11}B (around 50 ppmw), ^{43}Ca (around 350 ppmw), ^{46}Ti (around 2 ppmw), ^{56,57}Fe (up to 18 ppmw), ^{67}Zn (around 50 ppmw), ^{95}Mo (around 0.4 ppmw, though this trace level may be contamination from the HEM crystal growth process), and ^{116,117,118,120}Sn (around 0.5 to 2.5 ppmw).

CONCLUSIONS

The need for improved accuracy and efficiency led GIA to develop new corundum standards sets for its LA-ICP-MS instruments. These sets:

1. Minimized the number of individual standards
2. Incorporated a true "zero" to represent the matrix background
3. Covered trace element levels that best represent the ranges found in natural ruby and sapphire of the key trace elements Mg, Ti, V, Cr, Fe, and Ga
4. Contained individual pieces that were calibrated using a highly controlled process based on, to the best of our knowledge, the most accurate methods technologically available today

Additionally, we were able to calibrate silicon in corundum standards, and with our determined SIMS RSF value for silicon in sapphire we were able to accurately characterize trace levels of this significant trace element using the high mass resolving power of SIMS.

These new standards sets were tailored to ensure high reproducibility, minimal calibration time, and less chance of instrument signal drift with fewer individual measurements in the calibration cycle. The creation of these standards was a lengthy and complex endeavor, incorporating custom crystal growth, creation of ion implant standards, and utilization of RBS and SIMS measurement techniques. We consider the end product well worth the effort, as these new standards allow us to more accurately study corundum chemistry for the purposes of both basic research and geographic origin reporting.

ABOUT THE AUTHORS

Dr. Stone-Sundberg is a GIA research scientist and a technical editor of Gems & Gemology *located in Portland, Oregon. Mr. Thomas is director and design engineering authority at Applied Materials in Hillsboro, Oregon. Mr. Sun is a staff gemologist at GIA in Carlsbad, California. Dr. Guan is laboratory director of the Microanalysis Center, Division of Geological & Planetary Sciences, at the California Institute of Technology in Pasadena, California. Mr. Cole is director of Scientific Materials in Bozeman, Montana. Dr. Equall is vice president of laser operations at FLIR. Dr. Emmett is director of Crystal Chemistry in Brush Prairie, Washington, and a consultant to GIA.*

ACKNOWLEDGMENTS

This work would not have been possible without the support of many individuals. Discussions with Prof. George Rossman at Caltech were invaluable during the course of the project. Discussions with Dr. Chandra Khattak regarding the high-purity material were very much appreciated. To help verify our data at various stages, discussions with Dr. Lyudmila Goncharova of the physics and astronomy department at the University of Western Ontario, Dr. Hassaram Bakhru at the State University of New York, Albany, and Dr. Tim West at Evans Analytical Group were most helpful. We recently worked with Professor Graham Pearson's lab on the issue of using sector field ICP-MS technology with 193 nm LA to accurately quantify low levels of silicon in corundum. Some preliminary work with Dr. Mandy Krebs and Dr. Yan Luo from Prof. Pearson's lab is underway, and results will be included in a future publication. Discussions with Dr. Karl Schmetzer regarding quantification of silicon in corundum were very much appreciated. We would like to thank Troy Ardon for creating "AtomicDensityCalculator" software for future SIMS data processing. Finally, the support of GIA management (Tom Moses and Shane McClure) was essential to see this project to the end.

REFERENCES

Benninghoven A., Rudenauer F.G., Werner H.W. (1987) *Secondary Ion Mass Spectrometry: Basic Concepts, Instrumental Aspects, Applications and Trends*. John Wiley & Sons, New York.

Burnett D.S., Jurewicz A.J.G., Woolum D.S., Wang J., Paque J.M., Nittler L.R., McKeegan K.D., Humayun M., Hervig R., Heber V.S., Guan Y. (2015) Ion implants as matrix-appropriate calibrators for geochemical ion probe analyses. *Geostandards and Geoanalytical Research*, Vol. 39, No. 3, pp. 265–276.

Chapin M., Pardieu V., Lucas A. (2015) Mozambique: A ruby discovery for the 21st century. *G&G*, Vol. 51, No. 1, pp. 44–54, http://dx.doi.org/10.5741/GEMS.51.1.44

Colaux J., Jeynes C. (2014) High accuracy traceable Rutherford backscattering spectrometery of ion implanted samples. *Analytical Methods*, Vol. 6, No. 1, pp. 120–129, http://dx.doi.org/10.1039/C3AY41398E

Emmett J.L., Scarratt K., McClure S., Moses T., Douthit T., Hughes R., Novak S., Shigley J., Wang W., Bordelon O., Kane R. (2003) Beryllium diffusion of ruby and sapphire. *G&G*, Vol. 39, No. 2, pp. 84–135, http://dx.doi.org/10.5741/GEMS.39.2.84

Emmett J.L., Stone-Sundberg J.L., Guan Y., Sun Z. (2017) The role of silicon in the color of gem corundum. *G&G*, Vol. 53, No. 1, pp. 42–47, http://dx.doi.org/10.5741/GEMS.53.1.42

Emori K., Kitawaki H. (2015) Geographic origin determination of ruby and blue sapphire based on trace element analysis using LA-ICP-MS and 3D plot. *Proceedings of the 34th International Gemmological Conference IGC*, Vilnius, Lithuania, pp. 48–50.

Harris D. (2004) A century of sapphire crystal growth. *Proceedings of the 10th DoD Electromagnetic Windows Symposium*, Norfolk, Virginia, May 2004, 17 pp.

Khattak C., Schmid F. (2001) Growth of the world's largest sapphire crystals. *Journal of Crystal Growth*, Vol. 225, No. 2-4, pp. 572–579, http://dx.doi.org/10.1016/S0022-0248(01)00955-1

Laufer A., Volbers N., Eisermann S., Potzger K., Geburt S., Ronning C., Meyer B.K. (2011) Determination of secondary ion mass spectrometry relative sensitivity factors for polar and non-polar ZnO. *Journal of Applied Physics*, Vol. 110, No. 9, pp. 094906-1–5, http://dx.doi.org/10.1063/1.3660417

Lin J., Liu Y., Yang Y., Hu Z. (2016) Calibration and correction of LA-ICP-MS and LA-MC-ICP-MS analyses for element contents and isotopic ratios. *Solid Earth Sciences*, Vol. 1, No. 1, pp. 5–27, http://dx.doi.org/10.1016/j.sesci.2016.04.002

Mychaluk K. (1995) The Yogo sapphire deposit. *G&G*, Vol. 31, No. 1, pp. 28–41, http://dx.doi.org/10.5741/GEMS.31.1.28

Pardieu V., Vertriest W. (2016) Gem News International: Update on colored gemstone mining in Tanzania. *G&G*, Vol. 52, No. 3, pp. 318–321.

Pearce N.J.G., Perkins W.T., Westgate J.A., Gorton M.P., Jackson S.E., Neal C.R., Chenery S.P. (1997) A compilation of new and published major and trace element data for NIST SRM 610 and NIST SRM 612 glass reference materials. *Geostandards and Geoanalytical Research*, Vol. 21, No. 1, pp. 115–144, http://dx.doi.org/10.1111/j.1751-908X.1997.tb00538.x

Peucat J., Ruffault P., Fritsch E., Bouhnik-Le Coz M., Simonet C., Lasnier B. (2007) Ga/Mg ratio as a new geochemical tool to differentiate magmatic from metamorphic blue sapphires. *Lithos*, Vol. 98, No. 1-4, pp. 261–274, http://dx.doi.org/10.1016/j.lithos.2007.05.001

Peretti A., Günther D. (2002) The color enhancement of fancy sapphires with a new heat-treatment technique (Part A). *Contributions to Gemology*, No. 1, pp. 1–48.

Peretti A., Günther D., Graber A.L. (2003) The beryllium treatment of fancy sapphires with a new heat-treatment technique (Part B). *Contributions to Gemology*, No. 2, pp. 21–34.

Ryssel H., Ruge I. (1986) *Ion Implantation*. John Wiley & Sons, New York.

Shen A.H. (2010) Silicon in sapphires – Its role and detectability by LA-ICP-QMS. *Goldschmidt Conference Abstracts*, p. A945.

Strasheim A., Brandt M.P. (1967) A quantitative X-ray fluorescence method of analysis for geological samples using a correction technique for the matrix effects. *Spectrochimica Acta Part B*, Vol. 23, No. 3, pp. 183–196, http://dx.doi.org/10.1016/0584-8547(67)80014-4

Sutherland F.L., Zaw K., Meffre S., Yui T.F., Thu K. (2015) Advances in trace element "fingerprinting" of gem corundum, ruby and sapphire, Mogok area, Myanmar. *Minerals*, Vol. 5, No. 1, pp. 61–79, http://dx.doi.org/10.3390/min5010061

Sylvester P.J. (2008) Chapter 5: Matrix Effects in Laser Ablation-ICP-MS. *Mineralogical Association of Canada Short Course Series*, Vol. 40, Vancouver, B.C., pp. 67–78.

Verma H.R. (2007) *Atomic and Nuclear Analytical Methods*. Springer, Berlin.

Wang W, Hall M., Shen A.H., Breeding C.M (2006) Developing corundum standards for LA-ICP-MS trace-element analysis. *G&G*, Vol. 42, No. 3, pp. 105–106.

Real-Time Microradiography of Pearls: A Comparison Between Detectors

Stefanos Karampelas, Abeer Tawfeeq Al-Alawi, and Ali Al-Attawi

Over the past ten years, gemological laboratories have been replacing film-based microradiography with real-time X-ray microradiography (RTX). This paper compares the output quality and resolution provided by two RTX units fitted with different detectors: an image intensifier (II) and a flat panel detector (FPD) using the same type of X-ray generating tube. Although the II is faster and less expensive, the images acquired with the FPD show greater detail of the pearl's internal growth structures, making interpretation and consequent conclusions easier to validate.

Since the early 20th century, gemological laboratories have been using film-based microradiography to reveal minute structures that separate natural from cultured pearls, sometimes alongside other methods such as Laue diffraction and endoscopy (e.g., Galibourg and Ryziger, 1927; Anderson, 1932; Alexander, 1941; Webster, 1954; Farn, 1980; Hänni, 1983; Poirot and Gonthier, 1998; Scarratt et al., 2000; Sturman, 2009). Today, real-time X-ray microradiography (RTX) is the foremost testing method for carrying out this vital work. It can also be paired with the more time-consuming X-ray computed microtomography for challenging identifications and research purposes (Karampelas et al., 2010; Krzemnicki et al., 2010).

With film-based microradiography, pearls are sometimes placed in direct contact with a high-resolution film cassette or immersed in a scatter-reducing liquid (e.g., lead nitrate solution or carbon tetrachloride, both of which are hazardous). X-ray scattering may also be reduced by simply surrounding individual pearls with a thin lead sheet or film. Regardless of the technique, a darkroom and a series of chemicals are necessary for film processing. It takes approximately 20 minutes to select the film and secure the pearls to the film cassette. At the same time, the exposure must be determined assuming an average-sized sample and keeping in mind that pearls in a strand are often graduated in size and that spheres require longer exposure times through the centers than the edges. Next, the film must be developed, fixed, and dried. All told, it is a time-consuming process.

The last 20 years have seen RTX steadily replace film-based radiography in the medical sector, and over the last decade most gemological laboratories have followed this trend by partially or fully adopting RTX. This method has several important advantages. No hazardous liquids are needed, and it gives immediate or nearly immediate results, which are easier to store and share among a team of technicians or in publications and presentations. RTX microradiography also requires a lower total amount of radiation than film-based microradiography, though similar X-ray generating tubes may be used without a need to reduce X-ray scattering. Some gemological laboratories initially employed RTX units with image intensifier (II) technology generally associated with digital cameras to acquire RTX microradiographs. More recent units have employed flat panel detectors (FPD), which can be of larger dimension with high resolution. However, FPD costs approximately US$25,000, about 40% more than II units and cameras.

An II is a vacuum tube device that converts invisible X-rays transmitted through the sample into visible light by a cesium iodide (CsI) scintillator. The visible light is then converted into electrons at the photoelectric surface and emitted inside the vacuum tube. The emitted electrons are accelerated and focused by electrodes, which act as an electron lens, onto the output screen and converted into bright visible light that is captured by a digital camera (figure 1, left; Ide et al., 2015). On the other hand, an FPD is a thin, flat solid sensor where invisible X-rays transmitted through the sample are converted into visible light, also by a CsI scintillator. The visible light is

See end of article for About the Authors and Acknowledgments.
Gems & Gemology, Vol. 53, No. 4, pp. 452–456,
http://dx.doi.org/10.5741/GEMS.53.4.452

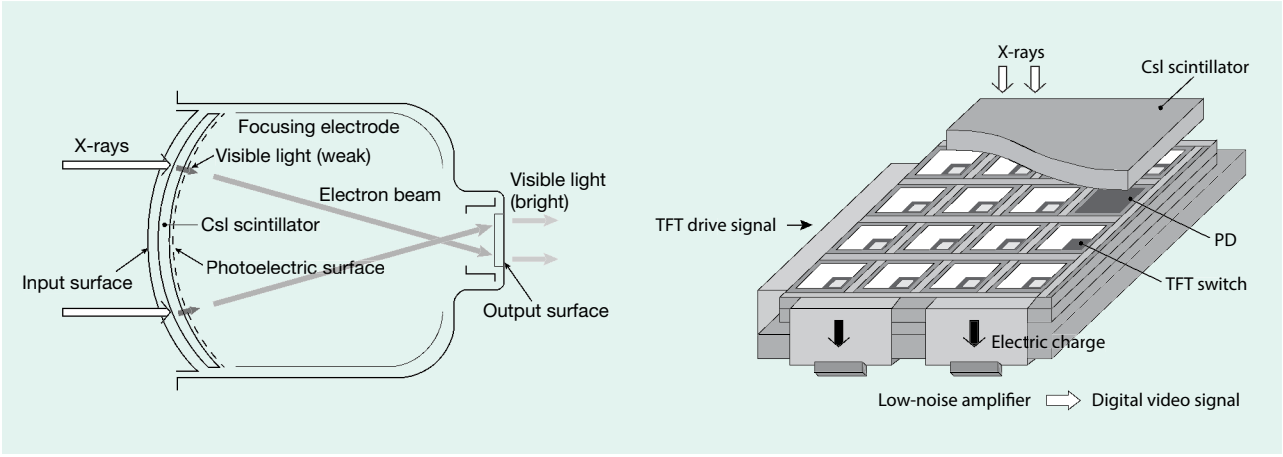

Figure 1. Structures and principles of operation for an II (left) and an FPD (right). Modified after Ide et al. (2015).

converted into an electric charge stored in each photodiode (PD). The signals are read by a thin-film transistor (TFT) switch provided for each pixel and amplified by a low-noise amplifier, undergoing analog-digital conversion to become digital video signals (figure 1, right; Ide et al., 2015).

The quality of the RTX microradiographs depends on the system's resolution (usually given in line pairs per millimeter, or LP/mm), the magnification, and the exported image size. The images are processed and initially viewed with software linked to the instrument or, more commonly, third-party software such as Fiji (ImageJ) or Adobe Photoshop. To view the microradiographs, a relatively large high-resolution screen (>20 inch) should be used. For this study, RTX microradiographs were acquired for the same set of samples (figure 2 and table 1) using the two different systems described above.

MATERIALS AND METHODS

Two undrilled and two drilled samples of various sizes from different mollusks were selected for this study (figure 2 and table 1): one natural saltwater pearl, one bead-cultured saltwater pearl, one non-bead-cultured freshwater pearl, and one non-bead-cultured saltwater pearl.

Microradiographs were acquired at the Bahrain Institute for Pearls and Gemstones (DANAT) using two RTX units: a FocalSpot (San Diego, California) Verifier HR FSX-090 and a Pacific X-Ray Imaging (PXI, San Diego, California) GenX-90. The electronics and imaging systems of both units were provided by PXI. Microradiographic images were collected in the same direction for each sample. Both instruments have the same tube type, a Thermo Scientific PXS5-928 with a spot size of <9 microns. The FocalSpot unit has a Toshiba E5877J-P1 image intensifier (two-inch and

Figure 2. The four samples from this study. Left to right: three cultured pearls (sample numbers 19, 21, and 8) and a natural pearl (sample number 1). The largest sample is 15.65 mm tall. Photo by Ghadeer Abdali, © DANAT.

TABLE 1. General characteristics of saltwater pearl samples.

Sample no.	Type	Mollusk	Size	Shape
1	Natural saltwater	*Pinctada radiata*	5.69–5.75 × 5.00 mm	Button[a]
8	Bead-cultured saltwater	*Pinctada fucata*	5.14 × 5.23 × 5.50 mm	Oval[b]
19	Non-bead-cultured saltwater	*Pinctada maxima*	11.63 × 12.37 × 15.65 mm	Baroque[a]
21	Non-bead-cultured freshwater	*Hyriopsis* species	10.29–10.86 mm	Near-round[b]

[a]*Undrilled*
[b]*Drilled*

four-inch options) with >40 LP/mm resolution at high magnification and a camera with 0.5 MB resolution. Due to the instrument's size and the X-ray tube collimator to minimize distortion, the maximum sensitive area is 33 × 33 mm^2 (with some areas at the corners not active, as an II initial field of view is round). The PXI unit has a Perkin Elmer Dexela 1512 flat panel detector with >40 LP/mm resolution at high magnification, a pixel size of 75 microns, 3072 × 1944 resolution, and a sensitive area of 33 × 33 mm^2, reduced from 49 × 56 mm^2 due to the X-ray tube filter.

In Brief

- Most gemological laboratories have been replacing film radiography with real-time X-ray microradiography (RTX) to separate natural and cultured pearls.
- A comparison of RTX units with image intensifier (II) and flat panel detector (FPD) technology shows that the first is more economical and produces faster results.
- An FPD yields images with less noise and greater detail of a pearl's internal structures, making it more suitable for their characterization.

The maximum frame averaging used to decrease noise was 256 frames for the II and 128 frames for the FPD. X-radiation of 70–90 kV accelerating voltage and 70–90 µA current were used in both instruments with an exposure time of 100–250 milliseconds per frame. The acquisition times for each microradiographic image were approximately 10 seconds for the II and 100 seconds for the FPD. The images were exported as TIF files, with a maximum resolution of 300 KB/8-bit grayscale and 6 MB/16-bit grayscale, respectively. For each sample, microradiographs were taken from three directions perpendicular to each other. The images were manipulated with Fiji (ImageJ) version 1.0 using Java 6, an open-source software.

RESULTS AND DISCUSSIONS

Selected radiographs of all four samples are shown in figures 3–6. Microradiographs acquired with the FPD are provided on the left, while images collected using the II system are on the right. All images are grayscale; lighter tones indicate materials with higher density such as calcium carbonate (usually aragonite for most gem-quality pearls, as in this study), while darker tones represent lower-density materials (usually organic matter, cracks, or cavities/voids). To view

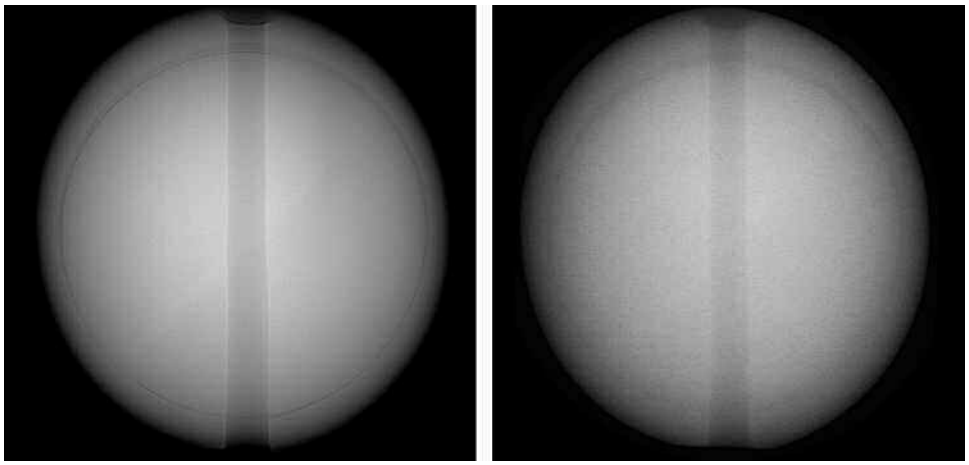

Figure 3. Microradiographs of sample 8, a bead-cultured saltwater pearl from Pinctada fucata, *produced with an FPD (left) and an II (right). The diameter of the bead is about 4.5 mm.*

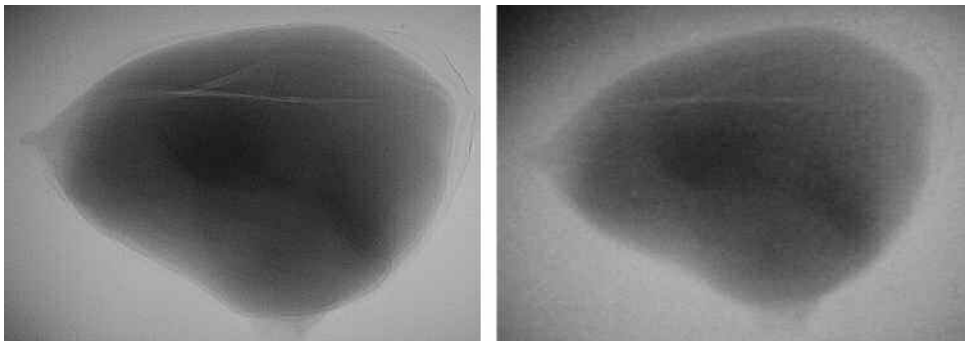

Figure 4. Microradiographs of the center of sample 19 (a non-bead-cultured saltwater pearl from Pinctada maxima*), produced with an FPD (left) and an II (right); fields of view approximately 7 mm.*

the raw original images, visit www.gia.edu/gems-gemology/winter-2017-microradiography-pearls and see supplementary items S3–S6. Figure 3 presents the microradiographs of a bead-cultured saltwater pearl from *Pinctada fucata*. The implanted bead, which presents no structure and is almost centered, is clearly indicated by a dark growth line running inside the edge of the sample and roughly parallel with this edge in both microradiographs. This line, made up mostly of organic material, separates the bead from the nacre overgrowth (Scarratt et al., 2000). The microradiographs acquired with an II appear less clear than those produced with the FPD, which allow the growth line surrounding the bead to be clearly viewed. This feature appears less clear in the II along several parts of the growth line.

Figure 4 presents the magnified microradiographs of the central part of a non-bead-cultured saltwater pearl from *Pinctada maxima*. A large irregular dark gray area that allows this sample to be identified is clearly observed in both microradiographs (Krzemnicki et al., 2010). However, the microradiograph acquired with an FPD reveals additional information in the form of light lines within the dark gray center and growth lines around it.

Figure 5 presents magnified microradiographs of the central part of a natural saltwater pearl from *Pinctada radiata*. Both images reveal an "onion-like" structure with a darker color and a dark spot in the center, a characteristic of natural pearls (Scarratt et al., 2000; Karampelas et al., 2010; Krzemnicki et al., 2010). Additionally, some dark areas and lines are observed toward the outer part of the sample. In the microradiograph acquired with the II, the dark center and the various growth lines are barely visible. It is very noisy, and thus further information cannot be revealed. In the microradiograph produced with an FPD, several additional lines are observed as well as some radial structures in the darker part of the sample. These structures, which likely result from the radial calcite, appear darker due to the enrichment of organic matter that is observed in the center of some natural pearls (Krzemnicki et al., 2010).

In figure 6, ring-like growth structures are recorded in the microradiographs acquired with FPD, as well as a weak, elaborate dark gray area in the center that represents a likely "twisted" cavity-related structure observed in some non-bead freshwater cultured pearls (Scarratt et al., 2000; Sturman, 2009). In the microradiographs acquired with II, fewer and less distinct

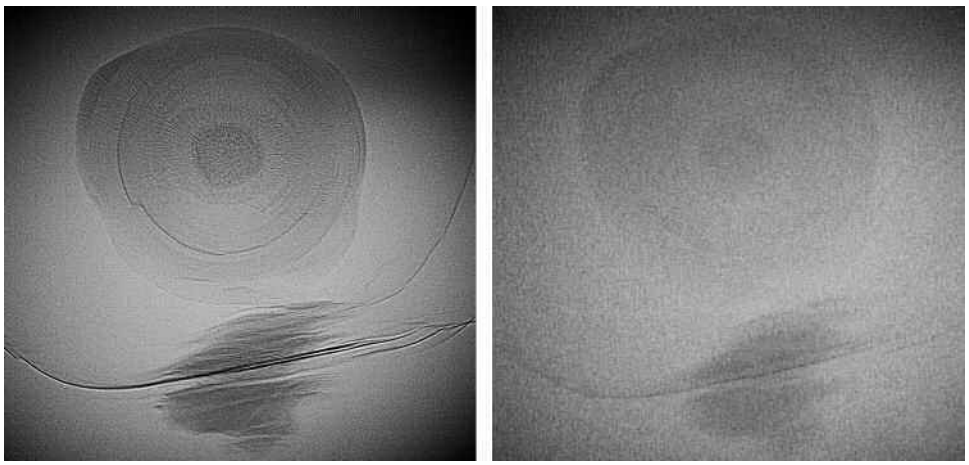

Figure 5. Microradiographs of sample 1 (a natural saltwater pearl from Pinctada radiata*), produced with an FPD (left) and an II (right); fields of view approximately 3.5 mm.*

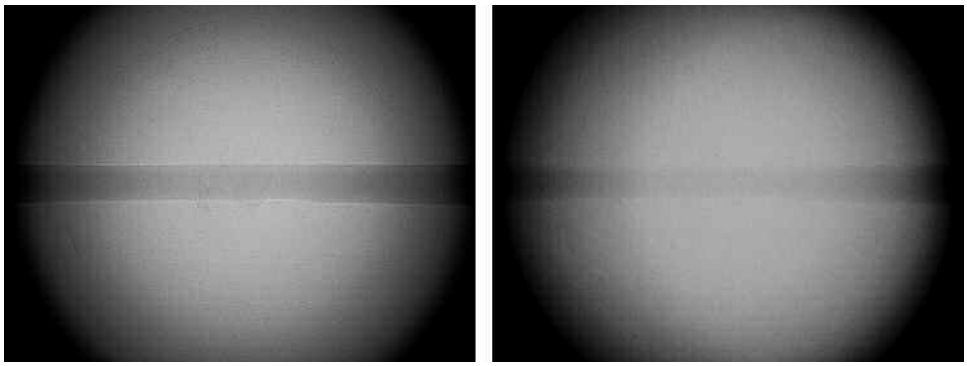

Figure 6. Microradiographs of sample 21 (a non-bead-cultured freshwater pearl from Hyriopsis *species), produced with an FPD (left) and an II (right); fields of view approximately 9 mm.*

growth structures are observed and in the center only a "hair-like" line is barely recorded. Generally, microradiographs of our samples acquired with an II give less distinct images with more noise than those acquired with an FPD; this observation is consistent with previous publications (Baba et al., 2002, 2004).

CONCLUSIONS

RTX microradiography is widely used today by gemological laboratories to separate natural and cultured pearls. Both II and FPD detectors are used for this purpose. An II detector produces faster results than an FPD, and at present the overall cost of an II-based unit is less. On the other hand, FPD images are less noisy and provide greater detail of the internal structures in both natural and cultured pearls, making them more suitable for pearl identification. However, an II could be appropriate for other industries, where the balance between cost and performance is important or when quick response is essential.

ABOUT THE AUTHORS

Dr. Karampelas (stefanos.karampelas@danat.bh) is research director, Ms. Al-Alawi is executive director, and Mr. Al-Attawi is pearl testing manager at the Bahrain Institute of Pearls and Gemstones (DANAT), based in Manama.

ACKNOWLEDGMENTS

The authors thank the gemological team of DANAT for their help with the microradiographs and macro image acquisition. John Donaldson from Pacific X-Ray (PXI) is thanked for the numerous fruitful discussions regarding the specifications sheets of each instrument.

REFERENCES

Alexander A.E. (1941) Natural and cultured pearl differentiation. *G&G*, Vol. 3, No. 12, pp. 184–188.

Anderson B.W. (1932) The use of X-rays in the study of pearls. *The British Journal of Radiology*, Vol. 5, No. 49, pp. 57–64, http://dx.doi.org/10.1259/0007-1285-5-49-57

Baba E., Konno Y., Ueda K., Ikeda S. (2002) Comparison of flat-panel detector and image intensifier detector for cone-beam CT. *Computerized Medical Imaging and Graphics*, Vol. 26, No. 3, pp. 153–158, http://dx.doi.org/10.1016/S0895-6111(02)00008-3

Baba E., Ueda K., Okabe M. (2004) Using a flat-panel detector in high resolution cone beam CT for dental imaging. *Dentomaxillofacial Radiology*, Vol. 33, No. 5, pp. 285–290, http://dx.doi.org/10.1259/dmfr/87440549

Farn A.E. (1980) Notes from the laboratory. *Journal of Gemmology*, Vol. 17, No. 4, pp. 223–229.

Galibourg J., Ryziger F. (1927) Les méthodes d'examen et d'étude des perles fines et des perles de culture. *Revue d'Optique Théorique et Instrumentale*, Vol. 3, pp. 97–133.

Hänni H.A. (1983) The influence of the internal structure of pearls on Lauegrams. *Journal of Gemmology*, Vol. 18, No. 5, pp. 386–400, http://dx.doi.org/10.15506/JoG.1983.18.5.386

Ide H., Yamamoto T., Onihashi H. (2015) X-ray devices contributing to sophistication of X-ray diagnostic systems. *Toshiba Review Edition*, Vol. 1, No. 1, pp. 39–44.

Karampelas S., Michel J., Zheng-Cui M., Schwarz J.-O., Enzmann F., Fritsch E., Leu L., Krzemnicki M.S. (2010) X-ray computed microtomography applied to pearls: Methodology, advantages, and limitations. *G&G*, Vol. 46, No. 2, pp. 122–127, http://dx.doi.org/10.5741/GEMS.46.2.122

Krzemnicki M., Friess D., Chalus P., Hänni H.A., Karampelas S. (2010) X-ray computed microtomography: Distinguishing natural pearls from beaded and non-beaded cultured pearls. *G&G*, Vol. 46, No. 2, pp. 128–134, http://dx.doi.org/10.5741/GEMS.46.2.128

Poirot J.P., Gonthier E. (1998) Le contrôle des perles à partir de 1929 au Laboratoire Gemmologique Français (du laboratoire syndical au laboratoire C.C.I.P.). *Revue de Gemmologie a.f.g.*, Vol. 133, pp. 26–27.

Scarratt K., Moses T.M., Akamatsu S. (2000) Characteristics of nuclei in Chinese freshwater cultured pearls. *G&G*, Vol. 36, No. 2, pp. 98–109, http://dx.doi.org/10.5741/GEMS.36.2.98

Sturman N. (2009) The microradiographic structures on non-bead cultured pearls. www.giathai.net/pdf/The_Microradiographic_structures_in_NBCP.pdf, Nov. 21 [date accessed: Jul. 8, 2017].

Webster R. (1954) Some unusual structures in pearls and cultured pearls. *Journal of Gemmology*, Vol. 4, No. 8, pp. 325–334, http://dx.doi.org/10.15506/JoG.1954.4.8.325

CHARTS

Inclusions in Natural, Synthetic, and Treated Ruby

Nathan D. Renfro, John I. Koivula, Jonathan Muyal, Shane F. McClure, Kevin Schumacher, and James E. Shigley

Figure 1. These rubies, a 16.68 mm rough and a 2.72 ct cushion cut, are from Myanmar. Photo by Robert Weldon/GIA, courtesy of the William F. Larson collection.

Following the charts for the micro-features of emerald and sapphire—published in Winter 2016 and Summer 2017, respectively—this chart on ruby rounds out *G&G*'s series on inclusions in the "Big Three" colored stones. Rubies (figure 1) have long been one of the top gems in the trade, commanding premium prices. Historically, their popularity has been critical to the development of color and clarity treatments (including heating and dyeing, and now more recently introduced processes) and synthetic gems. In the early 1900s, over five million carats of synthetic ruby were produced annually by the flame-fusion, or Verneuil, method (Hughes, 2017).

Innovative new treatments have also played a major role in satisfying the continued demand for ruby. In the early 1990s, gemological laboratories saw the introduction of chromium-diffused rubies (McClure et al., 1993). In the early 2000s, lead-glass filling of low-quality rubies reached international markets and became one of the most widespread—and most

See end of article for About the Authors.
Gems & Gemology, Vol. 53, No. 4, pp. 457–458,
http://dx.doi.org/10.5741/GEMS.53.4.457

problematic—treatments in the gem trade (McClure et al., 2006). Also encountered in the early 2000s was beryllium diffusion of ruby, which made it possible to produce pleasing red colors from stones with strong brown or dark tones that would not respond to traditional heat treatment (Emmett et al., 2003). Rubies from Songea, Tanzania, for example, were dramatically improved with beryllium diffusion.

Demand has also been met by several new ruby deposits in the last decade. Mozambique has become the leading producer of gem-quality rubies since the discovery in Montepuez in 2009. More than two million carats of rough from Mozambique were offered at the first Gemfields rough ruby auction in 2014 (Lucas and Pardieu, 2014).

The photomicrographs chosen for this chart represent a wide range of features one might encounter in natural, treated, and synthetic rubies when examining them with a gemological microscope. Some features are common, while others are exceedingly rare. However, all of the images presented provide the viewer with a tremendous amount of information about the unique micro-world of rubies. For more on ruby and its inclusions, see our suggested reading list (http://www.gia.edu/gems-gemology/winter-2017-suggested-reading-ruby-chart).

ABOUT THE AUTHORS

Mr. Renfro is manager of colored stones identification, and John Koivula is analytical microscopist, at GIA in Carlsbad, California. Mr. Muyal is a staff gemologist, Mr. McClure is global director of colored stone services, Mr. Schumacher is a photo and video photo producer for Gems & Gemology, and Dr. Shigley is distinguished research fellow at GIA in Carlsbad.

REFERENCES

Emmett J.L., Scarratt K., McClure S.F., Moses T., Douthit T.R., Hughes R., Novak S., Shigley J.E., Wang W., Bordelon O., Kane R.E. (2003) Beryllium diffusion of ruby and sapphire. *G&G*, Vol. 39, No. 2, pp. 84–135, http://dx.doi.org/10.5741/GEMS.39.2.84

Hughes R.W., with W. Manorotkul and E.B. Hughes (2017) *Ruby and Sapphire: A Gemologist's Guide*. RWH Publishing, Bangkok.

Lucas A., Pardieu V. (2014) Gemfields inaugural rough ruby auction in Singapore. *GIA Research News,* Jul. 17, www.gia.edu/gia-news-research-gemfields-ruby-auction-singapore

McClure S.F., Kammerling R.C., Fritsch E. (1993) Update on diffusion-treated corundum: Red and other colors. *G&G*, Vol. 29, No. 1, pp. 16–28, http://dx.doi.org/10.5741/GEMS.29.1.16

McClure S.F., Smith C.P., Wang W., Hall M. (2006) Identification and durability of lead glass–filled rubies. *G&G*, Vol. 42, No. 1, pp. 22–34, http://dx.doi.org/10.5741/GEMS.42.1.22

Additional Reading

For a list of references pertaining to inclusions in natural, synthetic, and treated ruby, go to www.gia.edu/gems-gemology/winter-2017-suggested-reading-ruby-chart or scan the QR code to the right.

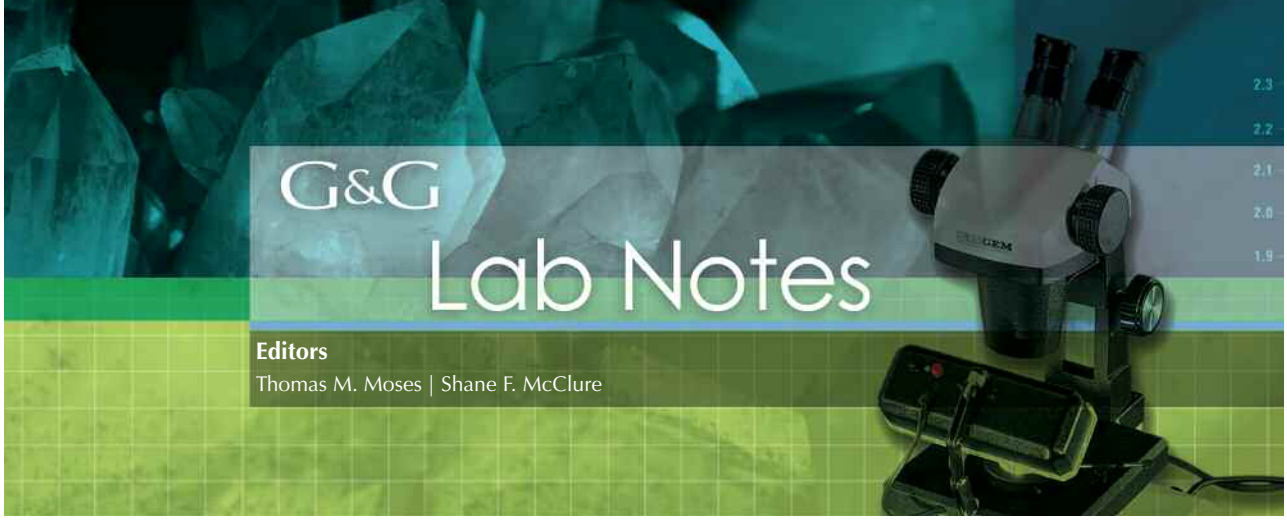

Cat's-Eye ALEXANDRITE with Unique Inclusion Pattern

Chatoyancy is an optical effect caused by light reflecting off dense concentrations of parallel needles or hollow tubes in cabochon-cut gem materials. To maximize chatoyancy, the base of the cabochon should be cut parallel to the inclusions to produce an even effect across the dome. In some cases, the parallel inclusions are not distributed throughout the stone and are only in zones or narrow bands. In such cases the cutter must orient the needles with care to produce a cat's-eye.

A chatoyant cabochon, weighing 21.22 ct and measuring 17.75 × 17.50 × 6.77 mm, was recently submitted to GIA's Tokyo laboratory for identification service. This stone displayed a change of color (figure 1) from brownish green in fluorescent light to brownish purple in incandescent light. Standard gemological testing resulted in a spot refractive index (RI) reading of 1.75, a specific gravity (SG) of 3.74, and strong trichroism. In addition to these properties, heterogeneous needle-like inclusions and infrared and Raman spectroscopy revealed that the stone was natural chrysoberyl.

What is notable about this stone is that all the needle-like inclusions that cause the chatoyancy are confined to a narrow layer at the very bottom of the cabochon (figure 2). The rest of the stone is nearly free of inclusions. The cutter obviously knew to orient what must have been a narrow layer of needles at the bottom of the cabochon so that the dome would form a complete cat's-eye. Some synthetic or imitation stones have an engraved foil backing or an engraved base to produce a cat's-eye or star in much the same way. Raman spectroscopic analysis indicated that the needle-like inclusions were rutile (figure 3). While the boundary between the included and

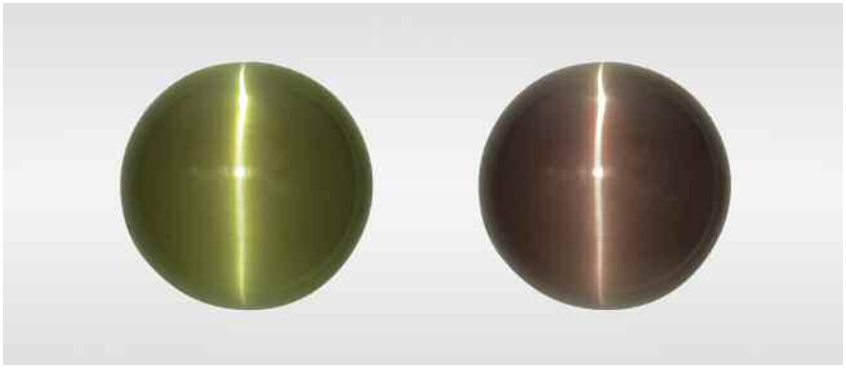

Figure 1. This alexandrite cabochon appears brownish green in fluorescent light (left) and brownish purple in incandescent light (right). The cabochon shows chatoyancy under both forms of illumination due to light reflection from the shallow plane of dense fine parallel needles.

Figure 2. A side view of the cabochon, immersed in water, showing the localized inclusions near the base. Field of view 1.6 cm.

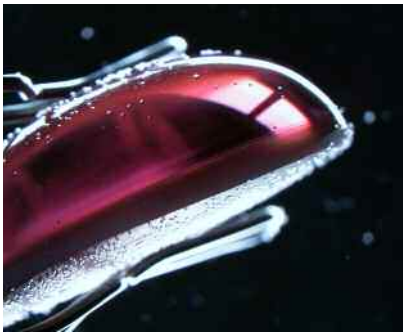

Figure 3. Iridescent minute parallel needles and particles in the alexandrite cabochon. Field of view 2.0 mm.

Editors' note: All items were written by staff members of GIA laboratories.

GEMS & GEMOLOGY, Vol. 53, No. 4, pp. 459–464.

Figure 4. A 2.67 ct oval-cut diamond with uneven "lizard skin" surface texture. Close-up views of the pavilion with reflected light show how the textured pattern continues across facet junctions. Fields of view 3.56 mm (center) and 1.29 mm (right).

inclusion-free areas looks sharp, the stone is not assembled.

Makoto Miura and Yusuke Katsurada

Lizard Skin on Deformed DIAMOND

Facets that are nearly parallel to a diamond's octahedral crystal plane often develop a wavy, rippled appearance called "lizard skin" during polishing (e.g., J.I. Koivula, *The MicroWorld of Diamonds*, Gemworld International, Northbrook, Illinois, 2000, p. 63). The term is also used more broadly to describe any bumpy, uneven surface texture that develops on polished diamond facets. It is often attributed to polishing off-grain. Recently, GIA's New York lab encountered a 2.67 ct type IIa diamond (figure 4, left) with especially prominent lizard skin texture on multiple facets (figure 4, center and right). In this case, the texture appears to have developed due to a preexisting deformation fabric or structure inherent to the diamond itself, rather than merely as a consequence of poor polishing technique.

The surface texture has a pattern to it, with small bumps appearing to line up in corridors. Some corridors clearly continue from one facet to the next (figure 4, right). The continuity across facets suggests that this texture is the surface expression of irregularities that actually extend into the volume of the diamond itself. At high magnification with crossed polarizing filters, the lizard skin can be seen to conform to the shape and texture of the strain pattern within the diamond—that is, the pattern of bumps and depressions matches up where the intricate internal dark/light pattern of tatami birefringence meets the polished surface. This connection supports the idea that the surface texture is a reflection of underlying crystal imperfections.

Unusual hydrogen- and methane-bearing metallic inclusions in this diamond suggest it originated from extreme depths of about 360–750 km in the earth's mantle (E.M. Smith et al., "Large gem diamonds from metallic liquid in Earth's deep mantle," *Science*, Vol. 354, No. 6318, 2016, pp. 1403–1405). In this high-temperature environment, deformation and annealing over a long period of time may have given the diamond a mosaic crystal structure. This natural phenomenon occurs when heat allows the crystal to undergo recovery, a process of dislocation reorganization that divides the distorted grain into a mosaic of smaller, undistorted subgrains without new crystal growth. The subgrains, measuring about 10–30 microns, are like bricks in a wall; while the wall may be slightly curved, the individual bricks are not distorted. These distortions become localized as subgrain boundaries rather than spreading continuously through the crystal. As a result, the subgrains will be oriented in slightly different directions.

Because polishing is so strongly dependent on crystal orientation, if a single facet consists of a mosaic of subgrains with varying orientation, polishing will be uneven. The resulting surface may develop a pattern of bumps and depressions that mimics the size and shape of underlying subgrains and, in turn, reflects the diamond's natural deformation history. Samples like this one are interesting for scientists because little is known about the geological conditions that lead to the various deformation-related features seen in natural diamonds.

Evan M. Smith and Paul Johnson

Gota de Aceite in a Zambian EMERALD

Gota de aceite (Spanish for "drop of oil"), a rare phenomenon that occurs in the finest emeralds, is typically associated with Colombian origin (R. Ringsrud, "*Gota de aceite*: Nomenclature for the finest Colombian emeralds," Fall 2008 *G&G*, pp. 242–245). The phenomenon creates a roiled effect caused by irregularity in the emerald's internal crystal structure. During the gemstone's crystallization the growth conditions are altered, giving rise to rapid columnar growth. When looking down the emerald's c-axis, the outline of the columns can be seen. This sometimes has the appearance of drops of oil, giving rise to the name. The columns typically have a slightly different trace element composition from that of the host emerald. This heterogeneity in trace element chemistry will cause a minor change in the refractive

index of the columns, allowing the structure to be visible.

The Carlsbad laboratory recently received a 2.10 ct emerald for origin determination. The stone had blocky multiphase inclusions and ilmenite scattered throughout, along with mica platelets and a very subtle blue flash effect associated with some small feathers. At a certain angle, a muted gota de aceite effect was also visible (figure 5). The UV-Vis spectrum shows a distinct Fe^{2+} broad band at approximately 900 nm. Inductively coupled plasma–mass spectrometry (ICP-MS) confirmed the stone's relatively high iron content and indicated a chemical composition consistent with Zambian origin.

The gota de aceite seen in this Zambian emerald was not exactly the same as the phenomenon found in Colombian emeralds. Dendritic ilmenite, an iron-rich mineral, was fully enclosed in the columnar structure. We believe the epigenetic ilmenite exsolved the increased iron content, as Zambian emeralds contain a larger amount of iron than their Colombian counterparts (J.C. Zwaan et al., "Emeralds from the Kafubu area, Zambia," Summer 2005 *G&G*, pp. 116–148).

Until now, gota de aceite has only been documented in Colombian emeralds and has been an aid in origin determination. Still, this is not the first time that an inclusion indicative of a particular origin has been found elsewhere. Jagged three-phase inclusions, traditionally seen in Colombian emeralds, have also been documented in emeralds from certain mines in Afghanistan, China, and Zambia (S. Saeseaw et al., "Three-phase inclusions in emerald and their impact on origin determination," Summer 2014 *G&G*, pp. 114–132). This emerald shows that inclusions may not always provide conclusive proof of origin, but they can still provide useful information.

Nicole Ahline

Figure 5. A muted gota de aceite *effect, with epigenetic ilmenite, in an emerald from Zambia. Field of view 1.26 mm.*

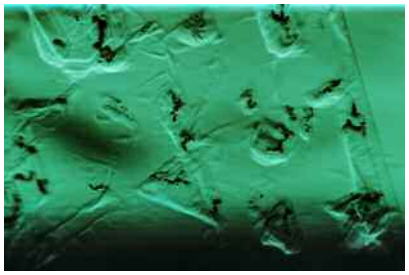

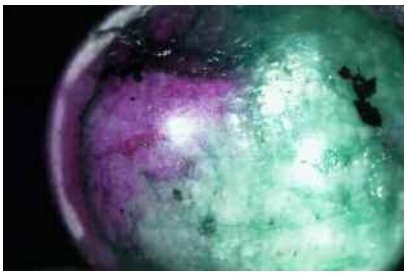

Figure 6. Green to dark green and pinkish purple to dark purple dye concentrations were observed in the fissures and structure of this quartzite, which resembled ruby-in-zoisite. Field of view 9.61 mm.

Dyed QUARTZITE Imitation of Ruby-in-Zoisite

The New York laboratory recently received a bracelet composed of translucent multicolored beads that closely resembled ruby-in-zoisite. Standard gemological testing of one of the round beads (measuring 8.33 × 8.17 mm) revealed an RI of 1.55 for both the purple and green areas (instead of approximately 1.76 or 1.69 for ruby and zoisite, respectively) and very weak red to inert fluorescence in long-wave and short-wave ultraviolet light, respectively. Microscopic observation revealed fissures and a translucent aggregated/grainy structure, both of which contained green to dark green and pinkish purple to dark purple dye concentrations (figure 6).

Although most of the translucent green and purple aggregate material we encounter for identification is ruby-in-zoisite, the gemological features of this bead were inconsistent with our expectations. Raman spectra were collected to confirm the identity. Spectra from both the purple and green areas matched quartz (figure 7). Since the material was an aggregate, we concluded that it was dyed quartzite.

The Lab Notes section has documented many cases of dyed quartzite

Figure 7. Raman spectra collected from the sample's purple and green areas indicated quartz rather than ruby and zoisite. Spectra are offset for clarity.

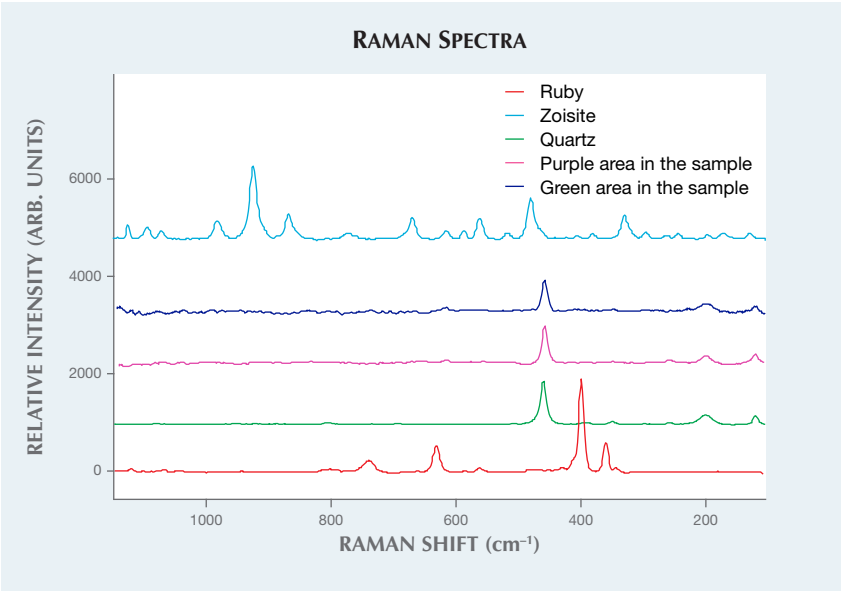

imitating jadeite, ruby, lapis lazuli, and sugilite (Spring 1986, pp. 49–50; Summer 1991, pp. 122–123; Summer 1995, pp. 125–126; Summer 1998, pp. 131–132; Spring 2001, pp. 62–63; and Fall 2003, pp. 219–220). But this is the first example we have seen of quartzite being used to imitate ruby-in-zoisite. This dyed quartzite provides an intriguing example for consumers to be aware of when purchasing ruby-in-zoisite.

HyeJin Jang-Green

SYNTHETIC MOISSANITE
Imitating Rough Diamond

The Carlsbad laboratory recently examined a very light green 9.71 ct specimen (figure 8), measuring 11.79 × 9.69 × 11.61 mm, that was submitted as a rough diamond. The sample resembled a diamond octahedron, with surface growth features and a bright vitreous to subadamantine luster. Closer examination of its habit and surface features, along with gemological and advanced testing results, revealed it to be a synthetic moissanite.

The specimen was not a true octahedron, as is typical of a diamond crystal, but a rectangular bipyramid with 10 faces (eight triangular and two hexagonal side pinacoids on the girdle). The surface was dimpled, and two of the faces had deep striations resembling growth features in a rough diamond. Irregularly shaped and sub-hexagonal etch pits (figure 9), along with some dark brown residue, were also found on the surface. Due to the uneven surface, observation of internal features was limited to some small scattered pinpoint inclusions and a few etch tubes (figure 10). The surface also made it difficult to see any doubling effect or a doubly refractive reaction in the polariscope. Viewed in plane-polarized light, however, a large twinning plane crossed the crystal diagonally, bluish green on one side and colorless on the other. This dichroism served as proof of the stone's doubly refractive nature, as opposed to singly refractive diamond. Standard gemological properties of the stone offered further evidence of its true identity, including an over-the-limit refractive index reading, a hydrostatic SG of 3.23, very weak yellow fluorescence in both long-wave and short-wave UV, and a uniaxial optic figure. These properties and advanced testing results, including Fourier-transform infrared (FTIR) and Raman spectrometry, identified the specimen as synthetic moissanite. It is important to note that although natural moissanite exists, it is extremely rare and gem-quality material has never been found. Natural moissanite commonly occurs in fragmented pieces and in much smaller sizes (the largest known specimen measured 4.1 mm), often with a creamy white or red matrix (Summer 2014 GNI, pp. 160–161). That was not the case for this 9.71 ct synthetic moissanite.

Gemological and advanced testing are indispensable tools for revealing the true identity of gems, especially simulants and imitations with an appearance that can easily deceive the general public. While there is no evidence that this specimen was deliberately deceptive,

Figure 8. A very light green 9.71 ct synthetic moissanite crystal, submitted to the Carlsbad laboratory as a rough diamond. Field of view approximately 14 mm.

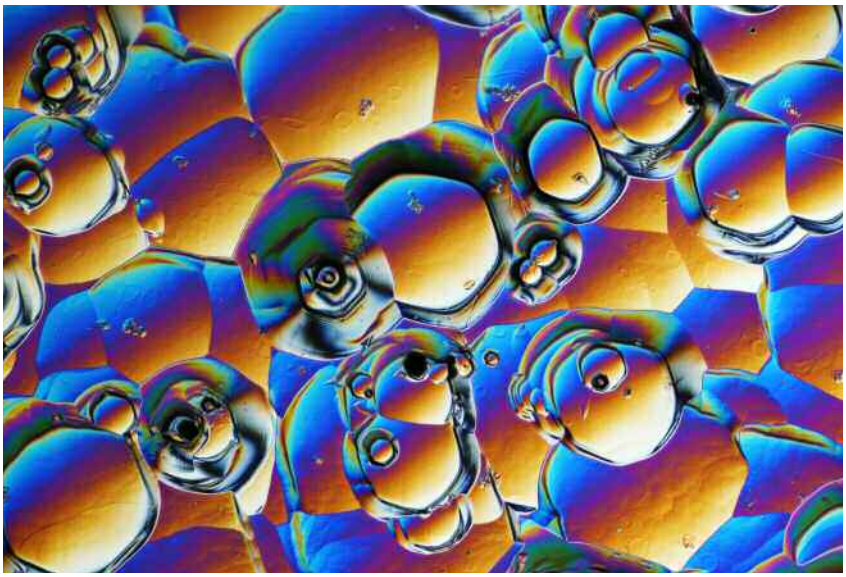

Figure 9. Sub-hexagonal etch pits in synthetic moissanite are observed using differential interference contrast. Field of view approximately 1.44 mm.

Figure 10. Etch tubes extended from surface etch pits and ended at the twinning plane. Field of view approximately 2.30 mm.

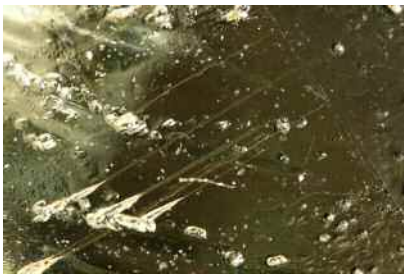

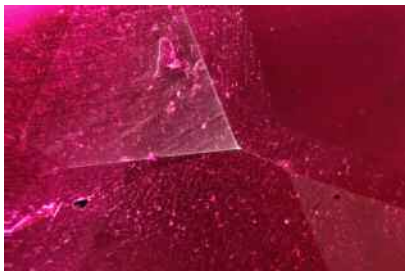

Figure 11. A thin layer of synthetic ruby overgrowth with flux particles is distinct from the natural sapphire seed visible in the upper right of the image. Field of view 1.99 mm.

TABLE 1. Trace elements in two synthetic ruby overgrowth samples, detected by LA-ICP-MS (avg. concentration in ppmw[a]).

Element	Concentration in overgrowth	Standard deviation
Cr	32,866	1342
Fe	1231	101.4
Ga	47.6	2.40
Mg	4.92	1.69
Mn	4.55	0.31
Mo	bdl[b]	—
Ni	34.9	49.5
Ti	19.06	6.94
Pt	4.03	4.07
Zr	0.41	0.71

[a] *Six spots examined in total.*
[b] *bdl: below detection limit. Detection limit was 0.013 ppmw for both samples.*

gemological knowledge is important in preventing accidental and intentional acts of fraud and preserving the integrity of the trade.

Rebecca Tsang

Two Unusual Natural Sapphires With SYNTHETIC RUBY Overgrowth

The New York laboratory recently received two loose red oval mixed cuts for identification. Standard gemological testing yielded refractive indices slightly higher than expected for corundum: 1.778–1.788 and 1.776–1.787, while a typical RI for corundum is 1.762–1.770. Elevated RIs for chromium-diffused corundum have been reported and may be attributed to higher Cr_2O_3 concentration at the surface (S.F. McClure et al., "Update on diffusion-treated corundum: Red and other colors," Spring 1993 *G&G*, pp. 16–28). To the unaided eye, the stones appeared to be chromium diffused, displaying red color concentration at the facet junctions, but their synthetic component became apparent upon further observation.

Microscopic examination revealed that planes of minute particles demarcated a thin layer, approximately 0.3 mm thick, of synthetic overgrowth from a natural sapphire core (figure 11). The presence of intact silk and heat-altered crystal inclusions confirmed the seeds to be natural (figure 12). A series of shallow flux-fingerprints cracking the surface suggested a flux growth process (figure 13). Portions of the near-colorless core could be seen in areas where the overgrowth was cut away during polishing (figure 14). These windows showed a sharp boundary without "bleeding" of the saturated red overgrowth into the near-colorless seed, which is typically observed in chromium-diffused corundum (McClure et al., 1993). The windows into the near-colorless seed also indicate that most or all of the red color is concentrated in the synthetic ruby overgrowth.

The overall appearance of the two stones was similar to the now-rare Lechleitner synthetic overgrowth

Figure 12. A fuzzy heat-altered crystal inclusion commonly referred to as a "snowball" is surrounded by a discoid fracture, proving the natural origin of the corundum seed. Field of view 1.26 mm.

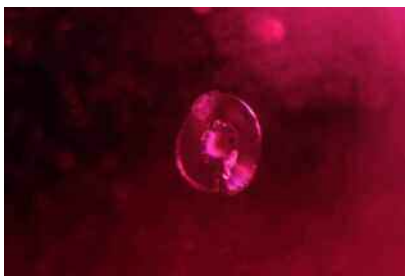

Figure 13. Reflective silk inclusions in the natural sapphire seed are visible behind a coarse flux fingerprint in the synthetic ruby overgrowth, which was cut through during the fashioning process. Field of view 3.57 mm.

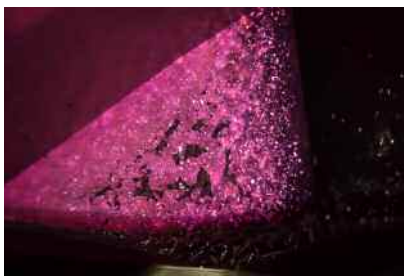

Figure 14. A portion of the near-colorless corundum seed is revealed in an area where the synthetic ruby overgrowth was cut away during fashioning. Field of view 10.85 mm.

Figure 15. A thin layer of synthetic emerald deposited on a near-colorless beryl seed, a type of synthetic emerald first marketed by Johann Lechleitner in the early 1960s. Field of view 3.57 mm.

emeralds, which are composed of a near-colorless beryl seed with synthetic emerald overgrowth. A sample with this type of synthetic emerald overgrowth was coincidentally submitted to the Carlsbad laboratory for identification around the same time (figure 15). In addition to emeralds, Lechleitner also experimented with ruby overgrowth on both synthetic and natural corundum seeds (K. Schmetzer and H. Bank, "Lechleitner synthetic rubies with natural seed and synthetic overgrowth," *Journal of Gemmology*, 1988, Vol. 21, No. 2, p. 95–101), with the most commonly documented versions containing synthetic seeds (E.J. Gübelin and J.I. Koivula*, Photoatlas of Inclusions in Gemstones,* Vol. 2, Opinio Verlag, Basel, Switzerland, 2005, p. 352; Fall 2014 Lab Notes, pp. 242–243).

Advanced testing on the synthetic ruby overgrowth layer using laser ablation–inductively coupled plasma–mass spectrometry (LA-ICP-MS) revealed the presence of Cr, Fe, Ga, Mn, Mg, Ni, Ti, Pt, and Zr (table 1). These results, specifically the presence of platinum, are consistent with previously reported synthetic ruby overgrowth (S. Saeseaw et al., "Analysis of synthetic ruby overgrowth on corundum," *GIA News from Research*, June 10, 2015). Molybdenum was reported in the primary examination of Lechleitner overgrowth rubies (Schmetzer and Bank, 1988), and its absence here suggests alternative growth conditions for these samples.

Although this is not the first report of synthetic ruby overgrowth on natural sapphire seeds (Schmetzer and Bank, 1988; C.P. Smith, "Diffusion ruby proves to be synthetic ruby overgrowth on natural corundum," Fall 2002 *G&G*, pp. 240–248), it marks the first time the New York and Carlsbad laboratories have had them submitted for identification. The resurfacing of these vintage overgrowth synthetics shows that once a material is in the trade, it is here to stay.

Tyler Smith and Hollie McBride

PHOTO CREDITS

1—Shunsuke Nagai; 2 and 3—Makoto Miura; 4—Evan Smith; 5—Nathan Renfro; 6—HyeJin Jang-Green; 8–10—Rebecca Tsang; 11–15—Hollie McBride.

THANK YOU, REVIEWERS

Gems & Gemology requires each manuscript submitted for publication to undergo a rigorous peer review process, in which a paper is evaluated by at least three experts in the field prior to acceptance. This is essential to the accuracy, integrity, and readability of *G&G* content. In addition to our dedicated Editorial Review Board, we extend many thanks to the following individuals who devoted their valuable time to reviewing manuscripts in 2017.

Non-Editorial Board Reviewers

Ilaria Adamo • Donald Burnett • Gagan Choudhary • Zachary Cole • Si and Ann Frazier • Dan Frost • Artitaya Homkrajae • Richard Hughes • Dorrit Jacob • John King • Maya Kopylova • Glenn Lehrer • Cigdem Lule • Carmel McDougall • Tetsuji Masaoka • Jana Miyahira-Smith • Lutz Nasdala • Laura Otter • Karl Schmetzer • Olivier Segura • Sherris Cottier Shank • Elena Shuchukina • Nicholas Sturman • Ziyin Sun • Rachelle Turnier • Chunhui Zhou

Cast Your Vote for the 2017 Dr. Edward J. Gübelin Most Valuable Article Award

Established in 1981, *G&G*'s Most Valuable Article Award invites the journal's readers to vote on the three most important articles (feature articles, field reports, and charts) from the previous year. Each completed ballot is entered into a drawing to win a one-year subscription to *Gems & Gemology*.

To qualify for the drawing, please submit your votes for the 2017 MVA Award by **Monday, March 12, 2018**, either by mail, by scanning the QR code, or by visiting www.gia.edu/most-valuable-article-2017

Aragonite Spheres in Ethiopian Opal

Recently, the authors examined an 88.51 ct pear-shaped white precious opal that displayed typical digit patterns and hydrophane behavior (see Fall 2013 Lab Notes, pp. 175–176). These properties were consistent with opal from the Wollo mining area in Ethiopia (see B. Rondeau et al., "Play-of-color opal from Wegel Tena, Wollo Province, Ethiopia," Summer 2010 *G&G*, pp. 90–105). The stone also showed weak whitish blue fluorescence in long-wave UV and was inert to short-wave UV. No phosphorescence was observed.

In addition to its attractive digit pattern with spectral play-of-color, this opal hosted a number of unusual inclusions: opaque black octahedrons and translucent spheres. When viewed with a fiber-optic light, the opaque black octahedrons appeared a dark brassy metallic yellow (figure 1). Raman analysis identified them as pyrite, which has been previously reported in Ethiopian opal (N. Renfro and S.F. McClure, "Dyed purple hydrophane opal," Winter 2011 *G&G*, pp. 260–270). Of particular interest is that the translucent spherical inclusions (figure 2), which formed as isolated spheres and clusters, were identified by Raman

Figure 1. This Ethiopian opal contained an interesting inclusion scene consisting of a string of octahedral pyrite crystals and aragonite spheres. Photomicrograph by Charuwan Khowpong; field of view 1.40 mm.

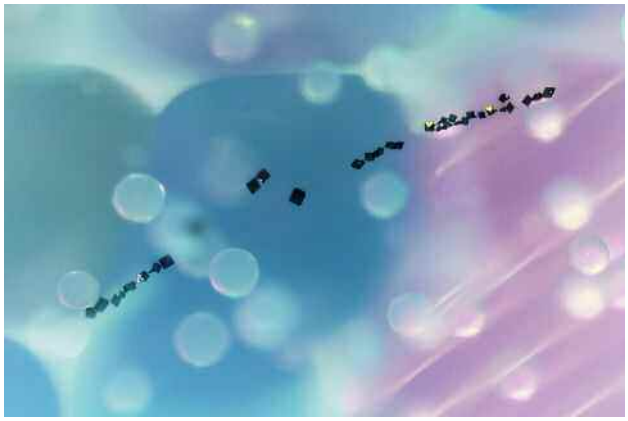

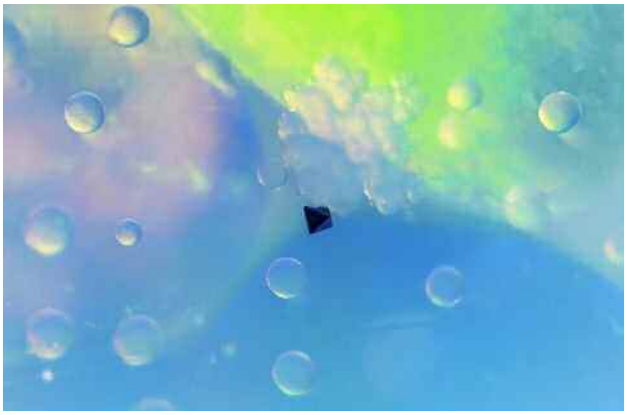

Figure 2. A single pyrite crystal is seen among spheres and clusters of translucent aragonite inclusions, both of which were identified by Raman spectroscopy. Oblique fiber-optic illumination. Photomicrograph by Charuwan Khowpong; field of view 1.05 mm.

About the banner: Modified Rheinberg illumination highlights the crystallographically aligned tension cracks in this topaz crystal. Photomicrograph by Nathan Renfro; field of view 10.29 mm. Specimen courtesy of John S. White. Editors' note: Interested contributors should contact Nathan Renfro at nrenfro@gia.edu and Jennifer-Lynn Archuleta at jennifer.archuleta@gia.edu for submission information.

Gems & Gemology, Vol. 53, No. 4, pp. 466–471.

analysis as aragonite. The presence of aragonite spheres in opal is quite uncommon and has not been previously reported in precious opal from Ethiopia.

Ratima Suthiyuth and Charuwan Khowpong
GIA, Bangkok

Remarkable Twinned Calcite Inclusion in Mogok Ruby

The Mogok Stone Tract in Myanmar (formerly Burma) is one of the world's most famous sources of ruby, which often forms there in a calcite-marble host. Calcite may occur as an inclusion inside the ruby, as in the example in figure 3. In this stone, the calcite is easy to spot between crossed polarizers, which reveal polysynthetic twinning planes that "crisscross" the crystal. While calcite is a common inclusion in ruby, this is the clearest example of calcite twinning this author has seen. Surrounding the calcite crystal is a dense, angular nest of exsolved rutile silk as short needles, a typical scene in rubies from this locality.

E. Billie Hughes
Lotus Gemology, Bangkok

Figure 3. Viewed between crossed polarizers, an included calcite crystal within an unheated Burmese ruby displays dramatic twinning planes. Photomicrograph by E. Billie Hughes; field of view 3.90 mm.

New Phenomenal Feldspar from North Carolina With Iridescent Inclusions

Several varieties of aventurescent feldspar are well known in the gem trade. Of these, one of the most remarkable is orthoclase from the Hart's Range area in Australia. This unique material showcases exsolution platelets of hematite and ilmenite that display thin-film interference colors along the interface between the exsolution product and the feldspar host. Because of its array of colors and the crosshatch pattern of exsolution platelets, the material's trade name is "rainbow lattice sunstone."

The authors recently examined samples of potassium feldspar from a relatively obscure source (figure 4) that displayed a phenomenon remarkably similar to Australian rainbow lattice sunstone. This new material is reported to be from the Statesville area of North Carolina and contains brown and black exsolution platelets of hematite and ilmenite showing thin-film interference colors along the interface with the host feldspar. This deposit was first reported by George Frederick Kunz (*Gems and Precious Stones of North America*, The Scientific Publishing Co., New York, 1890, p. 164). Chemical analysis of the feldspar was performed using laser ablation–inductively coupled plasma–mass spectrometry (LA-ICP-MS), and the results were consistent with potassium feldspar.

Local prospector Ryan Underwood first found samples of this material as loose crystal fragments and traced them back to their source rock, a metamorphic biotite gneiss. The crystals are brittle, apparently as a result of metamorphic stresses, and tend to cleave during cutting. As such, material suitable for cutting is rare and finished stones tend

Figure 4. Brown and black exsolution platelets of hematite and ilmenite in feldspar (left) show colorful thin-film interference colors in oblique fiber-optic illumination (right). Photomicrographs by Nathan Renfro; fields of view 3.55 mm.

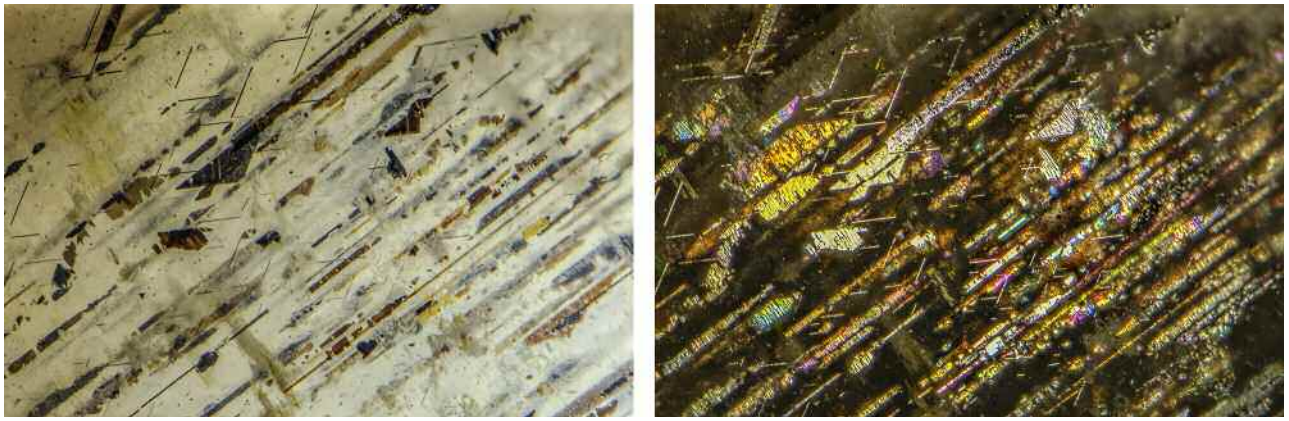

Figure 5. This octahedral-shaped negative crystal in a Burmese red spinel is filled with colorless carbonate crystals, yellow sulfur-rich liquid, opaque sulfide crystals, and diaspore fibers. Photomicrograph by Victoria Raynaud; field of view 1.20 mm.

to be small (though some large multicrystalline specimens up to 30 cm in diameter have been recovered). Base colors include blue-gray, tan, and a pink color apparently induced by additional fine hematite inclusions.

Stephen Challener
Raleigh, North Carolina

Nathan Renfro and Ziyin Sun
GIA, Carlsbad

Complex Yellow Fluid Inclusions in Red Burmese Spinel

Spinel has found new popularity and is now recognized as a birthstone for August. Some of the most desirable stones come from Myanmar, as they exhibit a pure red color with a light tone, accompanied by extremely high fluorescence under long-wave UV. Red Burmese spinel can also be found with a dark tone and much weaker fluorescence. The main localities that produce the highly fluorescent spinel are Namya in northern Myanmar and Man Sin in the Mogok Valley (V. Pardieu, "Hunting for 'Jedi' spinels in Mogok," Spring 2014 *G&G*, pp. 46–57). Clean stones are rare, as the majority have inclusions consisting of colorless carbonate crystals and complex multiphase negative crystals. These complex negative crystals contain a sulfur-rich yellow liquid, opaque metal sulfides, transparent carbonate daughter crystals, diaspore fibers, and a gas bubble. This unique yellow complex fluid inclusion (figure 5) is only known to occur in Burmese spinel and therefore serves as a good indicator of this origin.

Wim Vertriest
GIA, Bangkok

Victoria Raynaud
DANAT, Manama, Bahrain

Tourmaline Crystals on Burmese Ruby

During a GIA field expedition to Mogok, Myanmar, a tiny but interesting sample was acquired. This 0.552 ct ruby was purchased from local Kanase miners who process the tailings of the larger mines in the Kyatpyin Valley, just west of the town of Mogok. The ruby is associated with pure white calcite and bluish green tourmaline (figure 6).

Many rubies form in marble, especially in the deposits related to the Himalayan orogeny (Afghanistan, Tajikistan, Myanmar, and Vietnam), so calcite as an inclusion or associated mineral with these gems is common. While tourmaline in combination with ruby is not unheard of, it is a relatively unusual combination. LA-ICP-MS chemical analysis showed that the tourmaline was a Na-Mg-rich dravite. Tourmalines are of great interest to geologists be-

Figure 6. Bluish green tourmaline crystals and white calcite on a Burmese ruby. Photo by Charuwan Khowpong; field of view 2.48 mm.

Figure 7. This vibrant yellowish green crystal in a faceted ruby from Myanmar was identified as vesuvianite. Photomicrograph by Nathan Renfro; field of view 1.20 mm.

cause their isotopic and trace element composition are potentially strong indicators of the formation environment of the tourmaline and the associated minerals, in this case ruby.

Wim Vertriest and Charuwan Khowpong
GIA, Bangkok

Vesuvianite in Burmese Ruby

It is a pleasant surprise when a gemologist encounters a vibrantly colored crystal in a gemstone, as most gems are either inclusion free or contain inclusions that are weakly colored due to their small size. When the authors discovered a vibrant yellowish green crystal in a Burmese ruby (figure 7), it was a very welcome sight. Green crystals in corundum are not common but do occur occasionally. Green spinel and pargasite both occur in gem corundum. The former, a singly refractive mineral, was ruled out immediately because this inclusion behaved as a doubly refractive mineral when examined between crossed polarizers. Doubly refractive pargasite remained a possibility. The surprise came when Raman microspectrometry identified the yellowish green crystal as vesuvianite, also known as idocrase. To the authors' knowledge, this is the first time vesuvianite has been reported as an inclusion in ruby.

Nathan Renfro and John Koivula
GIA, Carlsbad

Wollastonite Blizzard Within Glass

A collection of lovely faceted blue beads was presented to author EAS during an annual meeting of inclusion specialists at the 2017 Tucson shows. While most specimens of interest highlighted in these meetings are of extraordinary naturally occurring minerals and gem materials—some of which have appeared in this column—these rather ordinary beads were intriguing for the veritable blizzard of translucent colorless needles and short euhedral crystals that filled each one. They created a beautiful optical effect, especially when illuminated from below (figure 8). Upon acquisition, the original owner had been told these were Russian synthetic quartz, and indeed their age and azure color suggested such an origin. It came as a surprise when standard gemological testing (RI of 1.518, SG of 2.47, and the absence of birefringence) identified the beads as glass, making the internal scene even more intriguing for its natural appearance. Raman spectroscopy at GIA's Carlsbad laboratory identified the beads as manufactured glass, and the majority of the nee-

Figure 8. Faceted manufactured glass beads measuring approximately 8 mm in diameter. Photo by Robison McMurtry.

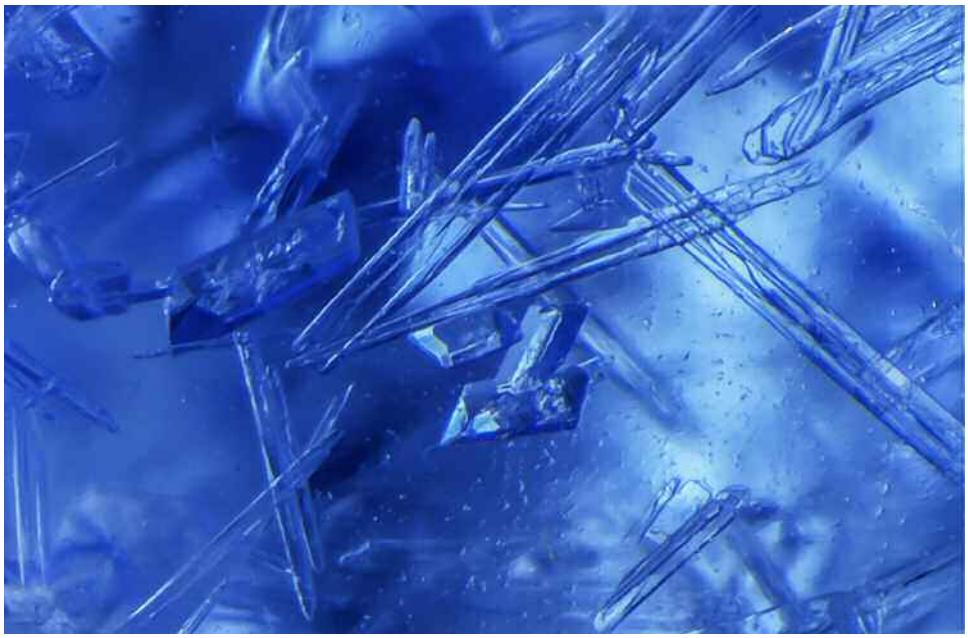

Figure 9. Transmitted light reveals a blizzard of transparent wollastonite needles within the glass host, an indication of devitrification. Interspersed among the needles are blocky crystals of diopside. Photomicrograph by Nathan Renfro; field of view 2.03 mm.

dles as the calcium silicate mineral wollastonite (figure 9). Additionally, relatively small blocky crystals scattered among the needles were conclusively identified as diopside (see Summer 2010 Lab Notes, p. 144).

Inclusions in glass such as wollastonite and diopside are indicators of devitrification, a process by which various components of the glass's composition crystallize out when subjected to high temperatures and/or changes in temperature. The process varies according to the type of glass. This may also happen in natural glasses, as with obsidian, resulting in the attractive lapidary material known as snowflake obsidian, which sports white blooms of cristobalite crystals on a black background. Devitrified glass is also sometimes used to imitate natural gems, as seen in manufactured "meta-jade." The beautiful blue inner world of these beads makes them a welcome addition to one's library of inclusions.

Elise A. Skalwold
Ithaca, New York
Nathan Renfro

Quarterly Crystal: Shattuckite in Quartz

For our "Quarterly Crystal" in the Micro-World column, we are always searching for unusual crystal specimens that contain interesting mineral inclusions and other micro-features worthy of description. This quarter's offering is an intergrown cluster of quartz crystals that play host to a rich blue deposition of the orthorhombic copper silicate mineral shattuckite, which typically forms aggregates of spherulitic to circular masses composed of acicular crystals (figure 10). The 41.27 mm long quartz crystal grouping (figure 11) came from the Kandesei mine in the Kunene region of Namibia and was acquired from Jordi Fabre (Fabre Minerals, Barcelona).

The inclusions were situated in the quartz crystals in the form of phantoms that developed through the deposition of the shattuckite on the surface. Laser Raman microspectrometry identified the phantom layers as shattuckite. As the quartz continued to grow, the shattuckite was captured as inclusion phantom planes tracing the form of the original quartz host.

Named for the type locality—the Shattuck mine in Bisbee, Arizona—shattuckite is a medium to deep blue mineral with a silky luster. A secondary mineral in oxidized copper deposits, shattuckite is often found together with ajoite, chrysocolla, and malachite, in addition to quartz.

John Koivula

Figure 10. As an inclusion in quartz, shattuckite typically forms aggregates of circular to spherulitic masses composed of acicular crystals. Photomicrograph by Nathan Renfro; field of view 3.55 mm.

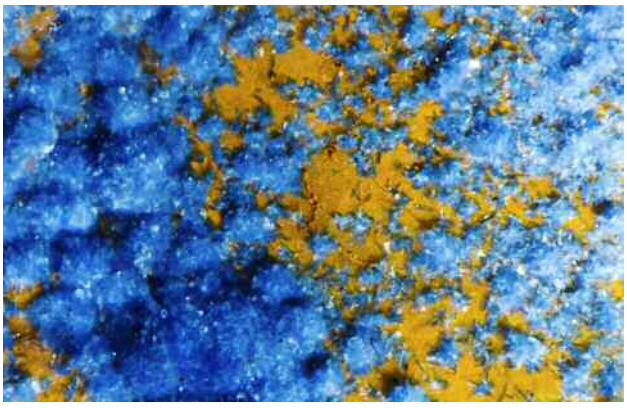

Figure 11. Measuring 41.27 mm and weighing 164.63 ct, this quartz crystal cluster contains a phantom composed of an abundance of deep blue radial concretions of shattuckite, forming a rich blue felted mat. Photo by Kevin Schumacher.

G&G
Gem News International

Contributing Editors
Emmanuel Fritsch, *University of Nantes, CNRS, Team 6502, Institut des Matériaux Jean Rouxel (IMN), Nantes, France* (fritsch@cnrs-imn.fr)
Gagan Choudhary, *Gem Testing Laboratory, Jaipur, India* (gagan@gjepcindia.com)
Christopher M. Breeding, *GIA, Carlsbad* (christopher.breeding@gia.edu)

COLORED STONES AND ORGANIC MATERIALS

Preliminary observations on facet-grade ruby from Longido, Tanzania. With rubies discovered about 100 years ago, the Longido district of Tanzania is one of the longest-known occurrences in Africa. The deposit is famous for its "ruby-in-zoisite," consisting of large red corundum crystals in a striking green zoisite matrix, often speckled with black amphibole spots. The majority is used for carving, but occasionally facet-quality material is discovered (D. Dirlam et al., "Gem wealth of Tanzania," Summer 1992 *G&G*, pp. 80–102).

For this study, 16 transparent rubies (figure 1) were collected during a July 2016 field expedition. The stones were acquired at the Mundarara mine in Longido and from a dealer in a nearby trading post. Most of the rough material ranged from 1 to 3 ct, although one heavily fractured piece weighed about 7 ct. Colors ranged from red to purplish red, very similar to the color of high-quality Mozambican ruby. Fluorescence was medium red under long-wave UV and weak red under short-wave UV.

Figure 1. Sixteen samples of facet-quality ruby (0.8–7.1 ct) from Longido, Tanzania. Photo by Sasithorn Engniwat.

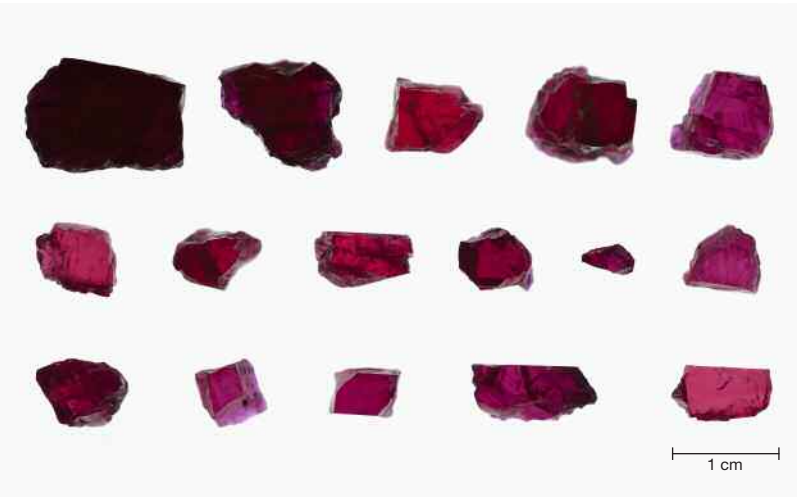

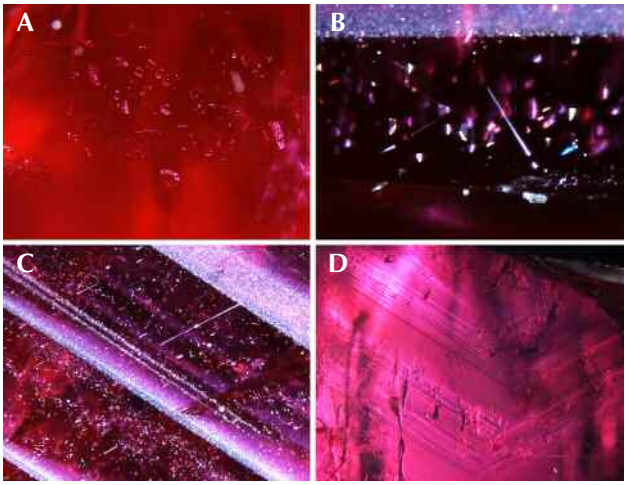

Figure 2. Internal features of ruby from Longido, Tanzania. A: A group of irregular thin films; field of view 1.6 mm. B: An array of reflective platelets with needles; field of view 0.9 mm. C: Short and long needles together with thin films; bands of fine reflective particles are also seen. Field of view 2.0 mm. D: Angular internal growth; field of view 4.0 mm. Photomicrographs by Boodsakorn Kongsomart.

The inclusion scenes (figure 2) had features similar to those of rubies from Mozambique: short needles, particle

Editors' note: Interested contributors should send information and illustrations to Stuart Overlin at soverlin@gia.edu or GIA, The Robert Mouawad Campus, 5345 Armada Drive, Carlsbad, CA 92008.

Gems & Gemology, Vol. 53, No. 4, pp. 472–490.

TABLE 1. Trace element concentrations in rubies from East African deposits.

Source		Trace element (ppma)				
Country	Mine	Cr min-max (avg., SD)	Fe min-max (avg., SD)	Ga min-max (avg., SD)	Mg min-max (avg., SD)	V min-max (avg., SD)
Tanzania	Longido, facet-grade (n=16)	1604–5059 (3300, 791)	62–544 (403, 80)	6–10 (7, 1)	7–42 (13, 7)	3–25 (5, 4)
	Longido, carving-grade (n=5)	1839–6235 (3760, 1185)	350–868 (565, 151)	5–8 (6, 0)	9–130 (32, 31)	2–4 (3, 0)
	Winza, facet-grade (n=14)	161–1094 (583, 295)	405–1596 (816, 276)	4–11 (6, 1)	0–118 (22, 21)	0–1 (1, 0)
Mozambique	Montepuez, Mugloto, facet-grade (n=14)	506–1737 (1167, 318)	851–2034 (1534, 243)	5–12 (9, 1)	11–50 (24, 10)	2–7 (4, 1)
	Montepuez, Maninge Nice, facet-grade (n=5)	1886–4941 (2868, 813)	261–402 (331, 30)	6–9 (7, 1)	19–47 (31, 8)	1–6 (3, 1)
Madagascar	Didy, facet-grade (n=21)	33–2698 (440, 498)	533–1274 (856, 198)	3–17 (8, 4)	0–67 (13, 14)	2–17 (5, 4)
	Andilamena, facet-grade (n=14)	53–1569 (403, 377)	559–1559 (1009, 253)	7–21 (14, 4)	19–53 (36, 7)	4–29 (18, 7)
	Zahamena, facet-grade (n=66)	135–3922 (1196, 874)	284–1994 (912, 249)	10–30 (16, 4)	13–61 (35, 8)	10–100 (17, 11)
Malawi	Chimwadzulu, facet-grade (n=18)	269–1816 (648, 377)	953–2760 (1697, 497)	5–15 (8, 3)	10–39 (21, 6)	1–10 (5, 2)

n = number of samples analyzed. On each sample, a minimum of three spots were measured. All the samples were facet grade except those from Longido, Tanzania, which included both facet and carving grades.

banding, and reflective platelets (V. Pardieu et al., "Rubies from the Montepuez area, Mozambique," *GIA News from Research*, Oct. 1, 2013). The most common inclusions were thin films (figure 2A), a combination of needles and reflective platelets (figure 2B), and particle banding (figure 2C). In addition, dense particulate planar clouds were arranged mostly parallel to each other and associated with short and long needles (again, see figure 2C). Internal growth zones (figure 2D) and twinning features were also found. Several types of crystals were identified by Raman spectroscopy, including amphibole, mica, and feldspar. Undetermined opaque metallic inclusions were also observed.

Various advanced analytical techniques were used to characterize the properties of the studied rubies. Fourier-transform infrared (FTIR) spectroscopy revealed strong absorption features consistent with boehmite in all samples. Other minerals that are normally present in ruby, such as diaspore or kaolinite, were not detected in the studied rubies.

The trace element concentrations of these rubies were analyzed with laser ablation–inductively coupled plasma–mass spectrometry (LA-ICP-MS) and compared to ruby from other East African sources (table 1). The rubies from Longido were extremely rich in Cr and fairly low in Fe compared to other African sources. The only East African deposit producing ruby with similar concentrations of chromophores is Maninge Nice in Mozambique, but the facet-grade material from Longido has lower magnesium content on average. Other deposits can be separated from Longido based on other trace elements (again, see table 1), although minor overlap cannot be excluded.

While Longido is traditionally known for large ruby-in-zoisite specimens, facet-grade rough is also produced and can yield attractive gemstones. Chemical analysis revealed an extremely high chromium concentration in both facet- and carving-grade ruby. While the internal features of the rubies from Longido are quite similar to those of other African deposits, trace element composition can aid in positively identifying their origin.

Boodsakorn Kongsomart, Wim Vertriest, and Vararut Weeramonkhonlert
GIA, Bangkok

Figure 3. A selection from Campbell Bridges's tsavorite collection, displayed at the 2017 AGTA Tucson Gem Fair. This collection includes some of the most important pieces found in the past half century. Photo by Robert Weldon/GIA, courtesy of the Bridges family.

Celebrating 50 years of tsavorite. The year 2017 marked the 50th anniversary of Campbell Bridges's discovery of tsavorite. At the 2017 AGTA Tucson Gem Fair, the Smithsonian Institution hosted a selection of historical pieces from Bridges's personal collection to commemorate his life's work (figure 3).

Starting in the front row and proceeding from left to right, we begin with two crystals that are some of the first tsavorites Bridges discovered, near Komolo, Tanzania, in 1967. These are among the first samples that were analyzed to identify this new gemstone.

Next, the tsavorite in matrix represents the 1970 discovery in Taita, Kenya, at Bridges's GG3 mine. Also represented from this location is a lovely tsavorite "thumbnail" unearthed in 1971. Some years prior, Bridges was engaged by Tiffany & Co. as a consultant. He was the first to bring tanzanite to the United States, and was credited with the discovery of tsavorite in Tiffany ads introducing the gem to the public in 1974 (figure 4).

The three large tsavorite rough samples weighing more than 5 grams each were found in 1980 at a source Bridges christened the Scorpion mine. The vibrant yet rich pure green to bluish green hue became a well-known characteristic of material from this mine. Over the following four decades, the Scorpion mine would prove to be the world's most prolific producer of fine tsavorite.

The next six rough pieces, weighing 5 to 25 grams, were recovered in 1992 from the famed Bonanza tunnel at the Scorpion mine. The Bonanza tunnel is the richest tsavorite-bearing reef zone at Scorpion and has yielded some of the finest pockets the world has seen. The "saddle reef structure," a series of recumbent folds, is the characteristic geological feature identified by Bridges at the Scorpion mine. This distinctive structure has led to the mine's rich and consistent production throughout its history.

Rounding out the Scorpion mine material in the top left corner is an extremely rare terminated euhedral tsavorite crystal in matrix. As tsavorite occurs under very high pressures and temperatures, it is often highly fractured in rough form, making such an unblemished and well-formed specimen a remarkable occurrence.

Figure 4. In this 1973 photo, Campbell Bridges (right) discusses tsavorite with Henry B. Platt, former president of Tiffany & Co. Photo courtesy of the Bridges family.

In the top right corner, we have a tsavorite nodule in matrix that opens a window into the gem's formation and its associated minerals. This nodule was extracted in its entirety from the Bonanza reef three decades ago and kept intact.

On display (again, see figure 3) are tsavorite, surrounded in the matrix by tanzanite, calcite, pyrite, quartz, and graphite. Tsavorite and tanzanite can occasionally occur together, though their formation is separated by approximately 100 million years. Tsavorite forms under prograde metamorphism and tanzanite under retrograde metamorphism.

Keeping guard on this tsavorite bounty are the namesakes of the Scorpion mine. These pewter scorpions were directly cast from actual scorpions that patrolled the mine. Needless to say, it's advisable to check your shoes in the morning… Also on display is one of Campbell Bridges's earliest business cards, from 1967.

In the top row are four extraordinarily fine, loupe-clean faceted gemstones. None of these were ever on public display before the Tucson exhibit. The first is a lovely 25.10 ct "mint" green grossular garnet, unearthed in 1971 from Bridges's GG2 mine in Taita, Kenya. Interestingly, this color of mint green garnet has been found at all of the Bridges mines in Tanzania and Kenya over the decades. A strike may yield both richly colored high-chromium and vanadium-colored saturated tsavorite, as well as the far lighter, mint green garnet within the same pocket. This variety is most prevalent in Merelani, Tanzania, but also occurs near Komolo, Tanzania, as well as in Taita. While such material came from all three locations in the early years, it simply was not marketable back then. It was not until the 2000s that a real market for these garnets developed.

Next is an exceptional 31.27 ct oval from Merelani with a vivid blue-green color. This tsavorite retains fantastic brilliance even in low lighting, while maintaining a sufficient level of saturation under strong lighting.

Last but certainly not least are two tsavorite cushions. As to their origin, the Bridges family wishes to preserve an element of mystery. The 33.55 ct square cushion on the right is a loupe-clean gem exhibiting an exceptional blue-green color that is well saturated yet extraordinarily vivid. After a lifetime of dealing with tsavorite, the author considers this one of the finest examples ever produced between 10 and 50 carats.

The largest of the four faceted gemstones in this display is a 58.52 ct cushion. It is another loupe-clean example representing the pinnacle of what is possible in tsavorite. It also exhibits a strong blue-green color that glows in any lighting environment. This is the finest tsavorite above 50 ct observed by this author. Given its one-of-a-kind nature, the Bridges family felt it most appropriate to name the gem the "Golden Jubilee" in honor of tsavorite's 50th anniversary.

As tsavorite and the legacy of Campbell Bridges celebrate 50 years, the Bridges family wishes to thank the Smithsonian and the colored gemstone community for their support throughout the years.

Bruce Bridges
Bridges Tsavorite, Nairobi

New azurite-malachite mixture from Peru. Green malachite, $Cu_2(CO_3)(OH)_2$, is very popular as an ornamental stone, with huge quantities coming every year from deposits in the Katanga Province of the Democratic Republic of Congo. Blue azurite has a similar chemical composi-

Figure 5. This polished vein of azurite with malachite and chrysocolla mined from Cochapata measures 8.5 cm wide. Photo by J. Hyršl.

Figure 7. A cross-section of a 25-mm-wide malachite double stalactite from Cochapata. The stalactite on the right shows malachite with an azurite center. Photo by J. Hyršl.

tion, $Cu_3(CO_2)_2(OH)_2$, but is much more rare. Cabochons of pure azurite are usually quite dark and not very attractive. A blend of the two is much more appealing for jewelry, but this combination is seldom found. Attractive azurite-malachite mixtures are known mainly from old finds in Bisbee and Morenci, both in the U.S. state of Arizona. There was also a find of malachite-azurite-gypsum mixture from Peru's Moquegua region in 2012 (J. Hyršl, "Malachite-azurite from Peru," *Journal of Gemmology*, Vol. 34, No. 7, 2015, p. 564).

Another new azurite-malachite mixture appeared in 2016 and was originally described as from Puno, in southeastern Peru. In fact, it is from Cochapata, in the Cotabambas Province about 50 km southwest of Cuzco, situated in high mountains. According to a dealer who visited the locality, there are several outcrops of oxidized copper veins on a steep hill exploited by artisanal miners. The veins are up to about 20 cm wide, but the parts most useful for cutting are usually only a few centimeters wide. Several tons of the rough have already been sold in Lima to foreign dealers, with the largest piece weighing 80 kg.

Deep blue azurite is the main mineral found today in Cochapata, accompanied by light green malachite and, less commonly, light blue chrysocolla (figure 5). The most attractive specimens have malachite with a banded structure, but some possess a brecciated structure (figure 6). The rarest samples are stalactites of malachite up to 5 cm in length. Some were sliced perpendicular to the elongated growth direction to prepare very attractive stones with an agate-like structure (figure 7).

Jaroslav Hyršl (hyrsl@hotmail.com)
Prague

Figure 6. These azurite-malachite cabochons, fashioned from Cochapata material, measure up to 31 mm. Photo by J. Hyršl.

DIAMONDS

Two natural type IIa diamonds with strong phosphorescence and Ni-related defects. Strong phosphorescence under UV excitation is rarely seen in natural diamond and normally limited to hydrogen-rich type Ia or type IaA/Ib chameleons and type IIb diamonds (T. Hainschwang et al., "A gemological study of a collection of chameleon diamonds," Spring 2005 *G&G*, pp. 20–35; S. Eaton-Magaña and R. Lu, "Phosphorescence in type IIb diamonds," *Diamond and Related Materials*, Vol. 20, No. 7, 2011, pp. 983–989). When seen in other diamond types, an even rarer occurrence, it is shorter and less intense. Recently, the National Gemstone Testing Center (NGTC) in Beijing encountered two natural diamonds that showed extraordinarily strong blue phosphorescence and uncommon fluorescence colors under the DiamondView.

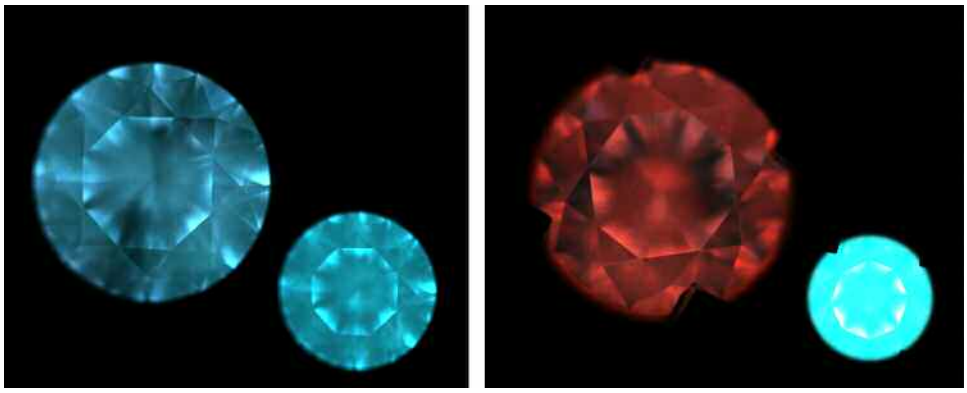

Figure 8. DiamondView images of two unusual diamonds (0.18 and 0.30 ct, respectively). Left: Unevenly distributed grayish blue fluorescence and strong blue phosphorescence. Right: Vivid red fluorescence, strong blue phosphorescence, and a dislocation network can be seen in the table. Images by Shi Tang.

The diamonds weighed 0.18 and 0.30 ct and were both graded as E color. Both were type IIa, with neither nitrogen absorption between 1100 and 1400 cm^{-1} nor boron-related absorption in their infrared spectra. Magnification and examination with a standard UV lamp showed no abnormal phenomena for natural type IIa diamonds. Instead of the deep blue fluorescence and inert phosphorescence that natural type IIa diamonds typically show in DiamondView imaging, the 0.18 ct diamond emitted unevenly distributed grayish blue fluorescence and strong blue phosphorescence, similar to that of a colorless HPHT synthetic diamond. The 0.30 ct diamond displayed vivid red fluorescence and strong blue phosphorescence, which is unusual for a natural colorless to near-colorless diamond (figure 8). Red fluorescence is rare in natural type IIa diamond and seldom reported (Summer 2016 Lab Notes, pp. 189–190).

Photoluminescence (PL) spectra collected with 532 nm laser excitation at liquid nitrogen temperature revealed something even more interesting. Along with the GR1 center emission at 741 nm typically seen in natural type IIa diamonds, the 883.0/884.7 nm doublet that is related to nickel impurity appeared in both samples' PL spectra (figure 9). This doublet, often referred to as the "1.40 eV center," is frequently seen in the {111} growth sectors of HPHT synthetic diamonds produced using Ni-based solvents/catalysts. Ni-related defects are more often seen in natural chameleon and greenish yellow diamonds (W. Wang et al., "Natural type Ia diamond with green-yellow color due to Ni-related defects," Fall 2007 *G&G*, pp. 240–243; Summer 2014 Lab Notes, pp. 151–152) but seldom found in colorless to near-colorless natural diamonds (e.g., Spring 2017 Lab Notes, pp. 95–96). For natural diamonds

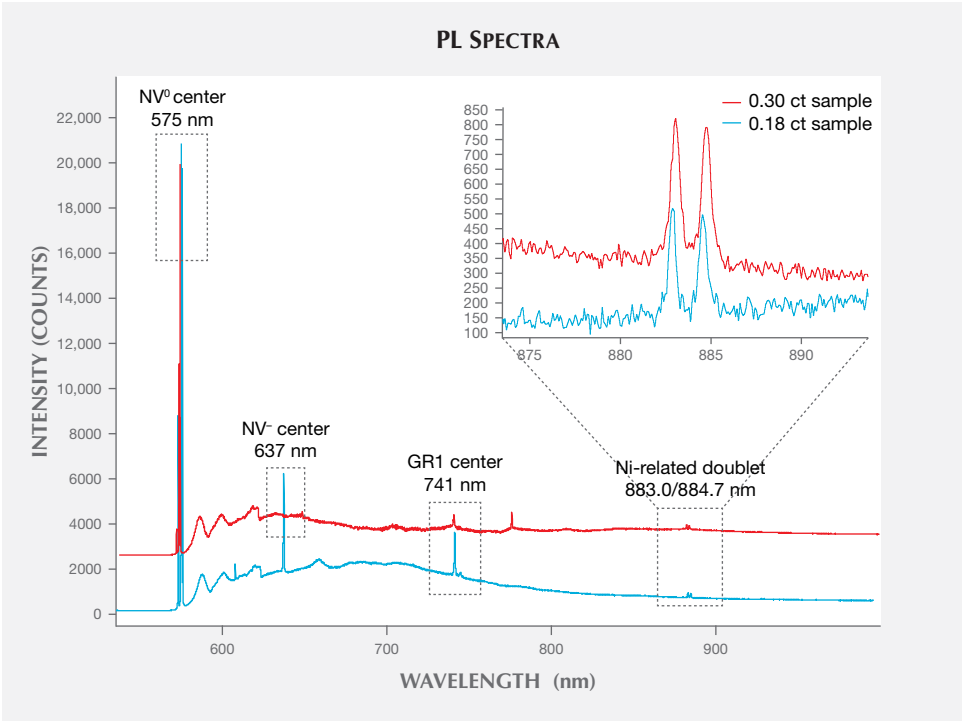

Figure 9. PL spectra of the two samples with 532 nm laser excitation. Both showed weak Ni-related doublets at 883.0/884.7 nm and strong NV centers at 575 and 637 nm, as well as the GR1 center at 741 nm.

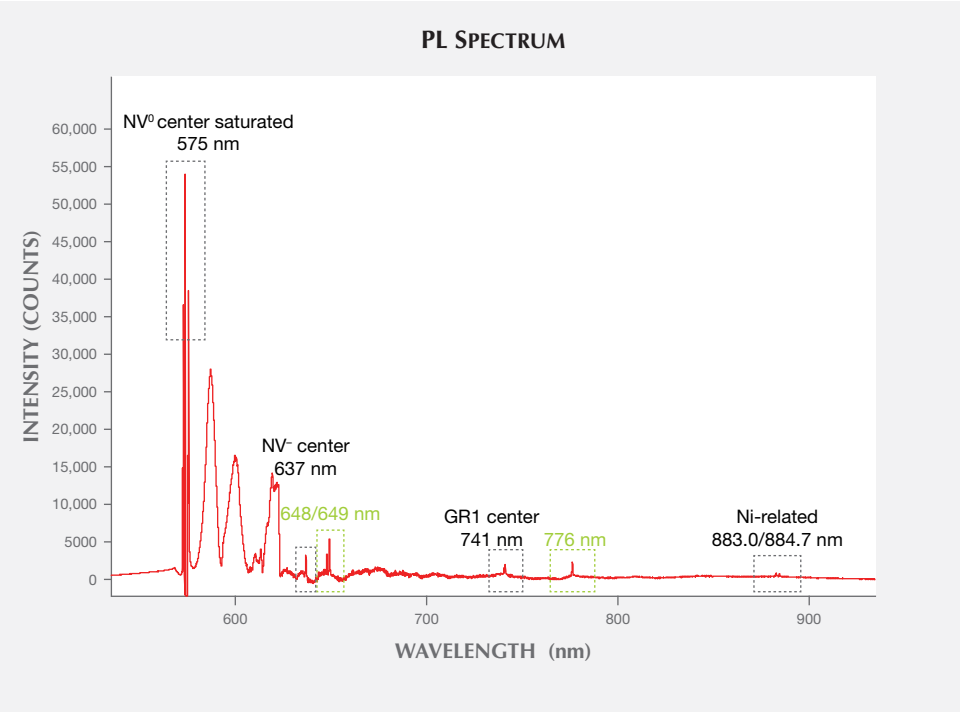

Figure 10. The PL spectrum of the 0.30 ct sample emitted with a 532 nm laser, at higher excitation energy. The NV^0 center peak is saturated, and emissions at 648 and 776 nm are clearly seen.

with such strong phosphorescence, the presence of Ni-related emissions is unusual.

The PL spectrum of the 0.30 ct sample also presented an extremely strong NV center at 575 nm, compared to the diamond emission at 572 nm, which explained the reddish fluorescence in the DiamondView image. In each sample's PL spectrum, the relative intensity of NV^0 (575 nm) is significantly stronger than that of NV^- (637 nm).

Furthermore, when we exposed the 0.30 ct sample to higher-energy excitation with the 532 nm laser to reveal more subtle features, the PL spectrum showed moderately strong emissions at 648/649 nm and 776 nm (figure 10). According to previous research, PL peaks at 648.2 and 776.4 nm are associated with boron in phosphorescing type IIb natural diamonds (Eaton-Magaña and Lu, 2011). Later studies ascribed the 648.2 nm defect to a boron-interstitial complex, while the 776.4 nm peak was assigned to a B-V complex (S. Eaton-Magaña and T. Ardon, "Temperature effects on luminescence centers in natural type IIb diamonds," *Diamond and Related Materials*, Vol. 69, 2016, pp. 86–95). These emissions may partly explain the strong phosphorescence of the 0.30 ct sample. Since they were not detected in the 0.18 ct sample, which also exhibited strong phosphorescence—the same is true of other phosphorescent natural IIa diamonds the authors have encountered before—this cannot be the full explanation.

Despite the synthetic-like luminescence color in DiamondView imaging and the Ni-related emissions in the PL spectra, the samples' Fourier-transform infrared (FTIR) spectra, UV-visible spectra, PL spectra, features observed under the crossed polarizing microscope, and UV reaction indicated that they are not of synthetic origin. These two samples demonstrated the diversity of luminescence and spectral features found in natural diamond. Their identification also highlights the importance of a comprehensive understanding of diamond origin.

Shi Tang (tangs@ngtc.com.cn), Zhonghua Song, Taijin Lu, Jun Su, and Yongwang Ma
NGTC, Beijing

Interesting growth structure in black diamond. The color of most black diamonds is attributed to graphite micro-inclusions or metallic inclusions (S.V. Titkov et al., "An

Figure 11. This 1.03 ct opaque round brilliant cut with a striking pattern of micro-inclusions was identified as a black diamond. Photo by Yujie Li.

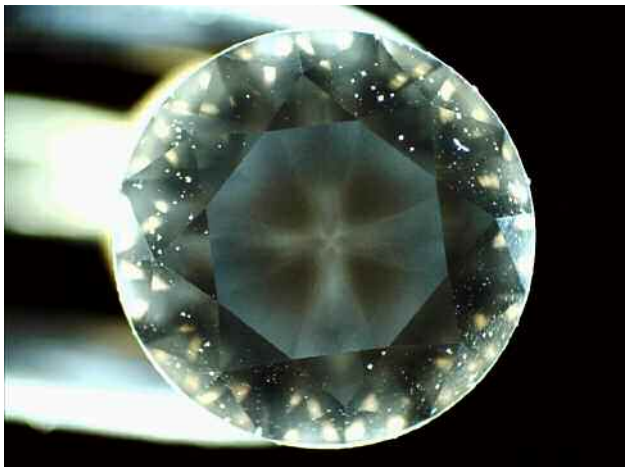

Figure 12. The "double cross" pattern seen in the black diamond. This pattern showed that the small inclusions were restricted to certain sectors, indicating that the diamond crystallized through two separate processes. Photo by Yujie Li; field of view approximately 4 mm.

investigation into the cause of color in natural black diamonds from Siberia," Fall 2003 *G&G*, pp. 200–209), and it is rare to see dense clouds of micro-inclusions producing a black appearance (see Spring 2007 Lab Notes, pp. 52–53). Since November 2016, the National Gemstone Testing Center (NGTC) in Shanghai has routinely received large quantities of polished black diamonds. One such stone, a 1.03 ct opaque round brilliant (figure 11) that we believed to have been heat treated, had a striking pattern of micro-inclusions we had never seen before.

Microscopic observation revealed a "double cross" pattern arising from an abundance of pinpoint-like gray inclusions restricted to certain sectors of the diamond (figure 12). The outer black cross was oriented in the same direction as the inner pale cross. The inclusions' crystalline forms were too small to resolve at 40× magnification. These small inclusions absorbed a large proportion of the light entering the diamond, causing the black appearance. The FTIR absorption spectrum confirmed the diamond was type IaAB and H-rich, with nitrogen-related absorption from 1000 to 1500 cm^{-1}, a graphite-related peak at 1582 cm^{-1}, and H-related IR peaks at 1405, 2785, 3050, 3107, 3154, 3236, 4169, and 4496 cm^{-1}. We confirmed that the pinpoint-like inclusions were graphitized hydrogen clouds (see P. Johnson et al., "Hydrogen rich treated black diamonds," poster presentation at Geological Society of America 2016 annual meeting).

When observed in the high-energy short-wave UV radiation of the DiamondView (figure 13), the bulk of this black diamond displayed moderate yellowish green fluorescence. Four small areas were basically inert to UV radiation; these also corresponded to the dark cross.

The unique double cross pattern and the DiamondView image revealed an interesting growth structure. The diamond apparently underwent two distinct phases of growth, with each phase forming a cross developing from separate mixed-habit growth with contemporaneous cuboid and octahedral sectors. The well-developed cuboid growth sectors contained regions with cloud-like light scattering that caused the black parts; very poorly developed octahedral growth sectors with a small amount of inclusions formed the light cross. The cuboid growth sectors exhibited yellowish green fluorescence, while the inclusion-poor octahedral sectors were inert to the short-wave UV light.

The interesting pattern of inclusions and distinctive growth features of black diamonds such as this one needs more attention.

Contributors' note: This study was supported in part by the National Natural Science Foundation of China (grants 41473030 and 41272086).

Yujie Li, Hui Xu, Taijin Lu, Zhikun Hu, and Xinming Wang
NGTC, Shanghai

Figure 13. The pattern as seen in the DiamondView. The well-developed cuboid growth sectors exhibited yellowish green fluorescence, while the poorly developed octahedral growth sectors were inert to the short-wave UV light. The DiamondView also revealed a mixed-habit growth structure.

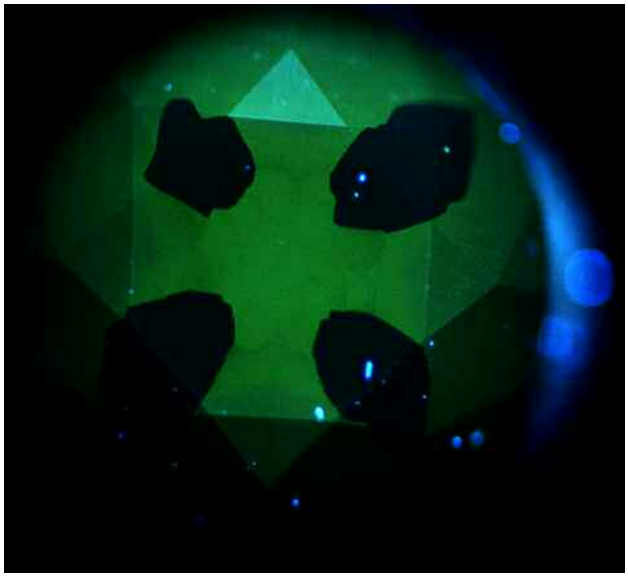

The Foxfire diamond, revisited. The largest gem-quality rough diamond found in Canada, reported earlier in *Gems & Gemology* (Summer 2016 GNI, pp. 188–189), has revealed remarkable responses to excitation with long- and mid-wave UV light. This 187.63 ct diamond (figure 14) was extracted from the Diavik mine in the Canadian Arc-

Figure 14. The 187.63 ct Foxfire rough diamond. Photo by Jeffrey Post.

tic in the spring of 2015. Aptly named for the aurora borealis, the "Foxfire" displays unusual fluorescence and phosphorescence behavior upon exposure to ultraviolet light. As previously reported, this type Ia diamond has a high concentration of nitrogen impurities, a weak hydrogen-related absorption at 3107 cm^{-1}, and typical "cape" absorption lines.

Exposing this stone to the near-band-gap ultraviolet light of the DiamondView instrument (about 210 nm) and short-wave UV (253.7 nm) results in only very weak fluorescence and phosphorescence, as reported earlier. However, exposure to mid- and long-wave UV (313 nm and 365.0 nm, respectively) produces extremely strong blue fluorescence and strong, long-lived orangish phosphorescence (figure 15).

Another surprising result of exposing the Foxfire diamond to UV light is a noticeable color change from very pale yellow to a light brown color (figure 16). Fortunately, the diamond reverts to its original color in a matter of minutes in ambient room lighting.

We further examined the spectral characteristics of the UV-excited phosphorescence emission with the spectrometer previously used to study phosphorescence from the Hope and other colored diamonds (S. Eaton-Magaña et al., "Fluorescence spectra of colored diamonds using a rapid, mobile spectrometer," Winter 2007 *G&G*, pp. 332–351; S. Eaton-Magaña et al., "Using phosphorescence as a fingerprint for the Hope and other blue diamonds," *Geology*, Vol. 36, No. 1, 2008, pp. 83–86). In the present experiments, the UV light sources employed were mineralogical short-, mid-, and long-wave UV lamps. Figure 17 displays the spectral emission between 350 and 1000 nm (approximately 10 nm resolution) as a function of time after turning off the UV light. The most intense emission resulted from long- and mid-wave UV excitation, while phosphorescence excited by short-wave UV was extremely weak.

The spectra of the "orange" phosphorescence reported above are unusual and distinct from those of other natural and lab-grown phosphorescent diamonds we have examined. We speculate that the primary mechanism for phosphorescence in diamonds is light emission resulting from recombination of electrons trapped at ionized donors and holes trapped at ionized acceptors that are in close proximity to one another. The long time delay results from the thermal movement of the trapped electrons or holes to retrap close enough to one another (P.J. Dean et al., "Intrinsic and extrinsic recombination radiation from natural and synthetic aluminum-doped diamond," *Physical Review*, Vol. 140, No. 1A, 1965, p. A352–A386; B. Dischler et al., "Diamond luminescence: Resolved donor-acceptor pair recombination lines," *Diamond and Related Materials*, Vol. 3, 1994, pp. 825–830). In the case of the Foxfire, we cannot identify as yet the nature of either the acceptors or donors involved.

Similarly, the phenomenon of the observed color change from light yellow to light brown with UV excitation and the

Figure 15. Left: The Foxfire diamond, photographed in daylight-equivalent lighting. Center: The fluorescence exhibited in a darkened room while the diamond was exposed to long-wave UV. Right: The phosphorescence shown in a darkened room immediately after extinguishing long-wave UV excitation. Photos by Jeffrey Post.

Figure 16. The Foxfire under ambient room lighting, before (left) and just after exposure to long-wave UV light (right). Photos by Jeffrey Post.

reversal to light yellow has no detailed explanation yet. Such color changes, or sometimes a lightening of color, are often observed in natural diamonds. It is speculated that these are due to charge transfer between various defects (donor or acceptor states) within diamond. Diamond is inherently an insulator where electric charges move very slowly and their motion depends on the nature of the defects present, the temperature of the diamond, and its exposure to light. For an interesting discussion, see K.S. Byrne et al., "Chameleon diamonds: Thermal processes governing luminescence and a model for the color change," *Diamond and Related Materials*, Vol. 81, 2018, pp. 45–53.

James E. Butler and Jeffrey E. Post
Smithsonian Institution,
National Museum of Natural History
Washington, DC

Wuyi Wang
GIA, New York

TREATMENTS

Coated beryl imitating emerald. Two major issues related to emerald are origin determination and the presence and quantity of fillers. An emerald's value depends in part on the quality of the stone and treatments applied, so examination with a gemological microscope is an essential part of any analysis.

A pair of earrings (figure 18, top) weighing a total of 84.06 grams was submitted to the Lai Tai-An Gem Lab for identification. The earrings consisted of numerous green drilled briolettes with a vitreous luster. The client, who claimed they were natural emeralds, granted permission to remove one piece to aid in identification. Testing gave a spot RI of 1.57, an SG of 2.67, and an inert reaction to both short-wave and long-wave UV, consistent with beryl. Microscopic observation revealed liquid, crystal, and two-phase inclusions (figure 18, bottom). Infrared and Raman spectroscopy indicated that the loose stone, along with the similar stones still in the earrings, were beryl. Epoxy peaks at 3056, 3037, 2964, 2931, and 2872 cm^{-1} were obtained by FTIR spectroscopy (figure 19). However, the green color was unusual in that it appeared to be concentrated on the surface, which was confirmed by additional testing.

Magnification with diffused illumination clearly showed concentrated patches of green color with "colorless" boundaries (figure 20, left), as often seen in diffusion-

Figure 17. Phosphorescence emission vs. time after extinguishing long-wave (left), mid-wave (center), and short-wave UV excitation (right).

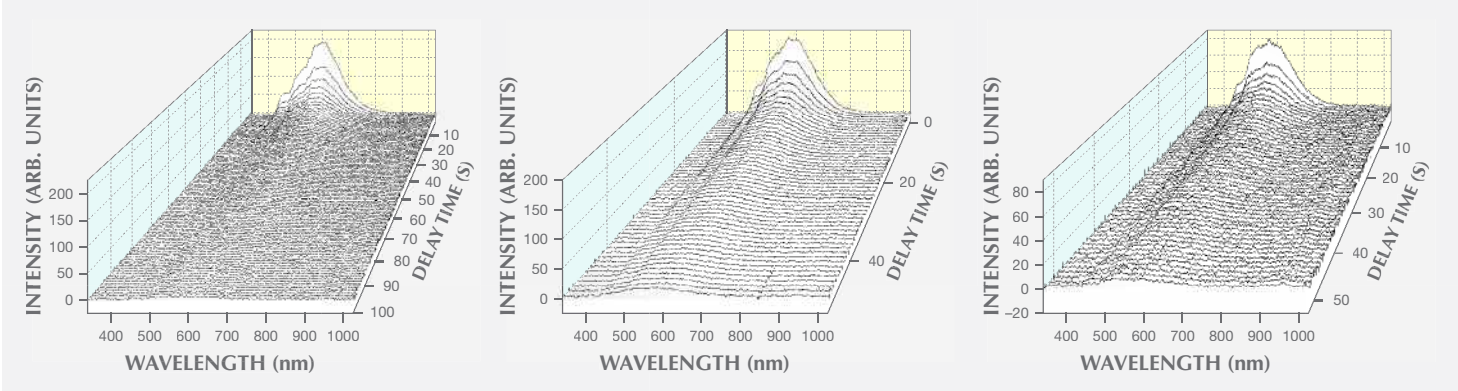

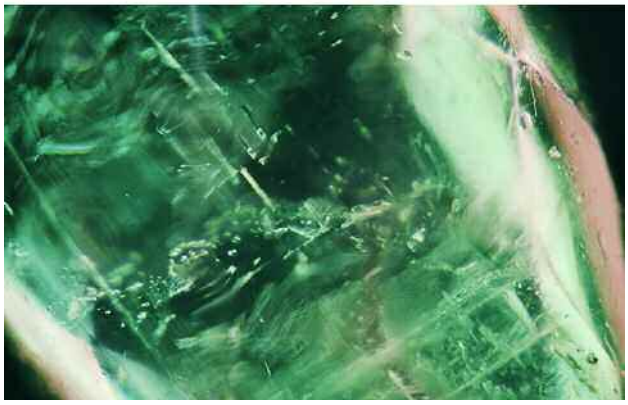

Figure 18. Top: The drilled green briolettes mounted in the pair of earrings submitted for identification. Bottom: Fluid inclusions, crystals, and two-phase inclusions proved the stones' natural origin; field of view 2.6 mm. Photos by Lai Tai-An Gem Lab.

treated stones such as corundum. Further observation by scanning electron microscopy (SEM) indicated a coating on the faceted surface (figure 20, right). DiamondView imaging revealed the fluorescence reaction of the underlying

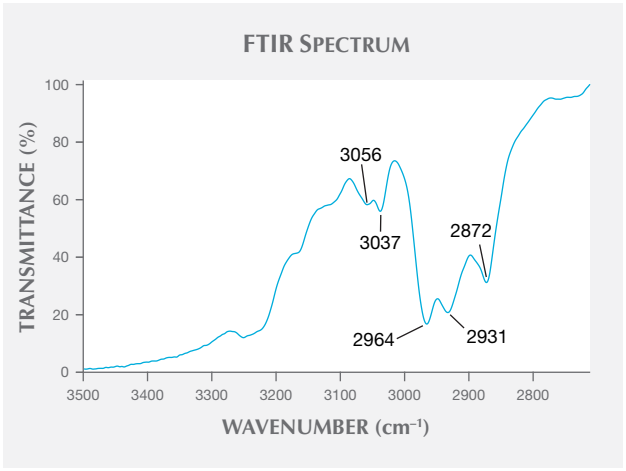

Figure 19. FTIR spectroscopy showed epoxy peaks at 3056, 3037, 2964, 2931, and 2872 cm^{-1}.

host beryl where the coating had been worn away at the facet junctions: When exposed to the ultra-short-wave UV of the DiamondView, the "colorless" areas reacted with a strong orange fluorescence (figure 21). UV-Vis-NIR spectra revealed differences between the test stone and a reference emerald. While emerald normally exhibits Cr^{3+}-associated main absorption bands at approximately 620 and 430 nm, the examined samples showed strong absorption bands at approximately 680 and 360 nm, as well as weaker bands at 620 and 430 nm (figure 22)

Coatings have been applied to various gemstones for decades, and most of the time they are easy to identify. Although this identification was not particularly challenging, it does show the importance of thoroughly examining jewelry in case treated stones have been incorporated into the design.

Larry Tai-An Lai (service@laitaian.com.tw)
Lai Tai-An Gem Laboratory, Taipei

Filled pearl with surface features. Pearl cultivation has been carried out for more than a century, with newer tech-

Figure 20. Left: Magnification with diffused illumination clearly showed the concentrated green areas of the coating and the boundaries of the underlying host beryl. Photomicrograph by Lai Tai-An Gem Lab; field of view 4.4 mm. Right: An SEM image from the specimen. The area labeled A shows the coated layer on the surface, while B shows facet boundaries without coating.

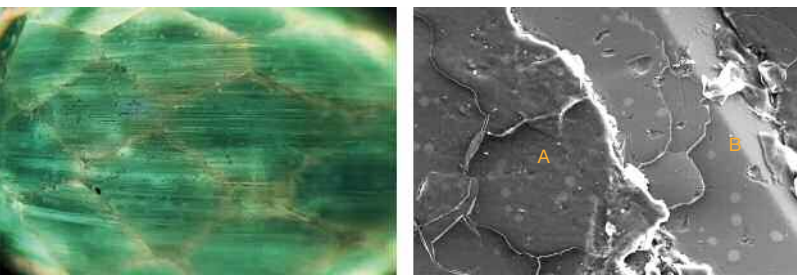

Figure 21. DiamondView imaging showed where the coating had been worn away at the facet junctions. The colorless areas reacted with a strong orange fluorescence after exposure to the short-wave UV radiation.

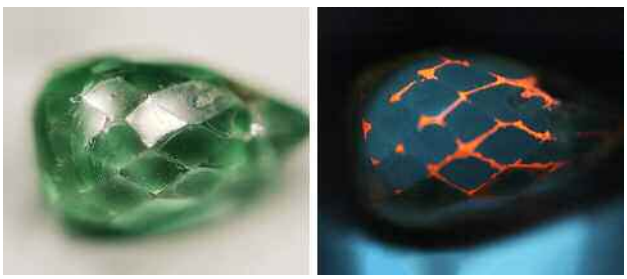

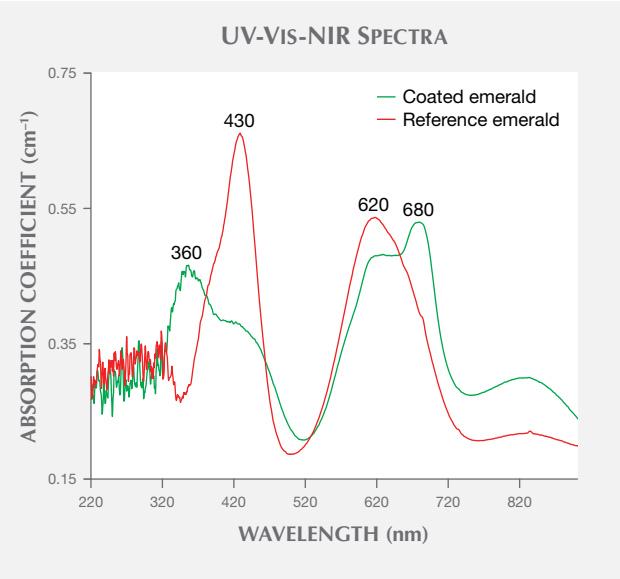

Figure 22. UV-Vis-NIR spectra show the differences between a reference emerald, which exhibits significant Cr^{3+}-associated main absorption bands at approximately 620 and 430 nm only (red trace), and the examined sample, which contains absorption bands at approximately 680 and 360 nm in addition to the 620 and 430 nm bands (green trace).

niques supplying the trade with larger and more consistently round freshwater and saltwater pearls. While natural pearls are seldom perfectly round, their rarity makes them desirable nevertheless. The Lai Tai-An Gem Lab recently had the chance to examine a specimen that was purchased by the client as a "natural white pearl" (figure 23) while traveling in the Philippines.

Figure 23. This 20.60 ct specimen was purchased by the client as a "natural white pearl." Photo by Lai Tai-An Gem Lab.

Figure 24. Two fillings displayed a coarse appearance and lower luster that differed from the rest of the pearl. Photomicrographs by Lai Tai-An Gem Lab; fields of view 11.5 mm (left) and 8.6 mm (right).

The white baroque pearl measured 20.0 × 19.0 × 13.3 mm and weighed 20.60 ct, with an SG of 2.60. It exhibited pink overtone. Long-wave UV produced a strong chalky blue reaction. Magnification revealed the typical overlapping platelet structure expected for nacreous pearls, but two abnormal surface features were also observed. These two areas displayed a coarse appearance and lower luster that differed from the rest of the pearl (figure 24).

We further analyzed the abnormal surface features to gather more data for future reference. DiamondView imaging showed a noticeable difference between the nacreous areas and the filled portions (figure 25). Raman analysis of the surface features revealed epoxy peaks at 635, 1108, and 1604 cm^{-1} and aragonite peaks at 1084 and 701 cm^{-1} (figure

Figure 25. The two filled portions of the pearl, shown in visible light (left images) and the DiamondView (right images). The DiamondView reaction showed a noticeable difference between the nacreous areas and the filled portions of the pearl.

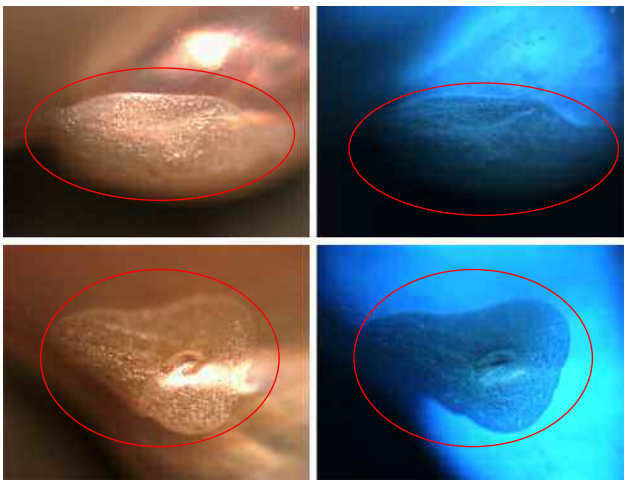

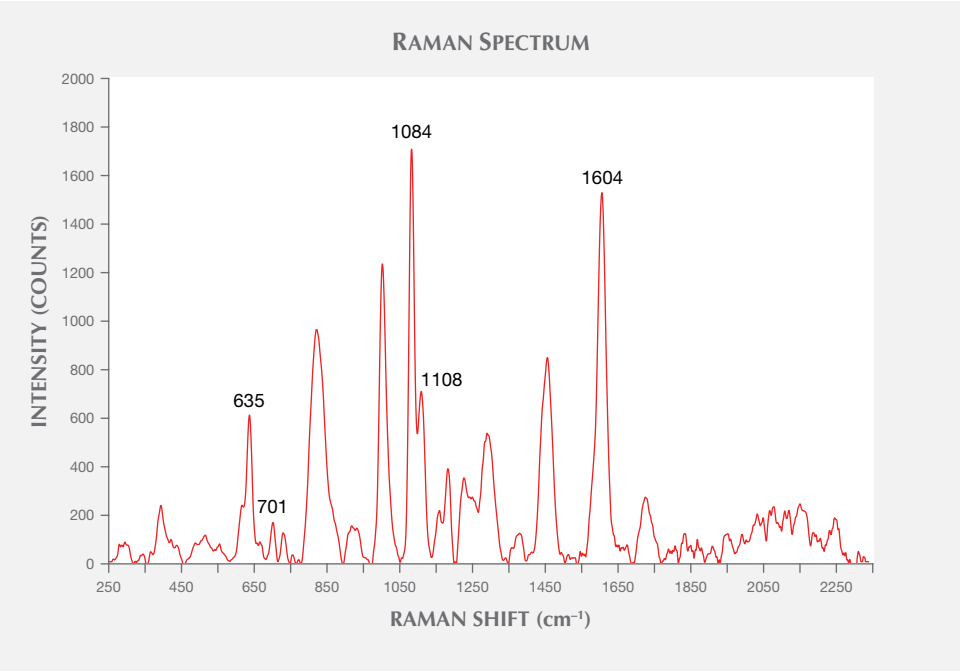

Figure 26. Raman analysis of the pearl revealed epoxy peaks at 635, 1108, and 1604 cm^{-1} and aragonite peaks at 701 and 1084 cm^{-1}.

26). These were consistent with results from FTIR reflectance spectrometry that showed calcium carbonate in the form of aragonite, with peaks at approximately 878 and 1484 cm^{-1}.

X-radiography (figure 27) proved this was a bead-cultured pearl with a pre-drilled nucleus typically used in freshwater pearl cultivation. The filling was very shallow due to the presence of mother-of-pearl (not visible). Energy-dispersive X-ray fluorescence (EDXRF) analysis detected higher levels of manganese, confirming the pearl's freshwater origin. The result came as a surprise to the client, who was expecting confirmation of a natural pearl. Such coatings and fillings, which we have seen before, show the importance of obtaining a reliable laboratory report when purchasing such a large pearl.

Figure 27. X-radiography proved this was a bead-cultured pearl. The filling was very shallow due to the presence of mother-of-pearl (not visible). Image by Lai Tai-An Gem Lab.

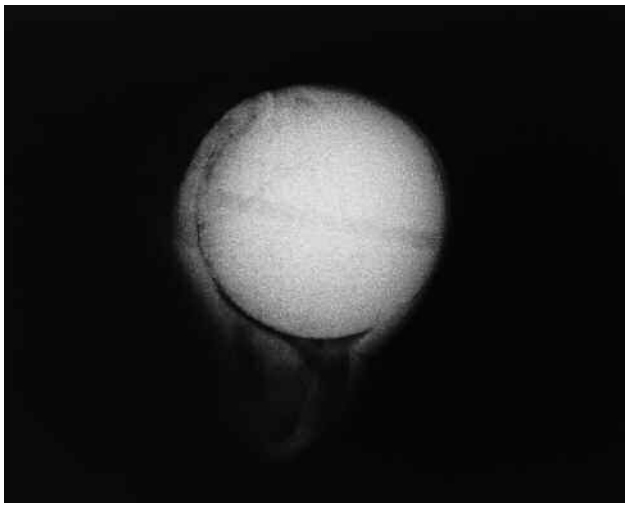

Larry Tai-An Lai (service@laitaian.com.tw)
Lai Tai-An Gem Laboratory, Taipei

Update on dyed hydrophane opal. Dyed purple opals first appeared in the gem trade in 2011 (N. Renfro and S.F. McClure, "Dyed purple hydrophane opal," Winter 2011 *G&G*, pp. 260–270). Recently, the authors became aware of similar material with vibrant blue and pink bodycolors (figure 28). From 2015 to 2017, a jewelry designer reportedly purchased over 500 carats of vivid pink and blue opals from a dealer she met at a small regional gem show in California. The dealer did not disclose that the material was dyed and claimed that these intense colors were from a new opal discovery in Mexico. This kind of misrepresentation could damage consumer confidence in all opals.

In July 2017, author EB received the two opals in figure 28 for examination. After determining that they were likely color treated, he sent both samples to GIA's Carlsbad lab for further testing. With permission from the owner, each opal was cut in half to obtain a control sample and a test sample. The test samples (one blue and one pink) were soaked in acetone and hydrogen peroxide solutions to determine if their colors were stable. These two opals were carefully examined and, like the dyed purple material from 2011, were consistent with hydrophane opal from Ethiopia that had been dyed. Both stones displayed a "digit pattern" play of color (B. Rondeau et al., "On the origin of digit pat-

Figure 28. These two opals (21.75 and 15.12 ct) were represented as natural-color blue and pink opal from Mexico. Photo by Robison McMurtry.

terns in gem opal," Fall 2013 *G&G*, pp. 138–146). They also showed small spots of saturated color at the surface, consistent with dye (figure 29).

Both stones were soaked in acetone to collect some of the dye material for color spectroscopic analysis. The acetone with residual dye was measured and artificially concentrated by a factor of 20 by multiplying the very low absorption values measured. The measurements produced a spectrum consistent with an organic dye, characterized by broad band absorption features in both the pink and blue samples (figure 30). The absorption measurements were then converted to transmission spectra using GRAMS/AI spectroscopy software by Thermo Fisher Scientific. Color space coordinates were calculated from the transmission spectra and plotted as a color swatch. The hues produced were consistent with the bodycolor of each opal, confirming that the spectra represent the organic dye component (figure 30, inset).

The two samples were further tested to see if they could be restored to their original non-dyed state. As reported by Renfro and McClure (2011), soaking dyed purple opal in a solution of hydrogen peroxide removed the purple color. These new pink and blue samples were sliced in half and one piece of each sample was soaked in 3% hydrogen peroxide for up to two weeks. Their color saturation was significantly reduced, with the blue half turning white and the saturated pink half becoming very light pink (figure 31). It is possible that more time in the solution would have further reduced the pink color. Note that even though the samples lost their color, the dye molecules were not removed. But the hydrogen peroxide had oxidatively decomposed the dye into different molecules that did not absorb visible light and therefore could no longer impart color on the opals. Soaking dyed stones in hydrogen peroxide may be an effective way to remove the observed color in dyed opals, returning them to their natural appearance. In our experience, however, there is a risk of cracking when any hydrophane opal is immersed in a liquid.

Acetone allowed the removal of enough dye for spectroscopic analysis, proving that the coloring agent is an organic dye. While soaking the opals in acetone did not seem to greatly affect their color, soaking them in a hydrogen peroxide solution for several weeks removed the artificial color almost entirely. Upon further examination, we determined that they were originally hydrophane opals with a white bodycolor, likely from Ethiopia, that were color treated using an organic dye. These findings reaffirm the

Figure 29. Both the blue and pink opal showed dye color concentrations around pits and scratches on the surface, consistent with hydrophane opal that has been artificially dyed. Photomicrographs by Nathan Renfro; fields of view 2.34 mm (left) and 1.99 mm (right).

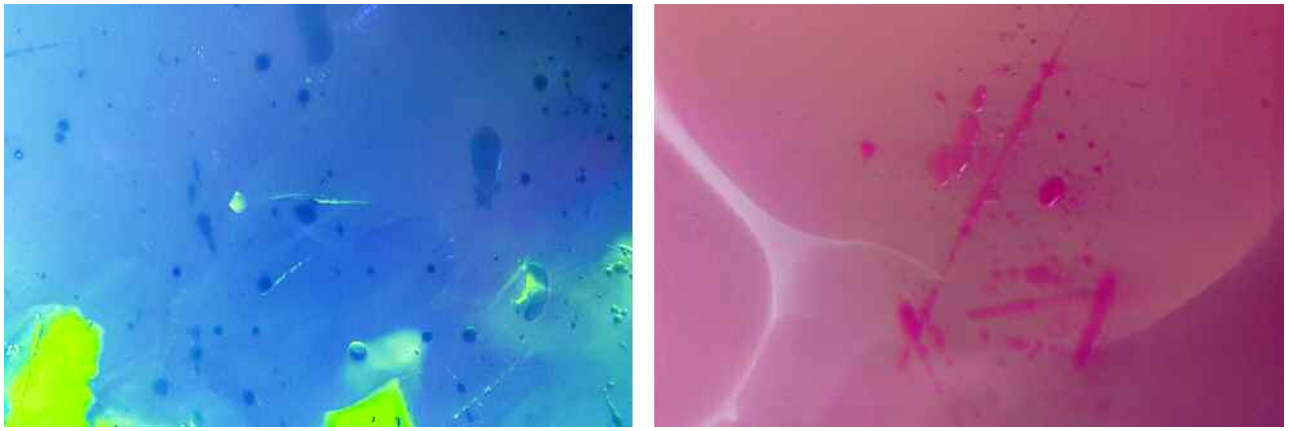

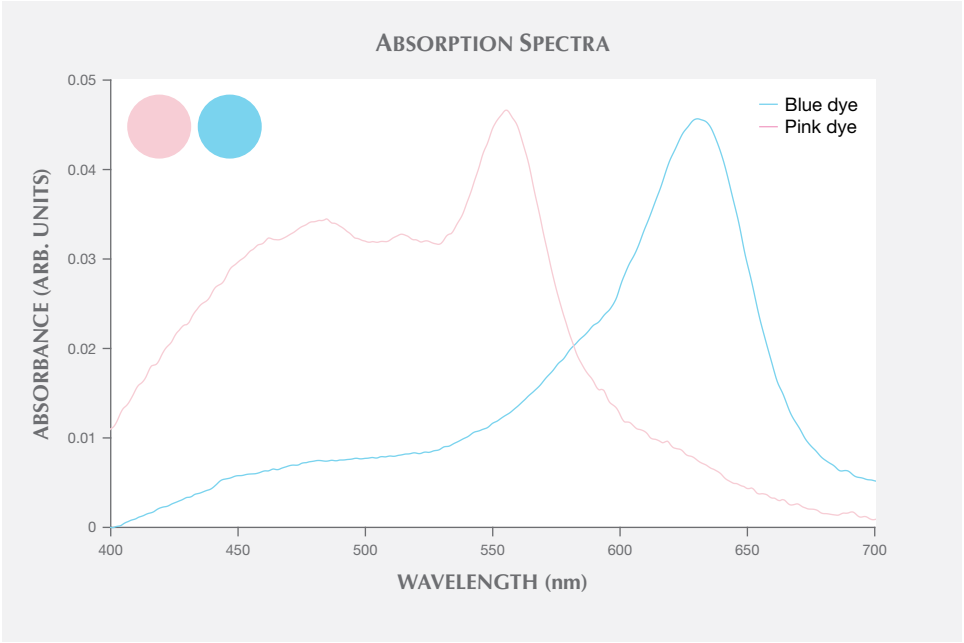

Figure 30. The absorption spectra of the dyes were collected by first soaking the opals in acetone to remove some of the dye material. Color swatches were then calculated from measurements of the dye molecules suspended in acetone to produce the color swatches for reference (inset).These swatches were consistent with the observed bodycolor of each opal.

importance of treatment disclosure in the trade. A few unscrupulous industry members could compromise the reputation of dealers selling natural opal as well as those properly disclosing treated material to their customers.

Edward Boehm
RareSource, Chattanooga, Tennessee
Nathan Renfro
GIA, Carlsbad

Figure 31. The blue and pink opals were confirmed to be dyed hydrophane opal, likely from Ethiopia. Half of each stone has been bleached using 3% hydrogen peroxide solution. Photo by Robison McMurtry.

CONFERENCE REPORTS

GSA 2017 annual meeting. The Geological Society of America (GSA) held its annual meeting October 22–25 in Seattle. For the fifth year, GIA hosted technical sessions on gemological research in the 21st century. More than 30 researchers, students, and gem experts from multiple institutions shared their most recent research results (figure 32).

Invited speaker **Evan Smith** (GIA, New York) presented the diamond inclusion suite study he carried out over the past two years. Following his paper published in *Science* on type IIa Cullinan-like, large, inclusion-poor, pure, irregular, resorbed (CLIPPIR) diamonds, Dr. Smith investigated *in situ* mineral phases in more than 20 extremely rare type IIb diamonds selected from GIA's day-to-day grading operations. The identified inclusions indicated that type IIb diamonds can originate from the lower mantle, at depths beyond 660 km. This surprising result refuted the well-accepted view that almost all superdeep diamonds are small and not of gem quality. **Nancy McMillan** (New Mexico State University) talked about the diamond provenance study she performed with **Catherine McManus** (Materialytics, Killeen, Texas). To ease consumer concerns about conflict diamonds, they conducted multivariate analysis of laser-induced breakdown spectroscopy (LIBS) on diamonds from various origins as well as synthetic diamonds. The information provided by LIBS on trace element composition and the electronic structure of atoms in diamonds aided in provenance determination. Through infrared (IR) mapping, **Sally Eaton-Magaña** (GIA, Carlsbad) and her colleague **Troy Ardon** documented the spatial changes of the optical defect center B^0 (uncompensated boron) in two type IIb diamond samples: One specimen was irradiated along an edge and

Figure 32. Presenters, session advocates, and senior executives from GIA at GSA's annual meeting in Seattle. Photo by Tao Hsu.

then annealed, while the other was only annealed. The irradiated diamond showed an obvious gradient in B^0 across the specimen itself and larger gradient changes during annealing compared to the other sample. These were caused by changes in compensating defects, which were then plotted by photoluminescence (PL) mapping.

The following three presenters from the University of Alberta shared their intriguing diamond formation research. **Mandy Krebs** offered trace element data of fluids trapped in gem-quality diamonds and compared them to those in fibrous diamonds that have been extensively studied. The results showed clear similarities in trace element patterns in both categories, which indicates that fibrous diamonds and gem diamonds may share a common origin. **Rebecca Stone** reported on diamond growth in saline fluid. She and her colleagues carefully documented diamond growth features under different salinities using a mixed KCl-NaCl brine system within the diamond stability field. Their series of experiments showed that Na-rich brine is a better medium for diamond growth than K-rich or Na+K mixed brines. **Robert Luth** discussed the partial melting mechanism facilitating diamond formation. He noted that the amount of diamond formed during this process depends on the lithology being melted and the composition of the fluid. The origin of the C-bearing fluid was also explored.

Following the diamond research presentations, invited speaker **Darrell Henry** (Louisiana State University) started the colored stone session with a talk on gem tourmaline. He pointed out that tourmaline is a very sensitive mineral that can incorporate and retain chemical and textural fingerprints from its environment. Paraíba, Paraíba-like, liddicoatite, and "chrome" tourmaline were used to illustrate this mineral's incredible scientific value. **Aaron Palke** (GIA, Carlsbad) discussed his recent findings on demantoid garnet's coloration mechanism. The existing theory attributes the brown coloration of this gem to intervalence charge transfer between Fe^{2+} and Ti^{4+} or Fe^{3+}. Dr. Palke challenged this interpretation based on recent spectroscopic results showing insufficient Fe^{2+} in demantoid to justify this mechanism. **Philippe Belley** (University of British Columbia) addressed the challenges of modeling spinel deposits. His potential solutions are based on detailed petrographic and geochemical studies on 14 samples from exceptionally well-exposed *in situ* spinel occurrences on Baffin Island in Nunavut, Canada. **Donald Lake** (University of British Columbia) compared two beryl occurrences in northern Canada with Colombian emerald deposits. He pointed out that in terms of formation environment, these potential emerald deposits are the first "Colombian-type" sources outside Colombia. **Rachelle Turnier** (University of Wisconsin–Madison) presented her study on oxygen isotope fractionation factors in corundum. Oxygen isotope ratios are important to understanding corundum genesis and origin determination. This study empirically calibrated the calcite-corundum oxygen isotope fractionation factor from the metamorphosed karst-bauxite deposits at Naxos, Greece. GIA's **Jennifer Stone-Sundberg** closed this portion of the session with a presentation on matrix-matched corundum standards development. She explained the importance of these newly developed standards in accurately determining trace element concentration and elaborated on the advantages of these standards over other commonly used products.

This year's poster session attracted 18 presenters, triple the number from last year (figure 33). **Daniel Howell** (Uni-

versity of Padua) presented new applications of DiaMap software in automated and semi-automated mapping of single substitutional defects (N and B) and micro-inclusion-bearing diamonds. **Paul Johnson** (GIA, New York) reported the first observation of nickel as the cause of the green color of an HPHT synthetic diamond. Nickel is commonly used in the metal flux that produces HPHT synthetic diamond, but it rarely contributes to diamond coloration. **Tyler Sundell** (Missouri State University) evaluated the viability of *in situ* $\delta^{13}C$ measurement in diamonds using time-of-flight secondary ion mass spectrometry (ToF-SIMS). **Tingting Gu** (GIA, New York) shared her study on micro- and nano-inclusions containing both N and Fe in type IaB diamonds. **Kyaw Soe Moe** (GIA, New York) presented the identification features of irradiated and annealed pink diamonds using IR spectroscopy and DiamondView imaging. **Elizabeth Levy** (Louisiana State University) explained how to directly measure Fe^{2+} and Fe^{3+} concentration in tourmaline crystals using synchrotron-based X-ray absorption near-edge spectroscopy (XANES). **Cole Mount** (New Mexico State University) found that using multivariate analysis of LIBS spectra of tourmaline can remove the negative influence of chemical zoning on host lithology determination. **Ulrika D'Haenens-Johansson** (GIA, New York) gave her insights on the 812 ct Constellation and two other large rough diamonds. FTIR and morphology observations indicate that the three could possibly be pieces from the same rough. **Christopher M. Breeding** (GIA, Carlsbad) described the first ever co-occurrence of magnesite, olivine, graphite, and silicon-vacancy defects in natural diamonds and explored the unusual conditions under which these diamonds formed. **Karen Smit** (GIA, New York) discussed the formation of peridotitic diamonds through isochemical cooling and eclogitic diamonds through redox buffering. **George Harlow** (American Museum of Natural History, New York) and **Rachelle Turnier** discovered that syenite-hosted sapphires from six different sources show a wide range of $\delta^{18}O$ values, which indicates scavenging of sapphire from multiple reservoirs. **Troy Ardon** (GIA, Carlsbad) used IR mapping, cathodoluminescence (CL) imaging, and hyperspectral mapping to correlate various optical and infrared point defects in diamonds with strong brown coloration. **Susanne Schmidt** (University of Geneva) outlined U-Pb geochronology work done on zircon inclusions in Sri Lankan sapphires. This study was performed by her former graduate student **Emilie Elmaleh. Ziyin Sun** (GIA, Carlsbad) investigated the role of chromophore vanadium in coloration of pyrope-spessartine garnet, using samples without a color-change phenomenon. **Eric Brinza** (University of Wisconsin–Eau Claire) described an IR spectroscopic study on hydrothermal quartz crystal. Different hydroxyl species concentrations vary both vertically and horizontally through the crystal. **Kyle Tollefson**, also of the University of Wisconsin–Eau Claire, presented IR and visible spectroscopic study on coloration of watermelon tourmaline. The results showed that the chromophore was incorporated during crystal growth and could reflect changes in the growth environment. **Dona Dirlam** and her coauthors from GIA's Richard T. Liddicoat Gemological Library and Information Center (Carlsbad, California) chronicled the legendary John Sinkankas, whose collection of books and other publications was acquired by GIA in 1988 to form the basis of its world-renowned gemological library.

Tao Hsu, James E. Shigley, and Dona Dirlam
GIA, Carlsbad

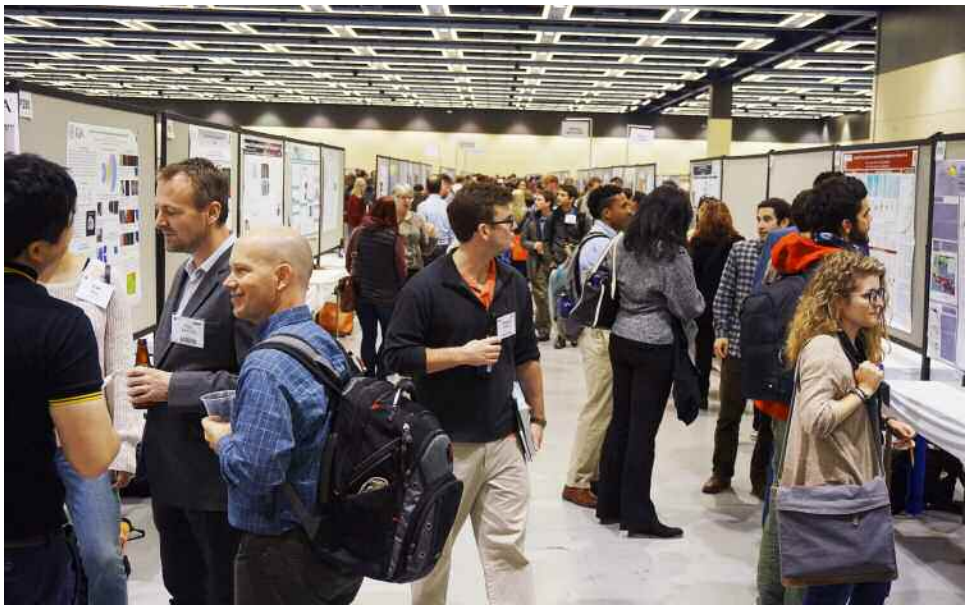

Figure 33. The GSA annual meeting's gemological research poster session featured 18 presenters from all over the world. Photo by Cathy Jonathan.

Figure 34. A gathering of the presenters at the fifth World of Gems Conference, held in Chicago in September 2017. Photo by Scott Drucker.

World of Gems Conference. The Gemworld International team, headed by **Richard Drucker**, hosted the fifth World of Gems Conference September 23–24 at the Loews Hotel in Chicago. The event was bookended by optional classes, making it an ideal opportunity for attendees to learn about new topics from a diverse group of international speakers (figure 34) and brush up on their practical gemology skills. Between presentations, the conference held its first-ever poster session. The posters included interactive discussions on jet and the identification of light blue stones using the polariscope and the conoscope, hosted by **Sarah Caldwell Steele** (Ebor Jetworks, Whitby, United Kingdom) and **Kerry Gregory** (Gemmology Rocks, Weavering, United Kingdom), respectively.

Invited speaker **Emmanuel Fritsch** (University of Nantes, France) opened with a talk about the identification of melee synthetic diamonds. He noted that while the majority of specimens are not hard to identify, near-colorless HPHT-treated synthetic melee may still be challenging. Dr. Fritsch also provided a brief history of synthetic diamond production and the current state of the industry, as well as basic and advanced methods of separating synthetic from natural. Isotropy and anomalous double refraction—otherwise known as strain—were covered in some detail, as he considered these very useful identification aids. **Jon Phillips** (Corona Jewellery Co., Toronto) reviewed world diamond production and the output of mines such as Jwaneng in Botswana, which accounts for 15% of total global production. Meanwhile, Canada's five operating mines rank among the top 19 producers. One key takeaway from his talk was that De Beers plans to invest US$140 million on a marketing campaign aimed at women buying diamond jewelry for themselves. This should not be ignored by jewelers. Mr. Phillips also reflected on the threat of synthetic melee in the market. **This author** (GIA, Bangkok) reviewed the different types of pearls (nacreous and non-nacreous) seen in the market and the various mollusks that produce them. The presentation detailed the surface structures of a wide selection of non-nacreous pearls and concluded with a summary of the more frequently encountered treatments. **Roland Schluessel** (Pillar & Stone International, San Francisco) provided a comprehensive look at Burmese jadeite and defined the various types, including the term *fei cui* (kingfisher) for the vivid green variety. He examined cultural aspects and discussed factors such as grain size and orientation, which relate to transparency and overall quality. Mr. Schluessel also provided insight into the different colors and patterns, as well as the differences between omphacite and jadeite. **Çiğdem Lüle** and **Stuart Robertson** (Gemworld International, Glenview, Illinois) reported on various gem treatments that provide enough supply to satisfy market demand. Frequently encountered treatments and the pricing of untreated vs. treated material were reviewed. Diamond was offered as an example of a gem where treatments markedly affect the end value, while tanzanite shows little if any price difference between natural and treated material. A very lively presentation from **Kerry Gregory** about the daily happenings in the pawnbroking world rounded out day one. Ms. Gregory discussed some of her experiences saving valuable pieces that would have otherwise been destroyed due to lack of resources, training, and time. She also provided insight into her use of simple yet valuable gemological methods (such as the polariscope and conoscope) in identifying light blue stones removed from items destined for the melt.

J.C. (Hanco) Zwaan (Netherlands Gemmological Laboratory, Leiden) started the second day with a comprehensive look at the geological formation and gemological

characteristics of metamorphic sapphires from Sri Lanka and to a lesser extent Montana. The search for a primary sapphire deposit in Sri Lanka and the discovery at Wellawaya (which Dr. Zwaan was involved with) were illustrated. Subsequent discussions on the use of chemical plotting in the separation of Sri Lankan and Montana material, from one another and from other sources, showed that it is beneficial but care is still needed with some cases that may overlap. **Çiğdem Lüle** followed with a solo talk about the various natural and "non-natural" black gem materials and the limitations encountered when testing such materials. She covered black diamonds in some detail, outlining the differences between the rare naturally colored stones and heated or irradiated specimens. **Al Gilbertson** (GIA, Carlsbad) reported on the status of GIA's fancy-cut diamond grading project and showed the challenges faced when producing a system that takes all variables into consideration and satisfies all opinions. This was reinforced after receiving feedback from 440 participants in six global locations who were asked to look at various fancy cuts and answer a series of questions. **Alan Bronstein** (Aurora Gems, New York) took attendees on a journey through the colorful world of fancy-color diamonds, looking at the subtleties of the main colors available: yellow, orange, pink, red, green, and blue. Mr. Bronstein was clearly in favor of retaining the original cut of a diamond and not re-cutting it. Chameleon diamonds were also briefly covered. "Beauty trumps rarity" was Mr. Bronstein's motto. **Richard Drucker** brought the presentations to a close with a look at some challenges that affect the pricing of gemstones. From the small print in pricing guides that might not be fully understood by users to gemological reports that raise doubts or cause confusion in appraisers' minds, it became very apparent that the valuation of some colored stones needed careful thought.

The conference ended with a Q&A session in which Mr. Drucker opened the floor to all attendees. Topics such as correct nomenclature and disclosure, brand name cooperation with items submitted for valuation, and color diamond grading consistency were covered.

Nicholas Sturman
GIA, Bangkok

IN MEMORIAM

Peter J. Dunn (1942–2017). Distinguished mineralogist and author Pete Dunn died November 8 at the age of 74. He is best known for the 134 new mineral descriptions he wrote over the course of his long career.

Dr. Dunn received his master's degree and PhD in mineralogy/geology from the University of Delaware in Newark. Before joining the Smithsonian Institution's National Museum of Natural History in 1972, he served in the U.S. Air Force and worked at Boston University as a curator in the geology department. In addition to characterizing new minerals, Dr. Dunn published a nine-volume monograph and more than 70 papers on the Franklin–Sterling Hill mining district in New Jersey in a number of scientific publications. In 1987, a member of the clinopyroxene subgroup from the Franklin mining district was named "petedunnite" in his honor. A prolific contributor to *G&G* throughout the 1970s, Dr. Dunn served on the journal's editorial review board from its inception in 1981 until 1987. Upon his retirement from the National Museum of Natural History in 2008, he volunteered at the museum's information desk until his death.

ERRATA

1. In the Fall 2017 Lab Note on screening of mounted melee using the GIA iD100 (pp. 366–367), a citation directed readers to p. 239 of the Fall 2017 Lab Notes section. The correct issue is Summer 2017, p. 239.
2. Also in the Fall 2017 Lab Notes section, the inset photo in figure 4 was taken by Kyaw Soe Moe.

MULTIMEDIA HIGHLIGHTS FROM 2017

Visit *G&G* online (www.gia.edu/gems-gemology) to explore free multimedia content. Scan the QR codes below with your smartphone or tablet, or use the links below.

2017 Dr. Edward J. Gübelin Most Valuable Article Award: Cast your vote for the three most important articles from 2017, and enter a drawing to win a one-year print subscription to *Gems & Gemology*. www.gia.edu/most-valuable-article-2017

The Dreher Family's Extraordinary Carvings: Interviews and photo galleries capture the lifelike detail and painstaking process followed by Gerd and Patrick Dreher, the two most recent standard-bearers of a German carving dynasty. www.gia.edu/gems-gemology/winter-2017-gem-virtuosos

Colombia's Emerald Industry: Videos reveal Colombia's emerald mining areas and the cutting and trading industry in Bogotá. www.gia.edu/gems-gemology/fall-2017-colombian-emerald-industry

The Lomonosov Diamond Deposit: The geology, production, and evaluation process at Russia's Lomonosov deposit are examined in videos taken at the source. www.gia.edu/gems-gemology/summer-2017-lomonosov-deposit

Brazilian Diamonds: Slideshows and videos document this historical diamond source, where large-scale production is expected to resume. www.gia.edu/gems-gemology/spring-2017-brazilian-diamonds

2017 Tucson Gem Shows: Watch exclusive videos from our annual coverage of the gem shows, featuring interviews and insider insight. www.gia.edu/gems-gemology/spring-2017-gemnews-tucson-overview

Micro-Features of Ruby

Treated

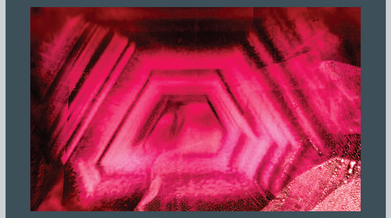

A hexagonal cloud results from heat treating this Burmese ruby from Mong Hsu. Field of view 2.97 mm.

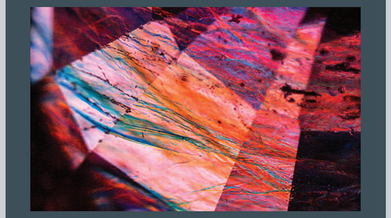

A blue and orange “flash effect” is prominent in this lead-glass-filled ruby. Field of view 2.90 mm.

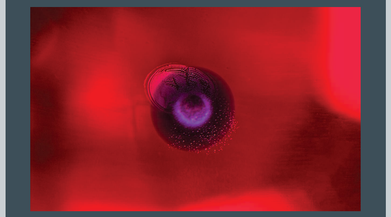

Internal diffusion of titanium around a rutile crystal in a beryllium-diffused ruby. Field of view 1.03 mm.

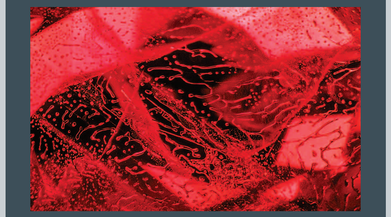

Heat treating ruby in the presence of flux can help to heal cracks. It can also leave flux residue trapped inside, as seen in this Burmese ruby. Field of view 3.10 mm.

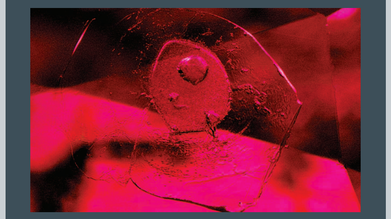

Heating of a Thai ruby caused this inclusion to rupture, providing evidence of treatment. Field of view 2.15 mm.

Natural

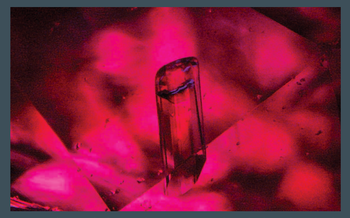

A rare inclusion of iolite (cordierite) is seen in this ruby from Greenland. Field of view 1.42 mm.

Rounded protogenetic crystals of orange spinel are extremely rare in Burmese ruby. Field of view 3.45 mm.

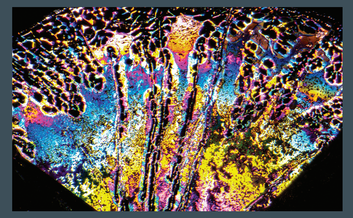

Rainbow-colored thin-film interference colors are seen along a partially healed fracture in this ruby from Thailand. Field of view 1.10 mm.

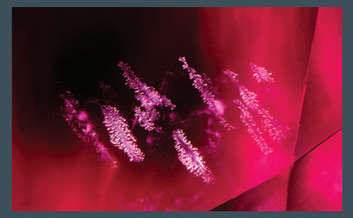

Delicately patterned, crystallographically oriented thin-film inclusions are found in a ruby from Vietnam. Field of view 2.02 mm.

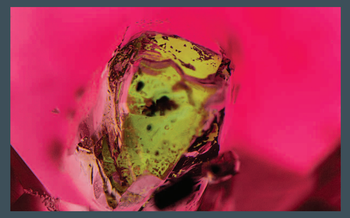

A very rare crystal inclusion of vibrant yellowish green vesuvianite is seen in this Burmese ruby. Field of view 1.99 mm.

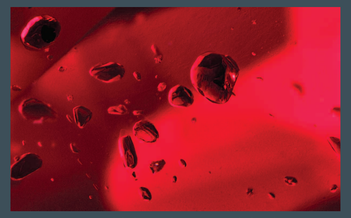

Dark, transparent amphibole crystals are commonly found in Mozambique rubies, such as the one shown here. Field of view 2.62 mm.

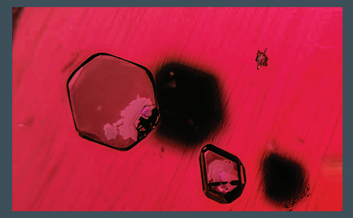

Metal sulfide crystals are sometimes observed in rubies from Mozambique. Field of view 1.42 mm.

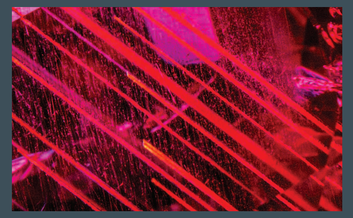

The intersection of twinning planes can provide a conduit for epigenetic solutions containing iron compounds to enter the interior of some rubies, as seen in this example from Mozambique. Field of view 4.35 mm.

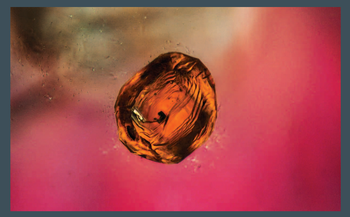

A rare orangy brown crystal of sphalerite floats in its host, a ruby from Myanmar. Field of view 1.03 mm.

Iridescent exsolution rutile is oriented in three directions in this Burmese ruby. This “silk” is responsible for creating asterism in gem-quality ruby. Field of view 1.99 mm.

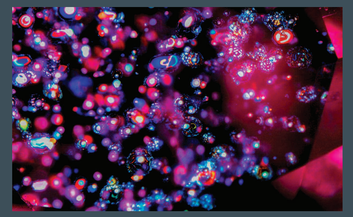

A field of reflective thin films is indicative of this ruby’s Thai origin. Field of view 4.10 mm.

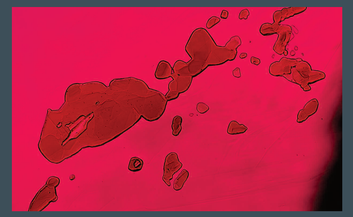

Thin platy inclusions of chromite can be found in ruby from Mozambique. Field of view 1.44 mm.

This black, blocky crystal with tension cracks, found in a Burmese ruby, was identified as uraninite. Field of view 1.03 mm.

Protogenetic carbonate inclusions are commonly seen in rubies that form in marble, as this example from Afghanistan shows. Field of view 1.26 mm.

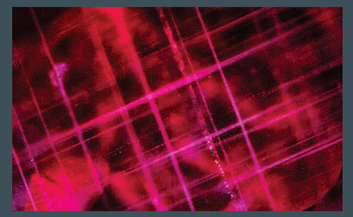

The aluminum hydroxide mineral boehmite, seen in this ruby from Greenland, is often found in corundum. Field of view 1.42 mm.

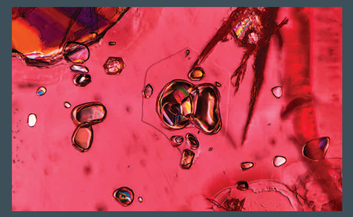

Inclusions of amphibole crystals and mica in a ruby from Mozambique show birefringent colors when examined in polarized light. Field of view 1.76 mm.

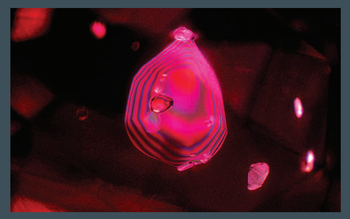

Cross-polarized light reveals an otherwise hidden ruby crystal in a Thai ruby host. Field of view 3.90 mm.

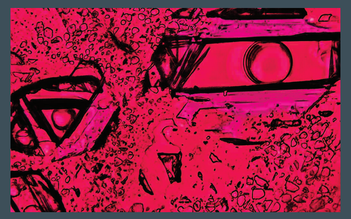

Carbon dioxide fluid trapped in angular negative crystals in this ruby from Tajikistan proves that the stone has not been heat treated. Field of view 0.288 mm.

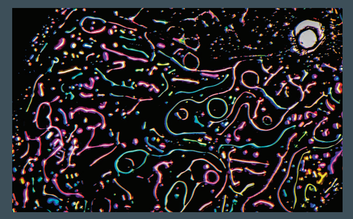

This partially healed, iridescent fingerprint in a Thai ruby shows an unusual and irregular curved pattern. Field of view 1.10 mm.

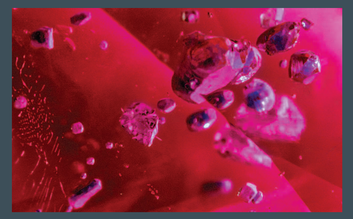

Very rare inclusions of blue lazurite are a welcome surprise in this Burmese ruby. Field of view 3.46 mm.

Synthetic

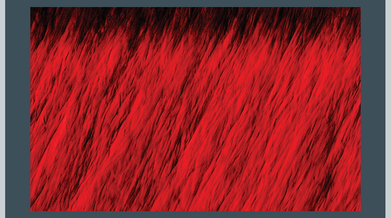

Chevron-shaped graining is diagnostic of the hydrothermal growth method used to produce this Tairus synthetic ruby. Field of view 1.22 mm.

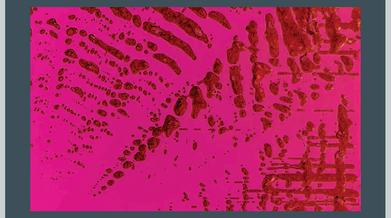

Crystallographically aligned yellowish flux residue reveals the synthetic origin of this Ramaura flux-grown ruby. Field of view 4.74 mm.

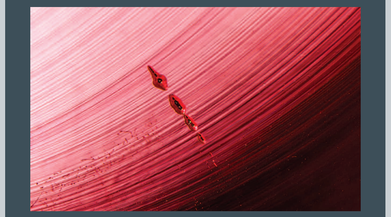

Curved striae are diagnostic of this flame-fusion synthetic ruby. The striae are accompanied by several gas bubbles that further reinforce the synthetic origin. Field of view 3.59 mm.

Platinum crystals are a common feature in Chatham flux-grown synthetic ruby. Field of view 1.70 mm.

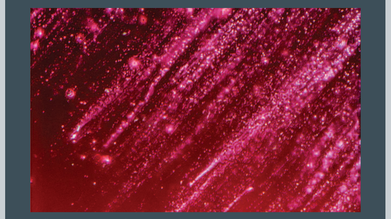

Reflective stringers of exsolution flux particles in Kashan flux-grown synthetic ruby are best seen using a fiber-optic illuminator. These oriented particles are diagnostic of Kashan synthetics. Field of view 1.78 mm.

This chart contains a selection of photomicrographs of natural, synthetic, and treated rubies. It is by no means comprehensive. The images show the visual appearance of numerous features a gemologist might observe when viewing rubies with a microscope.

Published in conjunction with Nathan D. Renfro, John I. Koivula, Jonathan Muyal, Shane F. McClure, Kevin Schumacher, and James E. Shigley (2017), “Inclusions in Natural, Synthetic, and Treated Ruby,” *Gems & Gemology*, Vol. 53, No. 4, pp. 457–458. Photomicrographs by Nathan D. Renfro, John I. Koivula, and Jonathan Muyal.

GIA®